STRAHLTECHNIK   BAND 60
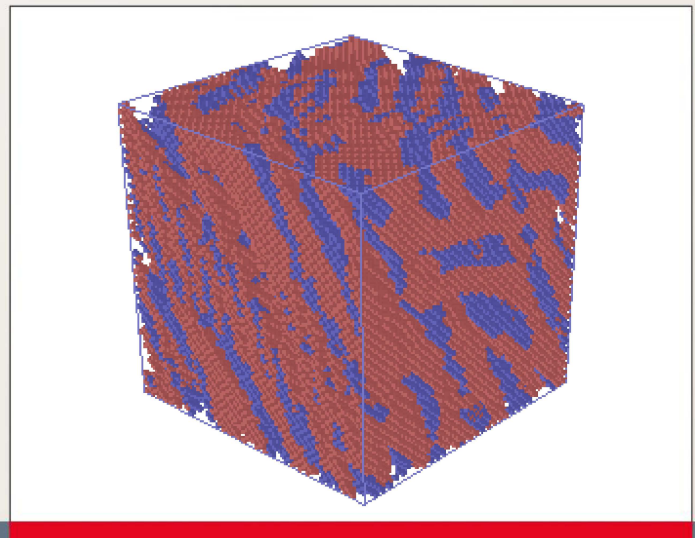
Edwin N. Kamau

Dynamic wave field
synthesis: enabling the
generation of field
distributions with a large
space-bandwidth product

Wissen schafft Wirtschaft

Dynamic wave field synthesis: enabling the generation of field distributions with a large space-bandwidth product

Eidesstattliche Erklärung

Hiermit erkläre ich wahrheitsgemäß, dass ich die vorliegende Arbeit ohne unerlaubte fremde Hilfe angefertigt habe. Ich habe keine anderen als die in den Quellen angegebenen Hilfsmittel benutzt und die den benutzten Werken wörtlich oder inhaltlich entnommenen Stellen als solche kenntlich gemacht.

Bremen, den 03. März 2016,

(Edwin N. Kamau)

Kamau, Edwin N.

Dynamic wave field synthesis: enabling the generation of field distributions with a large space-bandwidth product

Abstract

The generation and manipulation of electromagnetic field distributions plays an essential role in physics in general, and particularly in the vast field of physical optics. In the current state of the art, one of the most convenient methods of performing this task is provided by either static or dynamic diffractive as well as holographic optical elements. Currently available dynamic optical elements, such as spatial light modulators, do offer on the one hand high temporal flexibility. They however have a limited space-bandwidth product (SBWP), and thus limited degrees of freedom. This arises primarily from a limitation in the number of controllable elements, their inherent two dimensional nature and limited lateral extent. Conventional static optical elements, such as planar or volume holographic elements, have on the other hand high degrees of freedom but low flexibility in terms of temporal applications. An optical system that facilitates dynamic synthesis of field distributions with high SBWP is thus highly desirable.

This thesis presents a novel approach that facilitates the generation of a set of arbitrary orthogonal elementary waves, which can in turn be coherently superposed in order to generate optical fields with a high SBWP. To achieve this goal a hybrid system that consists of an angular multiplexed computer generated volume hologram (CGVH) as a static element and a spatial light modulator as a dynamic element is investigated, developed and characterized. CGVHs are volumetric holographic optical elements whose complex transmission function can be modeled mathematically in terms of the scattering potential of a given dielectric medium. This work presents an approach that employs perturbation theory in deriving a more elaborate mathematical model that is based on a series approximation of the complex wave field scattered from a volume hologram. The mathematical model behind this approach essentially incorporates various physical constraints that account for the discretized numerical design and a laser lithography based fabrication of the holograms in a non-linear optical material. Initial simulations and experimental work done to characterize this system show that the proposed approach facilitates a dynamic decoupling of single or a linear combination of far field projections without any detectable cross-talk between them. This work furthermore demonstrates that Bragg selectivity on the order of $\Delta\theta \leq 1°$ can be achieved. This in turn allows for the superposition of a set of wave fields, which can be decoupled sequentially or simultaneously from a CGVH with an SBWP $= 5.4 \times 10^8$ for each far field projection. Furthermore, this system facilitates dynamic synthesis of fields having an SBWP $\geq 1.1 \times 10^{10}$, i.e. approximately 4 orders of magnitude higher than the current state of the art, which is based on cascaded computer generated holograms.

Acknowledgment

I would like to first and foremost extend a large vote of thanks to my adviser Prof. R. B. Bergmann for his support, guidance and interesting discussions. I am also very grateful to all my colleagues at the coherent optics group for numerous suggestions, recommendations and assistance throughout my time at BIAS. Many thanks also to Dr. C. Falldorf and Dr. C. von Kopylow for their guidance and support.

I wish to express my gratitude to the rest of my fellow scientists and the technical team at BIAS for their constant support and help. In particular I wish to acknowledge three members of my department, Thomas Meeser, Julian Heine, Mostafa Agour and Vijay Parsi Sreenivas, for their support, meticulous proof reading of this work as well as for their feedback and assistance.

I dedicate this work to the most significant people in my life and to those who have been very instrumental to helping me come this far, my family. I am also greatly indebted to Marlis and Martin for always being there for me. And last but not least I thank my parents for their encouragement, prayers, never ending love and support.

Edwin N. Kamau

Contents

,

Symbols

A Amplitude of light

$\mathcal{A}$ Zero-order term of a hologram

$\boldsymbol{\mathcal{B}}$ Magnetic flux density vector

$\mathcal{B}$ Magnitude of the virtual image of a hologram

C A region where a set of constraints intersect / discreet quantization levels

c_k Weighting factor for the iterative algorithm

$\boldsymbol{\mathcal{D}}$ Electric displacement field vector / electric flux density

$\mathcal{D}_B$ Bounded Domain

$\boldsymbol{E}$ Complex electric field vector

$\mathcal{F}\{\cdot\}$ Fourier transform

$\boldsymbol{\mathcal{E}}$ Electric field vector

$\mathcal{F}\{\cdot\}^{-1}$ Inverse Fourier transform

$\boldsymbol{H}$ Complex magnetic field vector

$\boldsymbol{\mathcal{H}}$ Magnetic field vector

I Intensity of light

$\acute{I}$ Irradiance of light

i   Imaginary unit

$\boldsymbol{k}$ Wave vector in a given medium

k Wave number in a given medium

L_i Size of a hologram in the i-direction

$H(\cdot)$ Impulse response

$\mathcal{M}$ Magnetic polarization vector

n Refractive index of a given medium

$\mathcal{P}$ Polarization density vector

$\mathcal{P}_f$ Forward mapping operator

Q Quality factor of a volume hologram

$\boldsymbol{q}$ Position vector in frequency domain

$\boldsymbol{r}$ Position vector in spatial domain

S Scattering potential

$\boldsymbol{\mathcal{S}}$ Poynting vector / power density vector

$\{\boldsymbol{s}\}$ Observation plane

t Time

U Complex amplitude of a wave field

U_B Scattered field - first Born approximation

u Scalar function

V Volume

W Signal window

$\{\boldsymbol{x}\}$ Source plane

$\Delta\varphi$ Phase difference

δ_n Refractive index change / modulation

ϵ Permittivity of a given medium

ϵ_r Relative permittivity

γ Perturbation parameter

Φ Complex phase

Φ_R Scattered complex phase - first Rytov approximation

ϕ Phase of a wave field

η Diffraction efficiency

$\boldsymbol{\kappa}$ Absorption coefficient

x

$\tilde{\kappa}$	Coupling constant
Λ	Grating period
λ	Wavelength of a wave field
μ	Permeability of a given medium
ν	Temporal frequency
$\boldsymbol{\theta}$	Unit vector specifying the propagation direction of a plane wave
θ_B	Bragg angle
Σ	Extent of a source or an illuminated aperture
τ	Complex transmittance
$\Delta\Omega$	Solid angle
ω	Angular frequency
χ	Electric susceptibility
∇	Nabla operator / symbol

1. Introduction

1.1. Overview

Within the scope of physical optics, an optical element can be thought of as a device that transforms a single or a set of input optical signals into a set of output signals. Such an optical element could for instance be a simple linear optical element such as a mirror, a beam splitter or a prism. It could on the other hand be a micro or nano optical element that is integrated in a complex quantum optical system [1]. In all optical systems, ranging from geometrical optics based instruments to highly specialized quantum physics based systems, optical elements with distinct and optimized transfer functions are desired. Holograms can be designed to have such transfer functions thus making them highly desirable in a vast number of applications. In this case these holograms are referred to as holographic optical elements (HOE) [1, 2].

The concept of holography has been around for more than six decades now. Since their invention by Dennis Gabor in 1948 and of coherent laser light in 1960, holograms have motivated innumerable inventions. Specifically in the field of modern optics these applications include microscopy [3, 4], data storage [5, 6], metrology [7–10], and advanced imaging [11–13]. Another application has been the synthesis and analysis of optical wave fields [14–17]. Most of these applications utilize optical holography as a method for recording and reconstructing both the phase and amplitude of a complex wave field [18].

Thereby, the basic principle of holography which consists in the transformation of phase changes into recordable intensity changes is employed. Conventionally a hologram is produced by the interference between a given field, e.g. one that is diffusely scattered by an object, and a reference wave field. A predominant advancement to this scheme was the introduction of a smart combination of the holographic principle with the carrier frequency technique known from radar technologies [19]. With this approach, the twin image problem in Gabor's original in-line scheme could be effectively eliminated. However, owing to the high spatial frequency of the intensity fluctuations involved, a medium with adequate spatial resolution such as a photosensitive film was required to encode the hologram. Initially a photosensitive film was used in most applications. However, an approach that would allow for recording and digitally manipulating holograms was strongly desired. The first idea for such an approach was initially conceived and published as early as 1967 [20]. The introduction of digital cameras with reasonable space-bandwidth products (SBWP) [21] and powerful processor technology, which in turn led to a major improvement of digital holography (DH) can thus be viewed as a crucial step [12, 22, 23].

Another very commendable invention was made by Lohmann in 1967 [24]. He proposed a method of numerically generating holographic optical elements in the form of interference patterns using a digital computer. These elements are referred to as *computer generated holograms* (CGH) and are usually placed in the wider category of diffractive optical elements (DOE). CGHs are computed using the same basic principle of holography described above. A CGH can thus be described as a holographic optical element which is designed to modulate a given input complex wave field and thereby produce a desired optical field, either in its near field or far-field domain.

Depending on their temporal characteristics CGHs can generally be classified as either static or dynamic. Static CGHs are fabricated by transferring the designed element onto an appropriate substrate mainly by means of micro or sub-micrometer fabrication methods. Hereby, a variety of methods such as computer driven plotter writing [25], projection lithography [26, 27], direct laser writing [28] or electron-beam lithography [29] can be used. In the near past, the application of novel optical micro and nano fabrication methods has facilitated the realization of static CGHs with a comparatively high SBWP, thus making them ideal for applications where whole field and high frequency modulation of wave fields is desirable. They are therefore applied for instance for the generation of tailored illumination for aspheric testing [30] as well as the generation of complex light field distributions - e.g. optical vortex beams which are used in optical tweezers [31], or holographic projection [32, 33]. Similarly, they are used in lithographic systems whereby a master CGH is used to expose a desired intensity pattern on a substrate coated with a photoresist [23]. One major drawback of this type of CGHs is their static nature which leads to less flexibility in terms of temporal applications. This implies that for each given functionality, a long design and fabrication process is needed.

Dynamic CGHs which can on the other hand be attained by transferring the designed element onto a programmable element, e.g. a spatial light modulators (SLM) or a digital mirror devices (DMD). A digital mirror device is a semiconductor based micro-electrical-mechanical system consisting essentially of an array of individually addressable micro-mirrors. It is an electrical input, optical output element that can be used for high speed, efficient, and reliable spatial light modulation, whereby the position of each mirror is individually controlled using an external electrical signal [34, 35]. An SLM consists, in analogy to a DMD, of an array of individually controllable pixel elements. But unlike a DMD it is made up of liquid crystal elements whose index of refraction can be controlled electronically or optically [36, 37]. Dynamic CGHs are mainly applied for wavefront generation and adaptive illumination for example in imaging and projection display systems [38, 39], microscopy [40], wave field sensing [41–43] and in optical metrology [44–46]. However, these type of CGHs can not be applied in some of the aforementioned applications (e.g. aspheric testing) due to their inherent limitation in SBWP. This limitation arises from a number of technological constraints that include their size and most importantly their limited number of controllable elements, which is on the order of 1000x1000 micro mirrors or liquid crystal pixels. A system that combines the advantages of both types of CGHs, i.e. one that facilitates dynamic synthesis of wave fields with a large SBWP is thus highly desirable

[47, 48].

In order to allow the generation of a desired wave field with a high *signal* SBWP the degrees of freedom of the optical system used to generate it, and hence the SBWP of the CGH, must be higher or at least equal to that of the desired wave field [21]. Therefore, the task of designing and fabricating CGHs that allow for a generation of arbitrary wave fields with a high SBWP across a given plane has been extensively studied. Thereby advances in micro and nano fabrication methods, have facilitated for instance the generation of discontinuous diffractive optics using a diamond turning process. This novel approach has allowed for the realization of multiplexed CGHs with a much higher SBWP as compared to conventional CGHs [32, 33]. Nonetheless, owing to their inherent 2D nature, these CGHs can only modulate an impinging wave across a single transverse plane. This limitation has led to an ever increasing demand of developing 3D holographic optical elements. For instance, stratified CGHs in a cascaded setup have been proposed [49] and it has been shown that by adding more degrees of freedom they expand the system's solution space thus facilitating both angular and frequency multiplexing [50, 51]. Another example is presented by thick volume holograms [52]. These are optically recorded periodic diffractive optical elements that depict both angular and wavelength selectivity in cases where the Bragg condition is fulfilled, as opposed to their 2D counter parts. Although these two types of volume elements have found numerous applications their ability to generate arbitrary light distributions within a certain 3D domain is quite limited. This is mainly due to their comparatively low diffraction efficiency, since the efficiency of the device decreases as the square root of the number of holograms that are recorded in a single hologram. This can also be attributed to the fact that for thick holograms, since individual voxels cannot be addressed, the achievable degrees of freedom are limited by the optical recording process [53].

The first *computer generated volume hologram* was proposed as a specific type of modulated three dimensional grating a few decades ago [54] and has been investigated continuously since then [55, 56]. Recently, we have in our previous work studied and demonstrated their superior performance in terms of angular and wavelength multiplexing [47, 57]; as well as their application in the dynamic synthesis of wave fields [17]. State of the art CGVHs can be described as volumetric holographic optical elements whose complex transfer functions can be controlled and optimized in the design process. In analogy to their 2D counterparts, CGVHs are generated numerically by means of iterative optimization algorithms. They are modeled mathematically as a randomly scattering inhomogeneous medium that is characterized by a refractive index distribution - the so called scattering potential [58]. The scattering potential is assumed to be embedded in a known background potential. It therefore corresponds to a modulation of the refractive index, e.g. in the bulk of a transparent dielectric material thus facilitating fabrication of CGVHs by means of 3D laser lithography.

The problem of designing a CGVH can be stated as follows: *the set of wave field distributions that is to be generated in a certain predefined domain is the known effect for which the scattering potential inside the CGVH is the sought cause.* This is in essence an ill-posed inverse problem involving the mapping of the 3D field dis-

tribution scattered in the volume of the CGVH onto one or a set of transverse 2D planes. The resolution of this inverse problem requires very good knowledge of the underlying forward problem, i.e. an explicit description of how light is scattered inside the volume of the hologram is needed [17, 58]. In the current design approach several shortcomings in the applied forward model and its implementation have however been recognized. These shortcomings have the effect of imposing very stringent restrictions on the achievable optical functionality of CGVHs and can be listed as follows [17]:

(i) In the current state of the art the assumption of weak scattering is necessary in order to derive a linear model for the numerical modeling of the scattering process. Hereby the Born approximation is applied. This approximation is derived by considering only linear perturbation of the amplitude of the scattered wave field. This assumption leads to a constraint that limits the refractive index modulation allowed to very small values within a range on the order of $\delta_n \approx 10^{-4} \cdots 10^{-3}$, relative to the index of the background material [56, 57]. This in turn limits the optical functionality of the CGVH in terms of angular and frequency selectivity, as well as the achievable SBWP. An approximation that gives a more accurate estimate for larger CGVH sizes without such stringent restrictions has not yet been considered in this context and will be considered in the course of this work.

(ii) The iterative Fourier transform algorithm that has been applied so far tends to stagnate after the first few iterations [56]. This is attributed to the fact that a set of basic constraints in both the frequency and space domains are not fully fulfilled thereby leading to convergence to a local minimum. For instance, in the definition of the coding and quantization operators, which are crucial for the discrete representation and for the fabrication of the CGVH in a dielectric material, various linear interpolation schemes have to be employed. This misrepresentation of values can be shown to lead to deviations from the desired optimal distribution. This in turn implies that diffraction still occurs even for cases where the Bragg condition is not fulfilled. For multiplexed CGVHs, where the fulfillment of the Bragg condition is indispensable, this will result in a poor signal to noise ratio (SNR) and to a reduced diffraction efficiency.

(iii) In the current state of the art, only fabrication of CGVHs in glass by means of direct laser writing has been investigated. In such an approach, the intensity of the laser has to be chosen appropriately in order to achieve a condition where photomodification only occurs in the focal plane. Therefore, one challenging task is to be able to perform this complicated micro-structuring with a spatial resolution better or on the order of $1\,\mu$m and thereby induce refractive index changes on the order of $\delta_n \approx 10^{-4} \cdots 10^{-2}$. Here, we propose a new approach for the fabrication of CGVHs in an optical nonlinear material. In such a nonlinear optical material the absorption profile is narrower than the beam profile. This allows us to design and realize CGVHs with much smaller voxels as compared to the current state of the art.

1.2. Aim and Scope of this Thesis

In order to describe, generate and/or analyze optical fields in a specified three dimensional domain, it is customary to decompose them into independent discrete scatterers, such as planes, segments or points, which can be treated separately [59]. In this work we however focus on a problem in which an arbitrary wave field is defined in a given three dimensional domain. The main aim is to analyze light distributions scattered in the bulk of a volume hologram in order to develop a general method of computing the scattering potential of the aforementioned CGVHs. Moreover, we investigate how such holograms can be applied to generate a set of arbitrary orthogonal elementary waves, which can in turn be coherently superposed in order to generate optical fields with a high SBWP.

This work thus reviews the theory and the fundamental limitations of the inhomogeneous wave equation with respect to its application in solving scalar scattering problems. It investigates a novel approach that can be used to improve the capabilities of numerically computed volume holographic optical elements in terms of their Bragg selectivity, diffraction efficiency and achievable spatial bandwidth product. Specifically, this thesis extends the perturbation theory based approximations to the scattered field.

In a nutshell, the general aim of this thesis is the derivation and investigation of a model that allows for the design of CGVHs with an advanced optical functionality. Furthermore, the feasibility of fabricating such holograms in a nonlinear optical material by means of femtosecond laser lithography is assessed. To achieve these goals, a more accurate prediction of the field scattered within the volume of a CGVH is developed. Thereby, a novel formulation of the inverse random scattering problem for a weakly scattering inhomogeneous dielectric medium is presented. This thesis aims to achieve these goals by undertaking the following steps:

- Deriving an integral formulation of the wave equation for the aforementioned forward problem of computing multiplexed CGVHs. Hereby, a forward mapping operator that defines a 3D mapping of an arbitrary complex field by the scattering potential of the hologram onto a desired target field will be derived.

- Deriving the general sampling conditions that are necessary for the computation of such a *discrete* scattering potential. To do this, it is initially assumed that the magnitude of the scattered field for each projection must be continuous and bounded within a compact support. This will pave way to the development of an optimization theory based iterative technique that can be applied to numerically solve the aforementioned inverse problem within the accuracy of the Rytov approximation.

- Clearly formulating this inverse problem, which can be described as the problem of computing the scattering potential, given a set of desired optical fields and the corresponding physical constraints. This will essentially entail the transformation of these set of physical constraints into constraints on the scattering potential of the volume HOE.

- Assessing further physical constraints that need to be satisfied for the proposed hybrid system, which essentially utilizes the Bragg selectivity of CGVHs and the flexibility of a programmable spatial light modulator.

- Investigating an approach that is based on a multiphoton absorption process (MPA) to fabricate CGVHs in a nonlinear optical material such a photosensitive glass-ceramic. Since the proposed holograms are defined as discrete volume elements, an appropriate method that is able to create the desired subsurface micro structures in the bulk of the dielectric material needed.

- Assessing the feasibility of generating not only single but also a linear combination of 2D wave field distributions, which have a higher space-bandwidth product as compared to the currently available elements. To accomplish this goal, a spatial light modulator will be applied to simultaneously couple in a set of illumination fields into the CGVH and thereby decode a linear combination of the single far-field projections.

1.3. Structure of this Work

This work is divided into three major parts. The first part aims at reviewing the physical background behind the interaction of electromagnetic with different dielectric materials, which are encountered in the course of this work. For this purpose, Maxwell's equations are introduced and used to present a description of light as electromagnetic radiation. In the next step wave optics theory is then introduced as an approximation of the electromagnetic theory, which can be used to describe light by a single *scalar* function. This theory is then in turn used to derive scalar *diffraction* and scalar *scattering* integrals, which will form the basis for the discussion of planar and volume HOEs respectively. In the final step the proposed approach is described in details. Below is a brief overview of the contents of the individual chapters.

Starting with the derivation of the Helmholtz equation and the inhomogeneous wave equation, the basis of scalar diffraction theory and scalar theory of scattering are presented in chapter 2. The integral form of the linearized inhomogeneous wave equation is then derived and applied in chapter 3. For this purpose the weak scattering approximation is applied in deriving the relationship between the scattered wave field and the scattering potential. In chapter 4 the motivation behind this thesis is articulated and the hypothesis that forms the basis of this work is formulated.

Chapter 5 focuses on the design and realization of computer generated volume holograms. It starts by presenting a rigorous analysis of methods available in the current state of the art. This analysis is then applied to derive a model upon which the proposed novel approach is based. Both Rytov and Born approximation based models and their corresponding optimization algorithms are then compared by means of numerical studies in this chapter. The hybrid algorithm developed in the course of this work and the relevance, as well as the applicability of all the constraints implemented therein are then discussed in details.

Chapter 6 is dedicated to the experimental proof of the proposition stated in chapter 4. A laser lithographic method for the fabrication of CGVHs in a nonlinear optical material is discussed. For this purpose, the nonlinear wave equation which is derived in chapter 2 is applied. The fabricated holograms are then characterized by determining the achievable diffraction efficiency and an improvement in the quality of projected far-field distribution is demonstrated. The thesis is summarized in chapter 7 and an outlook for future research is presented.

2. Theoretical Background: Holographic Optical Elements

A holographic optical element (HOE) is an optical element - e.g. a lens, filter, beam splitter, diffuser, or diffraction grating - that can be described using the principle of holographic imaging processes [2]. Conventional HOEs are optically recorded or numerically computed and then transferred into a suitable dielectric medium. Thereby, the basic principle of holography which essentially consists in the transformation of phase changes into *recordable* intensity changes is utilized. HOEs are applied in diverse fields of modern physical optics to modulate light fields in order to acquire transformations thereof, some being analogous to the transformations carried out by classical elements and others being specific transformations determined by the possibilities of holography [60, 61]. It follows from this, that in order to gain a good insight on HOEs, a deeper understanding of the basic theory that governs the interaction of light with material in general is needed.

In the next two sections Maxwell's equations are introduced and used to present a description of light as electromagnetic radiation, which propagates in the form of two mutually coupled vector waves consisting of an electric-field and a magnetic-field. Thereby, *wave optics theory* is first introduced as an approximation of the electromagnetic theory to describe light by a single *scalar* function. In this simple case, Maxwell's equations are formulated for a medium that is isotropic, linear and non-conducting. Wave optics theory will in turn be applied in Sect. 2.3 to derive the *scalar diffraction integral* which is commonly adopted when considering planar HOEs. Furthermore, Maxwell's equations for a nonlinear, homogeneous as well as inhomogeneous dielectric medium will be considered. The former case will be encountered in chapters 3 and 5 while discussing propagation of light through a volume HOE. The latter case will, on the other hand, form the basis for the discussion of the fabrication of volume HOEs in nonlinear optical material by means of femtosecond laser lithography. The main aim of this chapter is therefore to form a basis for the description of light propagation, scattering and absorption in different media.

2.1. Theory of Electromagnetic Waves

The phenomena of scattering and absorption of *weak* electromagnetic waves, i.e. where the electric vector of the electromagnetic field is *small*, in any given medium plays a crucial role in many fields of science. It can for example be inferred directly from the basic theory of electromagnetic waves that a parallel beam of light will traverse

through vacuum without any energy loss. However, it will for instance interact through absorption and/or scattering with an inhomogeneous medium thereby partially or fully losing its energy. The energy of the incident beam is thus reduced by an amount equal to the sum of absorbed and scattered energy. This reduction is commonly referred to as extinction. In the next two chapters the theoretical background behind scattering and extinction of light traversing a given medium is presented. Of particular interest in this work are non scattering and weakly scattering homogeneous, as well as inhomogeneous dielectric media which are characterized by their index of refraction. Specifically, propagation of light and the dependence of the scattering interaction on the magnitude and distribution of the refractive index within such a medium, which is embedded in a homogeneous background, is discussed in details. This discussion will essentially form the foundation of this work and the basis for the derivation of the aforementioned forward and inverse problems in holography.

If on the other hand the electric vector of the electromagnetic field is *large* enough, the alternating electric field will induce a nonlinear polarization in the medium. This leads to an excitation of higher harmonics, and hence to interactions that result in to *wave mixing processes* [62]. In the following sections wave mixing processes will be discussed in further details. It will be shown that they correspond to different nonlinear effects, whereby the order of nonlinearity depends on the magnitude of the electric field and on the material in question. One such nonlinear process, which will be of particular interest in this work, is multi-photon absorption process (MPA).

2.1.1. Maxwell's Equations

Within the theory of quantum optics light is found to depict both particle-like and wave-like properties. However, many optical phenomena can adequately be described using the theory of electromagnetic waves which was put forward by James Clerk Maxwell in 1865. In this case an electromagnetic field is described by two related vector fields: the electric field $\boldsymbol{\mathcal{E}}(\boldsymbol{r}, t)$ and the magnetic field $\boldsymbol{\mathcal{H}}(\boldsymbol{r}, t)$. Both are vector functions of position $\boldsymbol{r}$ and time t. For a medium that is free of charges and imposed currents, the propagation behavior of electromagnetic fields is fundamentally governed by the following Maxwell's equations [2, 63]

$$\nabla \cdot \boldsymbol{\mathcal{D}} = 0 \tag{2.1}$$

$$\nabla \cdot \boldsymbol{\mathcal{B}} = 0 \tag{2.2}$$

$$\nabla \times \boldsymbol{\mathcal{H}} = \frac{\partial \boldsymbol{\mathcal{D}}}{\partial t} \tag{2.3}$$

$$\nabla \times \boldsymbol{\mathcal{E}} = -\frac{\partial \boldsymbol{\mathcal{B}}}{\partial t}, \tag{2.4}$$

where $\boldsymbol{\mathcal{D}}(\boldsymbol{r}, t)$ is the electric flux density and $\boldsymbol{\mathcal{B}}(\boldsymbol{r}, t)$ the magnetic flux density. When dealing with materials having distinct properties it is important to consider the relationship between the flux densities and the fields, i.e. between $\boldsymbol{\mathcal{D}}$ and $\boldsymbol{\mathcal{E}}$ as well as between $\boldsymbol{\mathcal{B}}$ and $\boldsymbol{\mathcal{H}}$. This relationship is characterized by the polarization density

$\mathcal{P}(\boldsymbol{r}, t)$ in the former case and the magnetization polarization density $\mathcal{M}(\boldsymbol{r}, t)$ in the latter. It can be described using the following material equations

$$\mathcal{D} = \epsilon_o \mathcal{E} + \mathcal{P} \tag{2.5}$$
$$\mathcal{B} = \mu_o \mathcal{H} + \mu_o \mathcal{M}. \tag{2.6}$$

Hereby, ϵ_o and μ_o are, respectively, the free space or vacuum permittivity and permeability. In free space $\mathcal{P}$ and $\mathcal{M}$ are equal to zero and thus $\mathcal{D} = \epsilon_o \mathcal{E}$ and $\mathcal{B} = \mu_o \mathcal{H}$ whereupon Eqs. (2.1) to (2.4) become free space Maxwell's equations [63]:

$$\nabla \cdot \mathcal{E} = 0 \tag{2.7}$$
$$\nabla \cdot \mathcal{H} = 0 \tag{2.8}$$
$$\nabla \times \mathcal{H} = \epsilon_o \frac{\partial \mathcal{E}}{\partial t} \tag{2.9}$$
$$\nabla \times \mathcal{E} = -\mu_o \frac{\partial \mathcal{H}}{\partial t}. \tag{2.10}$$

Maxwell's equations will be used in this thesis while considering propagation of light in free space as well as in dielectric media have particular properties as it is explained in the next section.

One significant property of electromagnetic waves is that they transport energy and momentum. Therefore, further insight on the physical properties of optical waves can be gained by considering the energy flow connected with the propagation of an electromagnetic wave, which is described by the Poynting vector

$$\mathcal{S} = \mathcal{E} \times \mathcal{H}. \tag{2.11}$$

Thus $\mathcal{S}$ is a *power density vector* which specifies both the power density in Watts per square meter, and the *direction* of flow. Let us for instance consider a monochromatic plane wave, which is an elementary solution of the Maxwell's equations. We start by adopting the complex representation of the field components as follows,

$$\mathcal{E}(\boldsymbol{r}, t) = \text{Re}\left\{\boldsymbol{E}(\boldsymbol{r})\exp(i\omega t)\right\} \tag{2.12}$$
$$\mathcal{H}(\boldsymbol{r}, t) = \text{Re}\left\{\boldsymbol{H}(\boldsymbol{r})\exp(i\omega t)\right\}, \tag{2.13}$$

whereby $\boldsymbol{E}(\boldsymbol{r})$ and $\boldsymbol{H}(\boldsymbol{r})$ represent electric and magnetic field complex amplitude vectors respectively; and ω the angular frequency. The complex Poynting vector of such fields can be expressed as

$$\boldsymbol{S} = \boldsymbol{E} \times \boldsymbol{H}. \tag{2.14}$$

Given the complex representation of the field components, a monochromatic electromagnetic wave whose electric and magnetic field components are plane waves of wave vector $\boldsymbol{k}$ can be expressed as

$$\boldsymbol{E}(\boldsymbol{r}) = \boldsymbol{E}_o \exp(-i\boldsymbol{k} \cdot \boldsymbol{r}) \tag{2.15}$$
$$\boldsymbol{H}(\boldsymbol{r}) = \boldsymbol{H}_o \exp(-i\boldsymbol{k} \cdot \boldsymbol{r}), \tag{2.16}$$

where $\boldsymbol{E}_o$ and $\boldsymbol{H}_o$ are constant vectors. From Eqs. (2.14), (2.15) and (2.16); the complex Poynting vector of such a plane wave is given by

$$S = \frac{1}{2}\boldsymbol{E} \times \boldsymbol{H}^*, \qquad (2.17)$$

where (*) denotes complex conjugation. The direction of $\boldsymbol{S}$ in this case indicates the direction of instantaneous power flow as we would expect i.e., it is normal to both $\boldsymbol{E}$ and $\boldsymbol{H}$ at any point.

Since optical waves have very large temporal frequencies lying in the range of several hundred terahertz, optical detectors can only register the time-average of the power flow which is given by the real part of the complex Poynting vector, i.e. the *irradiance* [64]

$$\tilde{I} = |\langle \boldsymbol{S} \rangle| = \frac{\varepsilon}{\mu}\frac{E_o^2}{2} \qquad (2.18)$$

In the course of this work we will only consider absolute measurements of the irradiance for time independent optical fields. Thus the constants in Eq. (2.18) will be omitted and the following simplified equation for the irradiance, which we will refer to as the *intensity*, will be adapted

$$I = |\boldsymbol{E}|^2 = E_o^2. \qquad (2.19)$$

2.1.2. Electromagnetic Waves in Dielectric Media

In the course of this work dielectric materials having different properties are considered. We assume that all the materials considered here are nonmagnetic. In order to describe the interaction of light with any of these materials, a brief discussion on the response of the given material to an electric field is presented. For instance, in chapter 3 we will deal primarily with linear media. A *linear* medium is one in which the polarization produced by an applied electric or magnetic field is proportional to that field i.e. the vector field $\boldsymbol{\mathcal{P}}(\boldsymbol{r}, t)$ is linearly related to $\boldsymbol{\mathcal{E}}(\boldsymbol{r}, t)$. Given the fact that interatomic electric fields are of the order of 10^{11} Vm^{-1}, the electric fields used in the course of this work (which are of the order $< 10^8$ Vm^{-1}) are small in comparison, and their effects are consequently linear. The oscillating fields produced by intense laser beams are often orders of magnitude larger and can cause nonlinear response [65]. Such a nonlinear process will be discussed in chapter 6.

Electromagnetic waves in linear, homogeneous, nondispersive and isotropic dielectric media

The simplest case considered in this thesis is when light propagates through free space or through linear, homogeneous, nondispersive and isotropic media. Such case is encountered for instance while considering the background dielectric medium within which a given HOE is embedded. Thereby, the vectors $\boldsymbol{\mathcal{P}}$ and $\boldsymbol{\mathcal{E}}$ at every position and time are then parallel and proportional, so that

$$\boldsymbol{\mathcal{P}} = \epsilon_o\chi\boldsymbol{\mathcal{E}}, \qquad (2.20)$$

where χ the electric susceptibility. By substituting (2.20) into (2.5) we arrive at

$$\boldsymbol{\mathcal{D}} = \epsilon \boldsymbol{\mathcal{E}}, \tag{2.21}$$

where the permittivity of the medium is defined as follows

$$\epsilon = \epsilon_o (1 + \chi). \tag{2.22}$$

The polarizability of such a medium, which is defined physically as the ratio of the dipole moment induced to the electric field that produces it, can in turn be expressed by the dielectric constant;

$$\epsilon_r = \frac{\epsilon}{\epsilon_o} = 1 + \chi, \tag{2.23}$$

i.e. its relative permittivity. The polarizability of a given dielectric material plays an important role in holography. For instance, holographic information can be stored in such a medium by means of small changes in the dielectric constant of a polymeric material [66]. In the course of this work we considered mainly pure phase photosensitive glass ceramics, whereby such a change is induced during exposure to light as it will be discussed in latter sections.

In a similar way to Eq. (2.21), given the permeability of the medium μ, the magnetic relation can be written in the form of

$$\boldsymbol{\mathcal{B}} = \mu \boldsymbol{\mathcal{H}}. \tag{2.24}$$

Given Eqs. (2.20) and (2.21) as well as the general form of Maxwell's equations in Eqs. (2.1) - (2.4); we can derive the following Maxwell's equations for a linear, homogeneous, nondispersive and isotropic medium,

$$\nabla \cdot \boldsymbol{\mathcal{E}} = 0 \tag{2.25}$$

$$\nabla \cdot \boldsymbol{\mathcal{H}} = 0 \tag{2.26}$$

$$\nabla \times \boldsymbol{\mathcal{H}} = \epsilon \frac{\partial \boldsymbol{\mathcal{E}}}{\partial t} \tag{2.27}$$

$$\nabla \times \boldsymbol{\mathcal{E}} = -\mu \frac{\partial \boldsymbol{\mathcal{H}}}{\partial t}. \tag{2.28}$$

It is apparent that Eqs. (2.25) - (2.28) are identical in form to the free space Maxwell's equations in Eqs. (2.7) - (2.10), except that in this case ϵ and μ replace ϵ_o and μ_o respectively. It is important to mention here that one necessary condition for $\boldsymbol{\mathcal{E}}$ and $\boldsymbol{\mathcal{H}}$ to satisfy Maxwell's equations is that each of their components satisfy the wave equation [63]

$$\nabla^2 u(\boldsymbol{r}, t) - \frac{1}{c^2} \frac{\partial^2 u(\boldsymbol{r}, t)}{\partial t^2} = 0, \tag{2.29}$$

where the speed of the propagating optical wave in this medium is given by

$$c = \frac{1}{\sqrt{\epsilon \mu}} \tag{2.30}$$

and the scalar function $u(\boldsymbol{r}, t)$ represents any of the three components $(\mathcal{E}_x, \mathcal{E}_y, \mathcal{E}_z)$ of $\boldsymbol{\mathcal{E}}$ or the three components $(\mathcal{H}_x, \mathcal{H}_y, \mathcal{H}_z)$ of $\boldsymbol{\mathcal{H}}$. From above we conclude that in a dielectric medium that is linear, isotropic, homogeneous, and nondispersive, all components of the electric and magnetic field behave identically and their behavior is fully described by a single scalar wave equation [2, 63].

Here we will assume that the medium at hand is nonmagnetic, which implies that $\mu = \mu_o$. This is a valid assumption since most of the material encountered in the course of this work are nonmagnetic. It follows from this that the ratio between the velocity of the optical waves in vacuum and the given medium is defined as the refractive index

$$n = \sqrt{\epsilon_r}, \tag{2.31}$$

whereby, as priorly mentioned, ϵ_r is the material specific dielectric constant - see Eq. (2.23). The response of different media encountered in this work to electromagnetic waves, as it can be expressed using Eq. (2.31), will play quite crucial role. However, in Eq. (2.31) ϵ_r it is presumed to be a *static* constant. For the majority of the material considered here ϵ_r, and therefore n, will be position and frequency dependent as it is discussed in later sections. The frequency dependence of n leads to dispersion. Additionally, as an electromagnetic wave traverses through a given medium a portion of it will always be attenuated. Thus in general, such a wave is taken to be traveling through a medium with a complex index of refraction

$$\tilde{n} = n + \mathrm{i}\kappa. \tag{2.32}$$

The imaginary part of the complex refractive index $\kappa = \mathrm{Im}\,\{\tilde{n}\}$ is commonly referred to as the *absorption coefficient* and it determines the amount of absorption loss as the wave traverses through the material.

Electromagnetic waves in linear, *inhomogeneous*, nondispersive and isotropic dielectric media

One deviation from the ideal uniform dielectric medium described above occurs when the medium is inhomogeneous. This implies that the relationship between $\boldsymbol{\mathcal{P}}$ and $\boldsymbol{\mathcal{E}}$ is dependent on $\boldsymbol{r}$. Such a medium will be encountered in this thesis while describing propagation of light in the bulk of volume HOEs. In such a case the relations in Eqs. (2.20) and (2.21) remain intact, but both the susceptibility and the permittivity become functions of position: $\chi = \chi(\boldsymbol{r})$ and $\epsilon_r = \epsilon(\boldsymbol{r})/\epsilon_o$. Hence also the refractive index becomes position dependent, so that $n = n(\boldsymbol{r})$. We can then show that the wave equation satisfied by $\boldsymbol{\mathcal{E}}$ becomes

$$\nabla^2 \boldsymbol{\mathcal{E}} - \mu_o \epsilon(\boldsymbol{r}) \frac{\partial^2 \boldsymbol{\mathcal{E}}}{\partial t^2} + \nabla \left(\frac{1}{\epsilon(\boldsymbol{r})} \nabla \epsilon(\boldsymbol{r}) \cdot \boldsymbol{\mathcal{E}} \right) = 0. \tag{2.33}$$

In order to derive this *inhomogeneous wave equation* from the Maxwell's equations in Eqs. (2.1) - (2.4), we can apply the curl operation $\nabla \times$ to both sides of Eq. (2.4). By then noting that $\epsilon = \epsilon(\boldsymbol{r})$ and invoking the identities

$$\nabla \times (\nabla \times \boldsymbol{\mathcal{E}}) = \nabla(\nabla \cdot \boldsymbol{\mathcal{E}}) - \nabla^2 \boldsymbol{\mathcal{E}} \tag{2.34}$$

and

$$\nabla \cdot \epsilon \boldsymbol{\mathcal{E}} = \epsilon \nabla \cdot \boldsymbol{\mathcal{E}} + \nabla \epsilon \cdot \boldsymbol{\mathcal{E}}; \qquad (2.35)$$

Eqs. (2.1),(2.3), (2.21) and (2.24) can be used to arrive at Eq. (2.33) [63]. A detailed derivation of this equation is presented in appendix A.1. From this inhomogeneous wave equation we can see that for a medium whose dielectric properties do not change over space, the third term on the left side of Eq. (2.33) is zero and hence Eq. (2.33) will take the form of Eq. (2.29). This term will however be nonzero for instance for a medium with a refractive index that changes over space, i.e.

$$n(\boldsymbol{r}) = \sqrt{\epsilon(\boldsymbol{r})/\epsilon_o}. \qquad (2.36)$$

Such material will be encountered in this work while describing light propagation in a CGVH. Specifically, we will assume the holograms can be described as a medium whereby $\epsilon(\boldsymbol{r})$ varies much slower than $\boldsymbol{\mathcal{E}}(\boldsymbol{r})$, i.e. $\epsilon(\boldsymbol{r})$ does not vary within a distance of one wavelength. In this case the third term in Eq. (2.33) maybe neglected so that the wave equation

$$\nabla^2 \boldsymbol{\mathcal{E}} - \mu_o \epsilon(\boldsymbol{r}) \frac{\partial^2 \boldsymbol{\mathcal{E}}}{\partial t^2} = 0 \qquad (2.37)$$

is approximately applicable for such an inhomogeneous medium. Thus, Eq. (2.37) will then be applied in Sect. 3.2 while discussing scalar scattering theory and in Sect. 5.1 to derive an advanced scattering model which forms the basis of this work. Thereby, it will be shown that this term introduces a coupling between the various components of the electric field.

Electromagnetic waves in *nonlinear*, homogeneous, nondispersive and isotropic dielectric media

Nonlinear dielectric media will be encountered in Sect. 6.1 while discussing laser lithography based micro- and nanofabrication of HOEs. A nonlinear medium is defined as a medium whereby the relationship between $\boldsymbol{\mathcal{P}}$ and $\boldsymbol{\mathcal{E}}$ is nonlinear. In analogy to to the inhomogeneous wave equation presented above, a *nonlinear wave equation* can be derived from the Maxwell's equations - Eqs. (2.1) - (2.4), as it is shown in appendix A.2, to arrive at

$$\nabla^2 \boldsymbol{\mathcal{E}} - \mu_o \epsilon_o \frac{\partial^2 \boldsymbol{\mathcal{E}}}{\partial t^2} = \mu_o \frac{\partial^2 \boldsymbol{\mathcal{P}}}{\partial t^2}. \qquad (2.38)$$

This nonlinear wave equation, as opposed to the linear wave equation in (2.29), contains an extra term that arises from the nonlinear polarization. This term is again responsible for energy transfer between coupled propagating waves in the medium.

An electromagnetic wave incident on a nonlinear medium will polarize it causing it to develop a time dependent electrical polarization $\boldsymbol{\mathcal{P}}(t)$. The resulting polarization can be considered to be made of several contributions, which are represented by terms consisting of products of higher order susceptibility $\chi^{(n)}$ and the magnitude of

the electric field $\mathcal{E}(t)$ [62]. This leads to the aforementioned wave mixing processes. Thereby, the ith component of $\mathcal{P}(t)$, where i stands for (x, y, z) is given by

$$\mathcal{P}_i = \epsilon_o \left\{ \chi_{ij}^{(1)} \mathcal{E}_j + \chi_{ijk}^{(2)} \mathcal{E}_j \mathcal{E}_k + \chi_{ijkl}^{(3)} \mathcal{E}_j \mathcal{E}_k \mathcal{E}_l + \cdots \right\}, \tag{2.39}$$

where $\chi^{(n)}$ is a tensor of rank $(n+1)$ with $3^{(n+1)}$ [62] components in general. This mathematical formalism will be adopted in Sect. 6.1. to present an elaborate description of the physical processes behind fabrication of CGVHs by means of optically induced refractive index modulation using non-linear absorption of near infrared light in glass ceramics.

2.2. Time Independent Wave Equation

2.2.1. Helmholtz Equation

In the first two chapters of this thesis we will mainly be interested in situations where the time-dependency of electromagnetic waves does not play a role. In what follows, we use a scalar representation of the wave field by using a single component. Furthermore, monochromatic electromagnetic waves will be of particular interest in this work, mainly owing to the fact that only laser light is considered. Thus, we will assume that only quasi-monochromatic light having a single frequency ν and corresponding angular frequency $\omega = 2\pi\nu$ is used. For such waves, we can consider the following solution of the wave equation in Eq. (2.29)

$$u(\boldsymbol{r}, t) = A(\boldsymbol{r}) \cos\left(\omega t + \phi(\boldsymbol{r})\right) = \mathrm{Re}\left\{U(\boldsymbol{r}) \exp\left(\mathrm{i}\omega t\right)\right\}, \tag{2.40}$$

where $A(\boldsymbol{r})$ is the amplitude and $\phi(\boldsymbol{r})$ the phase. The complex amplitude is given by

$$U(\boldsymbol{r}) = A(\boldsymbol{r}) \exp\left(\mathrm{i}\phi(\boldsymbol{r})\right), \tag{2.41}$$

By substituting $u(\boldsymbol{r}, t)$ into the wave equation - Eq. (2.29), it follows that U must obey the time-independent *Helmholtz equation*

$$(\nabla^2 + k^2)U(\boldsymbol{r}) = 0, \tag{2.42}$$

whereby

$$k = 2\pi/\lambda \tag{2.43}$$

is the wave number and λ the wavelength in the given dielectric medium [2]. The Helmholtz equation is valid for all waves satisfying the scalar wave equation.

2.2.2. Elementary Plane Waves

One of the simplest solution of the Helmholtz equation is a stationary plane wave. For the monochromatic optical wave field introduced in Eq. (2.15) this solution of the scalar wave equation can be written as follows

$$U(\boldsymbol{r}) = A \exp(-\mathrm{i}\boldsymbol{k} \cdot \boldsymbol{r}), \tag{2.44}$$

where A is a complex constant and $\boldsymbol{k} = (k_x, k_y, k_z)^T$ is a vector in spatial frequency space [64]. This equation satisfies Eq. (2.42) as long as

$$k^2 = k_x^2 + k_y^2 + k_z^2. \tag{2.45}$$

An illustration of a numerically simulated plane wave traveling in the direction parallel to the z-direction is shown in Fig. 2.1 *(a)*. The set of all solutions corresponding to a given k apparently represents a sphere with a radius $k = 2\pi/\lambda$ in three dimensional frequency space, the so called *Ewald's sphere* [67] - *cf.* Fig. 2.1 *(b)*. Here, k is given by Eq. (2.43). It follows therefore that the components of $\boldsymbol{k}$ are not independent of one another. Thus k_z is conventionally chosen to be the dependent variable so that $k_z^2 = k^2 - k_x^2 - k_y^2$ [68].
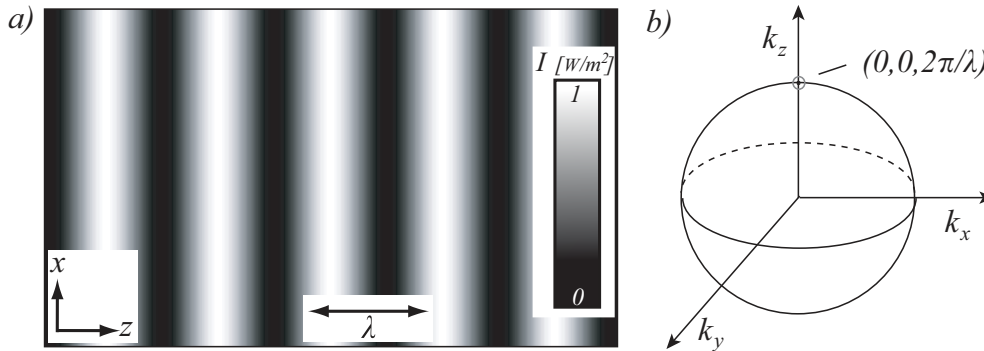
Figure 2.1.: (a) Illustration of a numerically simulated plane wave traveling in the direction normal to the x- and y-axis. (b) In the frequency space this plane wave is represented by a point at the position $(0, 0, 2\pi/\lambda)$ and lies on the surface of a sphere of radius $2\pi/\lambda$ - the *Ewald's sphere*.

2.3. Scalar Diffraction Theory and its Application in Holography

A major portion of holography is devoted to the consideration of numerically computed holographic optical elements, which are used to manipulate wave fields by means of diffraction. Such diffractive optical elements are commonly referred to as computer generated holograms [69]. A significant amount of study has been devoted to methods for numerically designing CGHs. The advantage gained by such a process is that one can generate arbitrary 2D or 3D wave field distributions. One is then only limited by the ability to describe these holograms mathematically, to compute them numerically in a reasonable amount of time and to fabricate them [2]. In this section the design theory behind the computation and fabrication of CGHs, which are considered to be thin diffractive optical elements is discussed. In particular, an analysis of phase-only CGHs and their characteristics is presented. We will assume that the structure of these

elements is defined by the modulation of the index of refraction of a given dielectric medium. This theory will then be generalized in the subsequent sections to include the design of volume holographic optical elements.

Scalar theory of diffraction is commonly adopted when considering thin diffractive optical elements, whereby the assumptions discussed in Sect. 2.2.1. are presumed to be fulfilled. Scalar diffraction theory involves the conversion of the wave equation (cf. Eq. (2.42)) from a partial differential equation into an integral equation. By treating diffraction problems as boundary-value problems, this integral transform formulation of diffraction theory can be derived without approximations [70]. Thus scalar diffraction theory can be used to analyze most types of diffraction phenomena and imaging systems within its realm of validity [71]. It offers a useful simplification of rigorous vector diffraction theory yet retains important features that allow for the treatment of diffraction and scattering in terms of linear system theory [72]. In this section scalar diffraction theory is used to derive some important tools. These tools are some of the cornerstones of Fourier optics and will form a basis for the work presented in this thesis.

2.3.1. Rayleigh-Sommerfeld Diffraction Integral

A monochromatic light beam propagating in free space can be completely deduced from the values of that beam, which are known across a given single plane. In other words the field crosssection in any one transverse plane completely determines the field everywhere else [73]. This dependence provides a solution to the problem of finding the diffracted wave field due to a given object. The Rayleigh-Sommerfeld formulation of diffraction and its paraxial approximation are commonly used to solve this problem. Let us consider for instance the determination of the monochromatic optical field distribution across a distant observation plane $\{s\}$ from a given field distribution across a source plane $\{x\}$. At the source plane, which is located at $z = 0$, an area Σ defines the extent of a source or an illuminated aperture. The field distribution in the source plane is given by $U(x)$. The field $U(s)$ in a distant observation plane can be computed using the first Rayleigh-Sommerfeld diffraction formula [2, p. 49]

$$U(\boldsymbol{x}) = \frac{1}{\mathrm{i}\lambda} \iint_{\Sigma} U(\boldsymbol{s}) \frac{\exp\left(\mathrm{i}k\left|\boldsymbol{r}\right|\right)}{\left|\boldsymbol{r}\right|} \cos\left(\hat{\boldsymbol{e}} \cdot \boldsymbol{r}\right) \mathrm{d}\xi \mathrm{d}\eta. \tag{2.46}$$

Here, $\left|\boldsymbol{r}\right| = \sqrt{(\boldsymbol{s} - \boldsymbol{x})^2 + z_o^2}$ is the distance between a position on the source plane and a position in the observation plane whereas z_o is the distance between the centers of the source and observation plane. The vectors $\boldsymbol{s} = (\xi, \eta)^T$ and $\boldsymbol{x} = (x, y)^T$ represent points in the observation and source space respectively. Equation (2.46) is, assuming the fields $U(\boldsymbol{x})$ and $U(\boldsymbol{s})$ are defined across two parallel planes, a convolution integral which can be written as

$$U(\boldsymbol{x}) = \iint_{\Sigma} H(\boldsymbol{s} - \boldsymbol{x}) U(\boldsymbol{x}) \mathrm{d}\xi \mathrm{d}\eta, \tag{2.47}$$

where the impulse response $H(\boldsymbol{s} - \boldsymbol{x})$ has the general form [2, pp. 61]

$$H(\boldsymbol{s} - \boldsymbol{x}) = \frac{1}{i\lambda} \frac{\exp\left(ik\,|\boldsymbol{r}|\right)}{|\boldsymbol{r}|} \cos\left(\hat{\boldsymbol{e}} \cdot \boldsymbol{r}\right). \tag{2.48}$$

Fourier convolution theorem can be applied to rewrite Eq. (2.47) as a discrete shift-invariant convolution in a simplified form as follows

$$U(\boldsymbol{x}) = \mathscr{F}^{-1}\{\mathscr{F}\{U(\boldsymbol{s})\} \cdot \tilde{H}(\boldsymbol{q})\}. \tag{2.49}$$

Here, $\mathscr{F}\{\cdot\}$ and $\mathscr{F}^{-1}\{\cdot\}$ are the forward and inverse Fourier transform operators respectively whereas $\boldsymbol{q} = (f_x, f_y)^T$ is a vector representing spatial frequencies. The transfer function $\tilde{H}(\boldsymbol{q})$ of the wave propagation phenomenon, which is derived using an angular spectrum analysis is given by [71]

$$\tilde{H}(\boldsymbol{q}) = \begin{cases} \exp\left(ikz_o\sqrt{1 - (\lambda f_x)^2 - (\lambda f_y)^2}\right) & \text{if } \sqrt{f_x^2 + f_y^2} < 1/\lambda \\ 0 & \text{otherwise.} \end{cases} \tag{2.50}$$

With the assumption that $z_o \gg \lambda$, it is apparent that wave propagation in a homogeneous medium is equivalent to a linear 2D spatial filter with the band limited transfer function given by (2.50) [74, pp. 61]. Furthermore, it is clear that the effect of propagation is the modulation of the relative phases of various plane waves whereby their amplitudes remain unchanged.

Equation (2.46) forms the basis for the numerical forward and backward propagation of wave fields in digital holography for diverse applications ranging from holographic interferometry [75] to metrology [8], as well as for the design of holographic optical elements [69]. In the next section application of the concept introduced here in both conventional digital holography and in the design of computer generated holograms is discussed. In a later chapter this approach will be adopted to derive a more advanced mathematical model that is applied in the design of computer generated volume holograms.

2.3.2. Basic Principle of Digital Holography

Conventional holography can essentially be described as an interferometric approach for numerically recording and reconstructing the amplitude and phase of a complex wave field, either optically or numerically [18]. Once the wave field has been recorded, the resulting hologram can be transferred onto an appropriate substrate. This can then be used to modulate an impinging complex wave field with the aim of generating a desired wave field distribution across a given plane or region. These, among other applications of holograms, have made them versatile and widely applied optical elements in different fields of science. In this section a short overview of the basic concepts behind digital holography (DH) in specific as well as holography in general are presented. These concepts will be revisited in the subsequent sections where the topic of wave field synthesis by means of holographic optical elements is introduced.

The principle of the interference between two coherent monochromatic light waves emitted by the same source is utilized in DH to encode phase information into detectable intensity modulations. A digital hologram is thus recorded by coherently superposing a given wave field, e.g. originating from an object of interest, with a known reference wave. Let $U_r(\varphi_r)$, denote the complex amplitude of a plane reference wave, $U_o(\boldsymbol{s})$ that of the object wave and $\Delta\varphi(\boldsymbol{s}) = \varphi_o(\boldsymbol{s}) - \varphi_r$ the phase difference of these two waves. Furthermore, let us assume that an ideal unit amplitude plane reference wave is used so that from Eq. (2.41) we have $U_r(\varphi_r) = \exp(\mathrm{i}\varphi_r)$. The total field $U(\boldsymbol{s}) = U_r(\varphi_r) + U_o(\boldsymbol{s})$ across the hologram plane $\{\mathbf{s}\}$ is given in terms of the interference pattern

$$
\begin{aligned}
I(\boldsymbol{s}; \varphi_r) &= |U(\boldsymbol{s})|^2 \\
&= |U_o(\boldsymbol{s})|^2 + |U_r(\varphi_r)|^2 + U_o(\boldsymbol{s})U_r^*(\varphi_r) + U_r(\varphi_r)U_o^*(\boldsymbol{s}),
\end{aligned} \tag{2.51}
$$

where $(^*)$ denotes the complex conjugate. The desired object wave field can be reconstructed from one of the last two terms in Eq. (2.51), i.e. the interference terms between the object and the reference waves. These two terms are, to a good approximation, proportional to the original object field. Thus, the complex field across a given plane $\{\boldsymbol{x}\}$ in the object space can be reconstructed from the hologram using Eq. (2.46) as follows

$$
U(\boldsymbol{x}) = \frac{1}{\mathrm{i}\lambda} \iint_{\Sigma} I(\boldsymbol{s})U_r^*(\varphi_r)\frac{\exp(\mathrm{i}k\,|\boldsymbol{r}|)}{|\boldsymbol{r}|}\cos(\hat{\boldsymbol{e}}\cdot\boldsymbol{r})\mathrm{d}\xi\mathrm{d}\eta. \tag{2.52}
$$

However, the reconstructed wave will contain distortions arising mainly from the different interference terms in (2.51). This becomes apparent after inserting the general forms, $U_r(\varphi_r) = \exp(\mathrm{i}\varphi_r)$ and $U_o(\boldsymbol{s}) = A_o(\boldsymbol{s})\exp(\mathrm{i}\varphi_o)$, of the complex valued reference and object waves into Eq. (2.52) to arrive at

$$
I(\boldsymbol{s})U_r^*(\varphi_r) = \mathcal{A}\exp(-\mathrm{i}\varphi_r) + A_o\exp(-\mathrm{i}\varphi_o) + A_o^*\exp(\mathrm{i}(\varphi_o - 2\varphi_r)), \tag{2.53}
$$

for the first term within this integral. In Eq. (2.53) the first term, with $\mathcal{A} = 1 + |A_o(\boldsymbol{s})|^2$, represents the *zero-order* term. The second term will, upon reconstruction, form the *real image* which corresponds to a distorted version of the original object wave. On the other hand, the last term forms the *virtual image*. This last term is in the general case, i.e. where the amplitude of the reference wave is not unity, proportional to a scaled version of the original object wave. The scaling factor is in this case given by the magnitude of the reference wave [8]. Therefore, since the original wave front is only a part of the reconstruction the four terms in (2.51) have to be separated. A number of solutions to this problem have thus been developed for various applications. Two of the most common approaches for this task are [2]:

The temporal phase shifting method

This method is usually employed in the reconstruction of the so called Gabor holograms, whereby the *in-line setup* depicted in Fig. 2.2 *(a)* is used to record the holograms. In such a setup the reference wave and the object wave are collinearly incident

on the detector plane. In this approach, a set of intensities are recorded with known stepped phase differences. In a practical implementation of an in-line setup, a coherent beam is divided into two paths, one of which contains a transmitting or reflecting object and the other a phase shifting element, e.g. a piezoelectric transducer mirror. Such an in-line setup can be used to record a series of intensities from which the phase
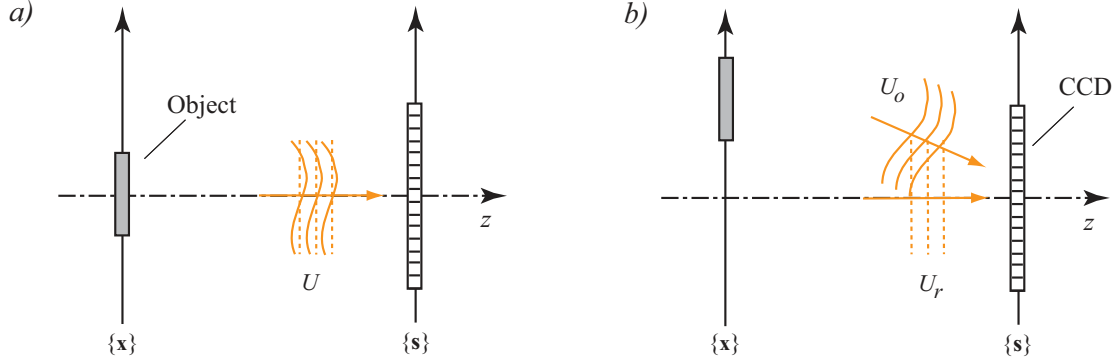
Figure 2.2.: Basic principle behind recording a digital hologram using *(a)* an in-line and *(b)* an off-axis setup. The hologram is hereby captured in form of an interference pattern between a given object field U_o and a reference field U_r using a CCD sensor.

and amplitude profiles of the object wave can then be extracted [75]. For instance in the so called four-step phase-shifting digital holography, four holograms are acquired with phase shifts of $\Delta\varphi = 0, \pi/2, \pi, 3\pi/2$ from which the phase

$$\Delta\varphi(\boldsymbol{s}) = \arctan\left[\frac{I_4(\boldsymbol{s}; 3\pi/2) - I_2(\boldsymbol{s}; \pi/2)}{I_1(\boldsymbol{s}; 0) - I_3(\boldsymbol{s}; \pi)}\right], \tag{2.54}$$

where the phase of the initial reference wave is assumed to be zero, and the amplitude

$$A_o(\boldsymbol{s}) = \frac{1}{4}\sum_{j}^{4} I_j(\boldsymbol{s}) \tag{2.55}$$

of the object wave can be recovered [76]. With this approach the contributions of the zero order term and the virtual image can be completely removed from the reconstruction. One of the main drawbacks of this method is the extended time needed to acquire a series of measurements, which makes it sensitive to vibrations and also leads to an elevated demand on the temporal coherency of the light.

The spatial phase shifting method

This method involves the introduction of a spatial carrier in order to spatially separate the real image from the virtual image and the zero order term [19, 77]. Practically this is realized using an off-axis setup like the one schematically depicted in Fig. 2.2 *(b)*.

To give a better insight on this method, we start by re-writing the hologram in Eq. (2.51) in terms of the intensities of the object and reference wave as follows

$$I_c(\boldsymbol{s}) = \mathcal{A}(\boldsymbol{s}) + 2\sqrt{I_o(\boldsymbol{s})I_r(\boldsymbol{s})}\cos\left[\Delta\phi(\boldsymbol{s}) + 2\pi\boldsymbol{q}_o\boldsymbol{s}\right]$$
$$= \mathcal{A}(\boldsymbol{s}) + \mathcal{B}(\boldsymbol{s})\exp\left[\mathrm{i}2\pi\boldsymbol{q}_o\boldsymbol{s}\right] + \mathcal{B}^*(\boldsymbol{s})\exp\left[-\mathrm{i}2\pi\boldsymbol{q}_o\boldsymbol{s}\right], \tag{2.56}$$

whereby in this case $\mathcal{A}(\boldsymbol{s}) = |U_o(\boldsymbol{s})|^2 + |U_r(\varphi_r)|^2$, $\mathcal{B}(\boldsymbol{s}) = \sqrt{I_o(\boldsymbol{s})I_r(\boldsymbol{s})}\exp\left[\mathrm{i}\Delta\phi(\boldsymbol{s})\right]$ and $\boldsymbol{q}_o$ is a known spatial carrier. By now taking the Fourier transform of Eq. (2.56) with respect to $\boldsymbol{s}$ we acquire

$$\tilde{I}_c(\boldsymbol{q}) = \tilde{\mathcal{A}}(\boldsymbol{q}) + \tilde{\mathcal{B}}(\boldsymbol{q} + \boldsymbol{q}_o) + \tilde{\mathcal{B}}^*(\boldsymbol{q} - \boldsymbol{q}_o), \tag{2.57}$$

where $\boldsymbol{q}$ denotes 2D spatial frequencies and the tilde is used to denote the Fourier transform of the individual terms. Given Eq. (2.57) the sought object field can be recovered from $I_c(\boldsymbol{s})$ using the *spatial filtering* method.

Considering the spectrum of the hologram $\tilde{I}_c(\boldsymbol{q})$ in Fig. 2.3, it is clear that one can extract any of the first order terms by means of spatial filtering using an appropriate mask as shown in Fig. 2.3. Thus an appropriate spatial carrier has to be chosen such that the term in question lies within the window W. Furthermore, the spectrum must be sampled adequately so that aliasing does not occur. After application of the spatial filter the retained frequencies can then be shifted into the center of the spectrum in order to obtain the appropriate dimensions for the reconstruction. Finally, Eq. (2.46) is applied to propagate the resulting field in order to numerically reconstruct the object field across the desired plane [8].
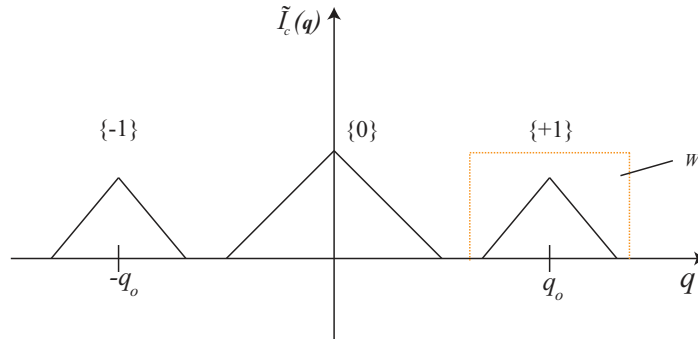
Figure 2.3.: Schematic representation of the spectrum of a hologram $\tilde{I}_c(\boldsymbol{q})$, whereby a spatial carrier of $\boldsymbol{q}_o$ is used to separate the virtual image $\{-1\}$ and the real image $\{+1\}$ of the object from the zero order term $\{0\}$.

Space-Bandwidth Product Analysis in Digital Holography

It is crucial to analyze the information capacity of a digital holographic system. This is usually done in terms of space-bandwidth product (SBWP). As a physical quantity, SBWP can be applied to characterize the capability of the system in capturing,

transferring and/or processing information. In digital holography, SBWP is defined as a parameter that allows for analysis of the information capacity of a given DH system either in the recording or reconstruction step. Thereby, the SBWP of a wave field within the system is defined by the location $\boldsymbol{x}$ and the spatial frequency bandwidth $\Delta\boldsymbol{q}$, i.e. the range of frequencies within which the field is non-zero, and can be expressed as [21, 78]

$$\text{SBWP} = \boldsymbol{x}\Delta\boldsymbol{q}. \tag{2.58}$$

The concept of SBWP can for instance be used to characterize the performance of the in-line and off-axis approach based DH systems discussed above. The temporal phase shifting method is thereby seen to offer better spatial resolution in the recording step as compared to the spatial phase shifting method. This is attributed to the fact that the spatial filter introduces an inherent spatial frequency bandwidth limitation. The off-axis approach thus yields a reconstruction with a poorer resolution than the intrinsic sensor resolution owing to the discarded high-frequency components. Herein lies the principle limitation of this method since this translates to a severe limit in the space-bandwidth product of the holographic system as it can be inferred from Eq. (2.58). This concept of SBWP will be used in later sections while assessing the information capacity of volume holographic element based systems.

2.3.3. Computer Generated Holograms (CGHs)

A CGH is a holographic optical element that is designed with a numeric optimization procedure and fabricated by means of micro-fabrication tools. Essentially, CGHs are holographic optical elements that are mainly used to modulate a complex wave field incident across a given plane $\{\boldsymbol{x}\}$, with the aim of generating a desired field distribution across a certain remote plane $\{\boldsymbol{s}\}$ as shown in Fig. 2.4. One main advantage of CGHs, as compared to conventional holograms, is that they allow for the use of a wide range of optical materials as a holographic storage medium, other than holographic plates or electronic devices. Additionally, unlike the conventional digital holograms discussed in Sect. 2.3.2., the numerical design and optimization of CGHs allows for the use of ideal wave fronts during encoding. Furthermore, the appropriate encoding strategy can be chosen for any given application. This in turn means that typical problems such as aberrations of the optical system, vibrations, thermal instabilities etc; that arise during the optical recording step in conventional holography can be avoided [23]. However, in analogy to conventional DH the reconstruction and decoding step is performed optically. Thus, the concepts of DH discussed above are adopted during the design and optimization of CGHs.

In this section an overview on computer generated holograms is presented. A generalized design approach, which can also be adopted to design and optimize holographic optical elements is presented in the next chapter. Therein, it will be shown that CGHs can be regarded as planar HOEs, which represents a special case of volume holographic optical element whose thickness is negligibly small. Here, key concepts such as the sampling and encoding of complex field distributions into fabricable discrete
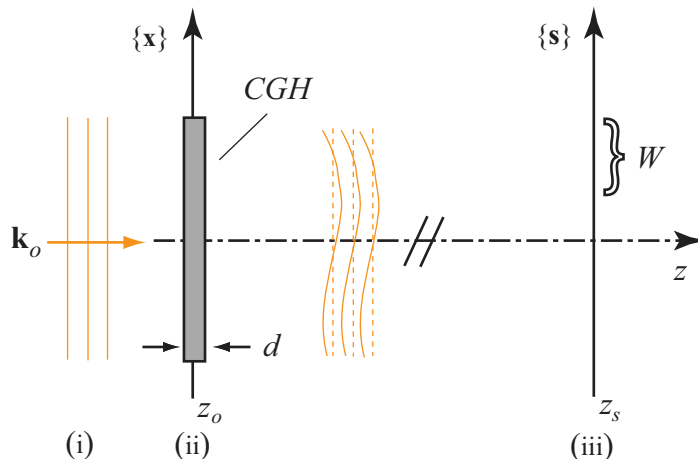
elements will also be introduced.

Figure 2.4.: Basic setup of the problem under consideration: a wave field U_o originating from region (i) propagates through a planar CGH which is located at the position $z = z_o$ and whose thickness is considerably small. This field is transformed into a total field $U = U_o + U_s$ by the CGH. This resulting field is assumed to be known in region (iii) across a remote plane $\{s\}$.

Computer generated holograms can generally be described as planar holographic elements, having a finite thickness d and a transmittance $\tau(\boldsymbol{x})$ which determines their optical functionality. This transmittance function is discretized into $N \times M$ pixels in order to allow numerical optimization. Thereby, the complex amplitude across either the CGH or reconstruction plane is also regarded as a distribution of discrete samples on a periodically extended rectangular grid of infinite extension. Thus as a result of numerical implementation, the sought discrete complex transmittance $\tau(n, m)$ is a sampled version of an unknown continuous function $\tau(\boldsymbol{x})$ [32]:

$$\tau(n, m) = \tau(\boldsymbol{x}) \sum_{i=0}^{N} \sum_{j=0}^{M} \delta \left(n\Delta x_i - x_i, m\Delta x_j - x_j \right). \tag{2.59}$$

Here, x_i and x_j are the components of $\boldsymbol{x}$ whereas Δx_i and Δx_j are the sampling distances in the $i-$ and $j-$ directions respectively. Once a solution $\tau(n, m)$ has been acquired by means of an iterative optimization algorithm [24, 79], numerous methods can be employed to fabricate the CGH. These methods include plotting techniques, direct laser writing, mask lithography laser and electron-beam lithography [23]. The choice of fabrication method dictates the approach that can be adopted to encode the complex transmittance $\tau(n, m)$. The choice can be *phase-only*, *amplitude-only* or *complex* encoding [69]. Encoding translates directly into physical constraints. For instance, pure phase-only elements are advantageous since they only modify the phase of an impinging field while transmitting all the power.

However, they rely on an inefficient encoding scheme since the field across the CGH plane has to be converted into pure phase information. Furthermore, in order for such a

CGH to be fabricable, the phase levels are constrained to C levels that can actually be fabricated with the target fabrication tool. In the case of electron-beam lithography or direct laser writing, binary encoding is thus usually adopted. In Fig. 2.5 *(a)* an example of a binary coded phase-only CGH, which was designed using an iterative Fourier transform algorithm [80], is shown. In this case the phase values are allowed to take on only either $+\pi$ or $-\pi$ values (see also Sect. 3.4.2.).
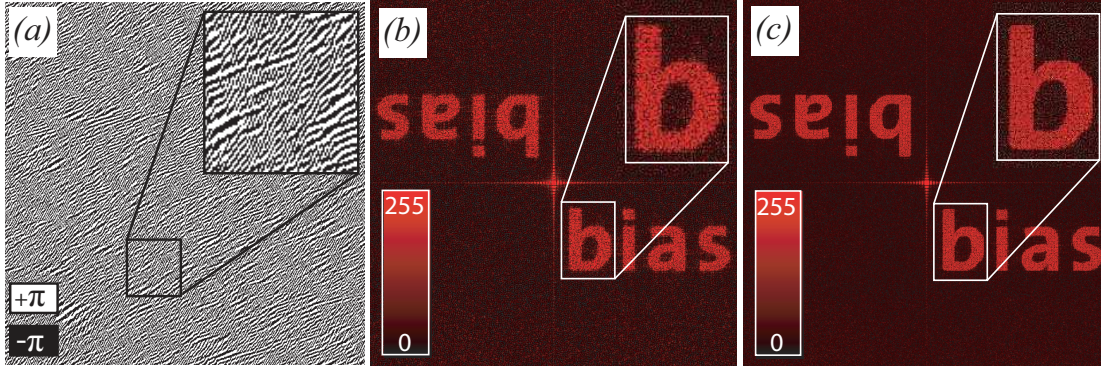
Figure 2.5.: *(a)* A binary coded phase-only CGH designed using an iterative Fourier transform based algorithm. *(b)* Numerically reconstructed far-field projections from a CGH with a size of 256 x 256 pixels and *(c)* of 512 x 512 pixels. Thus, the CGH in *(c)* has a space-bandwidth product of SBWP = $5.2x10^5$ which is four times higher than the one in *(b)* - SBWP = $1.3x10^5$. Therefore, it is apparent that higher SBWP values lead to a reconstruction with a better quality - see Eq. (2.60).

The information capacity of such a discrete CGH, which can be given in terms of the SBWP can be expressed as follows [69]:

$$\text{SBWP} = \frac{L_x L_y}{\Delta x_i \Delta x_j} C, \qquad (2.60)$$

where L_x and L_y denote the size of the CGH in the $x-$ and $y-$directions respectively. For instance, in Fig. 2.5 *(b)* and *(c)* a comparison of numerically computed far-field projections from two phase-only CGHs is presented. The results in *(b)* were acquired from a CGH with an SBWP = $1.3x10^5$, i.e. four times less SBWP as the ones in *(c)* - SBWP = $5.2x10^5$. In the former case a CGH with 256 x 256 pixels and a pixel size of $\Delta x_i = \Delta y_i = 3\mu$m was designed, whereas in the latter case the CGH had 512 x 512 pixels and the same pixel size. The speckled nature of the reconstructions is a result of the clipping of high spatial frequencies of the object wave by the pseudo random phase [15, 81]. It can be seen from these results that the quality of the reconstruction increases with an increase of the SBWP, i.e. with an increase in the degrees of freedom of the optical system.

It is important to note here that in general SBWP can be used to characterize an *optical system* or an *optical signal*. The SBWP of a signal or of a set of signals is

defined by the location and by the range of spatial frequencies within which the signal is nonzero. The SBWP, whether for a system or for a signal, may be either a pure number (degrees of freedom) or a specific area in the $(\boldsymbol{x}, \boldsymbol{q})$ domain, which we will refer to as the Wigner domain [21, 82, 83]. In this work we will use the former definition while considering the synthesis of field distributions means of holographic multiplexing. Thereby, we will investigate how single field distributions can be decoupled and superposed in order to generate a field that possess a higher SBWP than that of the holographic optical system.

3. Current State of the Art in Volume Holographic Optical Elements

As priorly mentioned, a significant portion of holography is devoted to the consideration of numerically computed holographic optical elements, which are used to manipulate wave fields by means of diffraction. This is mainly due to the fact that numerically generated holograms offer important advantages over the optical holograms discussed in the previous section. This type of holograms can for instance be used to encode mathematical functions or mathematically defined wave field distributions. From a historical point of view, digital holograms are commonly categorized as *thin* or *thick*, depending on the relation between the finest cell size they contain and the thickness of the holographic medium. Here, we will mainly discuss holograms in the latter category, as opposed to the thin holographic elements which can be modeled using the scalar diffraction theory presented in the previous chapter.

In this chapter the mathematical framework of three dimensional scattering which is the basis for understanding volume holographic optical elements and their multiplexing capabilities is developed. We begin with an explicit definition of the problem at hand and then we will consider the general case (see Sect. 3.2.), whereby we assume that a scalar field $U_i(\boldsymbol{r})$ is scattered by a weakly scattering but continuously inhomogeneous dielectric medium that is located in a bounded domain $\mathcal{D}_B$. We will show that the scalar approach and the mathematical treatise presented in Sect. 2.3. can be extended to the 3D case if the interaction process between the field and the holographic medium is introduced. In other words, we will show that if this interaction is modeled with an inhomogeneous wave equation, then the resulting field $U(\boldsymbol{s})$ which is captured across the plane $\{\boldsymbol{s}\}$ outside $\mathcal{D}_B$ can be predicted using the scalar theory of scattering. For this purpose the integral equation for potential scattering is derived in Sect. 3.2.2. and a weak scattering approximation is introduced in Sect. 3.2.3. in order to come up with an approximate technique for solving this equation. In section 3.4., we apply this technique to derive the forward and inverse scattering problems for thick volume holographic gratings and CGVHs.

3.1. Problem Definition

The principle problem of designing a HOE can be stated as follows: given a known incident wave field design a holographic optical element that modulates it in order to

obtain a desired target wave field distribution across a given distant plane. Thus we are faced with the problem of finding a hologram that transforms a specific reference wave into a desired *signal* wave field. In other words, we seek to solve an inverse problem for the forward problem of conventional DH described in Sect. 2.3.2., but for the general case of a volume HOE. It follows directly from this that the basic concepts of DH that were presented in the previous chapter are adopted while designing CGVHs. Thereby, the CGVH is defined as a holographic optical element which is usually characterized by the physical state of matter within a given dielectric medium. However, due to various physical limitations inherent to this problem a closed form solution for this problem does not exist in most cases. In the following these limitations will be discussed in details and a rigorous procedure with which an optimal solution to this problem can be acquired for a given set of constraints will be derived.

3.2. Scalar Scattering Theory and its Application in Holography

3.2.1. Inhomogeneous Wave Equation

This section explores the principles behind *scalar scattering theory* and its application in the description of light propagation through a weakly scattering but continuously inhomogeneous dielectric material. In the following analysis we assume that the scattering process is time independent and that the effects of polarization can be ignored. Moreover, we assume that the response of the medium to the incident wave is linear and can be described on a macroscopic scale in terms of the material's refractive index. Under these conditions the propagation of waves in an inhomogeneous medium is described in general by the scalar wave equation [74, 84]

$$(\nabla^2 + k^2(\boldsymbol{r}, \omega))U(\boldsymbol{r}, \omega) = 0. \tag{3.1}$$

It is however important to note that in this case, as opposed to the previously discussed *scalar diffraction theory*, $k(\boldsymbol{r}, \omega)$ is a frequency dependent scalar function representing the refractive index of the medium, i.e.

$$k(\boldsymbol{r}, \omega) = k_o n(\boldsymbol{r}, \omega), \tag{3.2}$$

where $n(\boldsymbol{r}, \omega)$ represents the modulated refractive index of the material (cf. definition in Eq. (2.31)) and $k_o = 2\pi/\lambda = \omega/c$ is the wave number of the incident field. It is evident from Eq. (3.2) that for a homogeneous medium of refractive index n_o, with $k(\boldsymbol{r}, \omega) = k_o$, Eq. (3.1) is the Helmholtz equation (see Eq. (2.42)) as priorly introduced. Substituting (3.2) into (3.1) and rearranging the terms, Eq. (3.1) can be re-written in the form

$$(\nabla^2 + k_o^2)U(\boldsymbol{r}, \omega) = -4\pi S(\boldsymbol{r}, \omega)U(\boldsymbol{r}, \omega), \tag{3.3}$$

with

$$S(\boldsymbol{r}, \omega) = \frac{1}{4\pi}k_o^2 \left[n^2(\boldsymbol{r}, \omega) - n_o^2\right]. \tag{3.4}$$

Equation (3.3) is an inhomogeneous wave equation which was introduced in Eq. (2.37). In this case, $S(\boldsymbol{r}, \omega)$ is the extra term that results from the space dependent dielectric properties and is usually referred to as the *scattering potential* [74, pp. 695]. Considering the geometry depicted in Fig. 3.1 and assuming that for the monochromatic case $S(\boldsymbol{r}, \omega)$ now defines the refractive index distribution within a scattering volume V, which is confined within the domain $\mathcal{D}_B$, the total field $U(\boldsymbol{r}, \omega)$ within this volume can be represented as a sum of two fields, i.e.

$$U(\boldsymbol{r}, \omega) = U_o(\boldsymbol{r}, \omega) + U_s(\boldsymbol{r}, \omega), \tag{3.5}$$

where $U_o(\boldsymbol{r}, \omega)$ is the non-scattered part of the incident field and $U_s(\boldsymbol{r}, \omega)$ the scattered field. The field $U_s(\boldsymbol{r}, \omega)$ is thus solely attributed to the presence of scattering inhomogeneities in the volume. In this work we assume that these inhomogeneities correspond to refractive index distribution given by

$$n(\boldsymbol{r}, \omega) = n_o + \delta_n n_1(\boldsymbol{r}, \omega), \tag{3.6}$$

where n_o is the refractive index of the dielectric material, δ_n represents a slight change in n_o and $n_1(\boldsymbol{r}, \omega)$ is a function of position that accounts for the fluctuations in refractive index. Here, we assume that the refractive index $n(\boldsymbol{r}, \omega)$ of the medium is a real random function of position [56, 74]. By substituting Eq. (3.5) into (3.3), the inhomogeneous wave equation can be expressed as

$$(\nabla^2 + k_o^2)U_o(\boldsymbol{r}, \omega) + (\nabla^2 + k_o^2)U_s(\boldsymbol{r}, \omega) = -4\pi S(\boldsymbol{r}, \omega)U(\boldsymbol{r}, \omega). \tag{3.7}$$

By now taking into account that $U_o(\boldsymbol{r}, \omega)$ is a solution of the homogeneous equation (2.42), i.e. $(\nabla^2 + k_o^2)U_o(\boldsymbol{r}, \omega) = 0$, the first term on the *lhs* drops out and we arrive at the following wave equation for the scattered component:

$$(\nabla^2 + k_o^2)U_s(\boldsymbol{r}, \omega) = -4\pi S(\boldsymbol{r}, \omega)U(\boldsymbol{r}, \omega). \tag{3.8}$$

3.2.2. Integral Equation of Potential Scattering

Since a direct solution for the scalar wave equation in (3.8) does not exist, we follow the scheme introduced in section 2.3. and derive an integral equation of potential scattering. Let us assume that a volume V, that is bounded in the domain $\mathcal{D}_B$, comprises of randomly distributed scatterers which represent points of inhomogeneity described by $S(\boldsymbol{r}, \omega)$ - see Fig. 3.1. The total field due to these scatterers can be represented as a summation of scaled and shifted versions of the impulse response $H(\boldsymbol{r} - \boldsymbol{r}', \omega)$ [85]

$$U_s(\boldsymbol{r}, \omega) = \int_V S(\boldsymbol{r}', \omega)U(\boldsymbol{r}', \omega)H(\boldsymbol{r} - \boldsymbol{r}', \omega)\mathrm{d}^3\boldsymbol{r}'. \tag{3.9}$$

Here, $H(\boldsymbol{r} - \boldsymbol{r}', \omega)$ has the general form of [74, pp. 698]

$$H(\boldsymbol{r} - \boldsymbol{r}', \omega) = \frac{\exp\left(\mathrm{i}k_o \left|\boldsymbol{r} - \boldsymbol{r}'\right|\right)}{\left|\boldsymbol{r} - \boldsymbol{r}'\right|}. \tag{3.10}$$

Let us now consider the case where the incident wave is a monochromatic plane wave of unit amplitude and frequency ω, propagating in the direction specified by a real unit vector $\boldsymbol{\theta}_o$. It follows from Eq. (3.5), with (2.44) and (3.9) that

$$U(\boldsymbol{r}, \omega) = \exp{(\mathrm{i}k_o\boldsymbol{\theta}_o \cdot \boldsymbol{r})} + \int_V S(\boldsymbol{r}', \omega)U(\boldsymbol{r}', \omega)H(\boldsymbol{r} - \boldsymbol{r}', \omega)\mathrm{d}^3\boldsymbol{r}'. \qquad (3.11)$$

This equation presents an analytical solution for the forward scattering problem. It is commonly referred to as the *integral equation of potential scattering* or the *Lippmann-Schwinger equation*. It defines a nonlinear mapping between the scattering potential and the scattered field and is entirely equivalent to Eq. (3.3). However, since in Eq. (3.9) the scattered field is represented in terms of the total field, i.e. $U(\boldsymbol{r}) = U_o(\boldsymbol{r}) + U_s(\boldsymbol{r})$ this equation still needs to be solved for the scattered field. We can therefore conclude that, given the total field $U(\boldsymbol{r}, \omega)$ inversion of Eq. (3.11) to attain the scattering potential is a nonlinear problem which is difficult to solve both from a mathematical as well as from a computational point of view. It is however possible to introduce some approximations under certain circumstances, which will allow linearization of this problem as it will be shown in the next section.
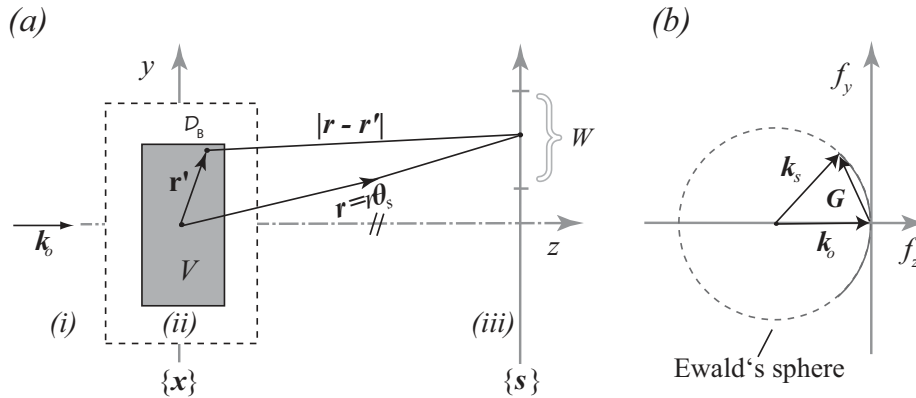
Figure 3.1.: *(a)* Schematic of the geometry considered for a general scattering problem. The gray area corresponds to the volume V of the volume hologram, which is defined by the scattering potential $S(\boldsymbol{r}, \omega)$ while the intermediate region corresponds to the domain $\mathcal{D}_B$. A wave field (wave vector, $\boldsymbol{k}_o = k\boldsymbol{\theta}_o$) incident upon this volume will be scattered such that a predefined field is projected into the signal window W across the plane $\{\boldsymbol{s}\}$ in the far-field domain of the hologram. *(b)* Frequency space representation of the scattering problem where values of the scattered field are seen to lie on a portion (solid line) of the Ewald's sphere (broken line) - after Kamau *et. al.* [17].

3.2.3. Weak Scattering Approximation of the Inhomogeneous Wave Equation

Suppose the scattering potential is localized about the point $\boldsymbol{r}' = 0$ and that it is essentially zero outside V. Furthermore, in reference to Fig. 3.1, we assume we want to determine the scattered field across a plane located *far away* from $\mathcal{D}_B$. Then it is evident that $\boldsymbol{r} \gg \boldsymbol{r}'$ for all points that contribute to the integral in Eq. (3.11), so that

$$|\boldsymbol{r} - \boldsymbol{r}'| \cong r - \boldsymbol{\theta}_s \cdot \boldsymbol{r}', \tag{3.12}$$

where $\boldsymbol{r}'$ is the position vector of the point within the scattering medium, $\boldsymbol{\theta}_s$ is a unit vector in the direction of the scattered field and $\boldsymbol{r} = r\boldsymbol{\theta_s}$ is the position vector of the point on the signal plane W (cf. Fig. 3.1). Thus we can make the approximation [86]

$$\frac{\exp\left(\mathrm{i}k_o\left|\boldsymbol{r} - \boldsymbol{r}'\right|\right)}{\left|\boldsymbol{r} - \boldsymbol{r}'\right|} \cong \frac{\exp(\mathrm{i}k_o r)}{r} \exp\left(-\mathrm{i}k_o\boldsymbol{\theta_s} \cdot \boldsymbol{r}'\right). \tag{3.13}$$

With these assumptions we can then invoke the *weak* scattering approximation to arrive at the following expression for the total field [74, 84]

$$
\begin{aligned}
U(r\boldsymbol{\theta}_s, \omega) &\cong \exp\left(\mathrm{i}k_o(\boldsymbol{\theta}_o \cdot \boldsymbol{r})\right) + U_B(r\boldsymbol{\theta}_s, \omega) \\
&\cong \exp\left(\mathrm{i}k_o(\boldsymbol{\theta}_o \cdot \boldsymbol{r})\right) + \frac{\exp(\mathrm{i}k_o r)}{r} \int_V S(\boldsymbol{r}', \omega)\mathrm{e}^{-\mathrm{i}k_o(\boldsymbol{\theta}_s - \boldsymbol{\theta}_o)\cdot\boldsymbol{r}'}\mathrm{d}^3\boldsymbol{r}'.
\end{aligned}
\tag{3.14}
$$

Equation (3.14) represents an integral form of the inhomogeneous wave equation within the validity of the so called first *Born* approximation, which is essentially a weak potential approximation. Hereby, U_B is thus the scattered field for the case of the first Born approximation. The integral term on the *rhs* of (3.14) is commonly referred to as the scattering amplitude. It clearly represents the Fourier transform of the scattering potential, i.e.

$$\tilde{S}(\boldsymbol{K}, \omega) = \int_V S(\boldsymbol{r}', \omega)\mathrm{e}^{-\mathrm{i}\boldsymbol{K}\cdot\boldsymbol{r}'}\mathrm{d}^3\boldsymbol{r}'. \tag{3.15}$$

From Eq. (3.15) it is clear to see that for a given incident field, the scattered plane wave in the far-field of CGVH in the direction specified by $\boldsymbol{q}_s$ depends entirely on only one Fourier component of the scattering potential, since the spatial frequency vector $\boldsymbol{K}$ is given by [74, 86]

$$\boldsymbol{K} = k_o(\boldsymbol{\theta}_s - \boldsymbol{\theta}_o). \tag{3.16}$$

3.3. Optically Recorded Volume Holograms

The term volume holograms was initially used to refer to thick hologram gratings. Essentially, these are holographic optical elements which are recorded in the bulk of a given medium by means of two or multiple beam interference. These type of holograms were studied intensively in the 1960s [5], and are still of particular interest for

applications in high capacity data storage [6] as well as display and communication technology [87]. In this section, the concepts behind volume holograms will be presented using the fundamentals of scalar scattering theory introduced in the previous section. This will pave way to the discussion on the current state of the art in the field of CGVHs.

It is important to note here that the scalar approach discussed here only presents a good approximation for weakly modulated loss-less holographic gratings. For the weakly modulated volume phase holograms (VPH) that we will consider here, we assume that typical values are on the order of $\delta_n \approx 10^{-3}$. With this assumption, effects resulting for example from polarization of the light or absorption within the hologram can be neglected [52]. A rigorous analysis of volume holograms involves applying the rigorous coupled wave theory (RCWT), which can be derived from the Maxwell's equations and is described more comprehensively in Sect. B.2.

3.3.1. Volume Phase Holograms

The most basic form of a volume hologram is recorded using plane waves for both the object and reference beams. The interaction of the two optical fields results in a stationary interference pattern at the media, consisting of bright and dark fringes. The fringes are recorded throughout the media volume via modulation of the dielectric constant of the material. These technique can however be used to record even more complex types of holograms, whereby the plane object wave is replaced by an arbitrary wave that can be generated for instance by means of a spatial light modulator [88]. These type of holograms are commonly referred to as volume phase holograms (VPH).

Let us consider a hologram which is recorded by superimposing two plane waves $U_r(\boldsymbol{r}) = U_1 \mathrm{e}^{\mathrm{i}\boldsymbol{k_r} \cdot \boldsymbol{r}}$ and $U_o(\boldsymbol{r}) = U_2 \mathrm{e}^{\mathrm{i}\boldsymbol{k_o} \cdot \boldsymbol{r}}$ in a linear dielectric medium, thereby leading to a refractive index modulation. This optically induced refractive index modulation $\delta_n(\boldsymbol{r})$ is locally proportional to the intensity distribution, which is given by Eq. (2.51). In other words

$$\delta_n(\boldsymbol{r}) \propto |U_1|^2 + |U_2|^2 + 2\,|U_1|\,|U_2| \cos\left[(\boldsymbol{k_r} - \boldsymbol{k_o}) \cdot \boldsymbol{r} - \Delta\varphi\right], \qquad (3.17)$$

where $\Delta\varphi$ is the phase difference between the phasors U_1 and U_2 [2]. For infinite plane waves, we can define a grating vector $\boldsymbol{K}_G$, which in analogy to Eq. (3.16) is given by the difference of the two wave vectors,

$$\boldsymbol{K}_G = \boldsymbol{k_r} - \boldsymbol{k_o}. \qquad (3.18)$$

The magnitude of the grating vector is given by $|\boldsymbol{K}_G| = 2\pi/\Lambda$, where Λ is the grating period. A beam transversing such an elementary grating is only diffracted when the Bragg condition, as it is defined by Eq. (3.18), is met. The magnitude of the illuminating and diffracted wave vectors inside the medium of a refractive index n are $|\boldsymbol{k_o}| = |\boldsymbol{k_r}| = 2\pi n/\lambda$ and have angles of θ_o and θ_r respectively as shown in Fig. 3.2. Due to this limitation on the range of wavelengths (or angles) over which diffraction occurs, it is ideally possible to record multiplexed holograms inside the same volume

that work independently and without interfering with each other [2, pp. 332]. It is also possible to obtain a theoretical 100% diffraction efficiency in this case. However, diffraction of light traveling through the hologram will also depend on the magnitude of the refractive index modulation δ_n as well as the thickness of the volume grating d. The multiplexing properties of volume holograms is thus dependent on the *thickness* of the recording material.

As per definition, a *thin* hologram is one that essentially modulates light across a single plane as it was discussed in the case of CGHs. On the other hand, the interaction of light in a *thick* hologram takes place at different positions within the volume. Within the validity of the scalar theory introduced above, the resulting field can be assumed to be a superposition of the light scattered from the individual positions within the hologram. In order to characterize a VPH as either thick or thin, and thereby take into consideration the influence of the other aforementioned parameters, the Q Parameter

$$Q = \frac{2\pi\lambda d}{n\Lambda^2} \tag{3.19}$$

was introduced [89]. Here, λ is the vacuum wavelength of the light used to reconstruct it and Λ is the grating period. If $Q > 1$ and the induced index change is large enough, then the VPH is considered thick and vice versa.

Let us now assume that a given hologram of thickness $d = L_z$ and infinite extent has a plane parallel grating with fringes that are normal to the grating surface - see Fig. 3.2 (a). Then the Bragg condition of such a VPH is given by [90]

$$m\lambda = 2n_1 \sin(\theta_B)\Lambda, \tag{3.20}$$

where θ_B is the Bragg angle in the grating medium, m is the order of diffraction and n_1 is the modulated part of the refractive index $n(y, z)$ within the hologram itself as given by Eq. (3.17) and is approximately represented by

$$
\begin{aligned}
n(y, z) &= n_o + n_1 \\
&= n_o + \delta_n \cos\left[\frac{2\pi y}{\Lambda}\right] \operatorname{rect}\left[\frac{z}{L_z}\right].
\end{aligned} \tag{3.21}
$$

Thus for plane parallel gratings Bragg condition is met when m is an integer and the wavelength and Λ is such that the angles of incidence and diffraction are equal and opposite, with respect to the surface normal [90]. This Bragg selectivity property essentially facilitates fabrication of multiplexed VPHs. In Fig. 3.2 (b) this multiplexing capabilities of volume holograms is illustrated. Hereby only light incident at the Bragg angle with respect to the grating with slanted fringes is scattered efficiently. It is this selective aspect which allows these gratings to be tuned for different angles or wavelengths by for instance changing the tilting angle with respect to the incident beam of light [90].
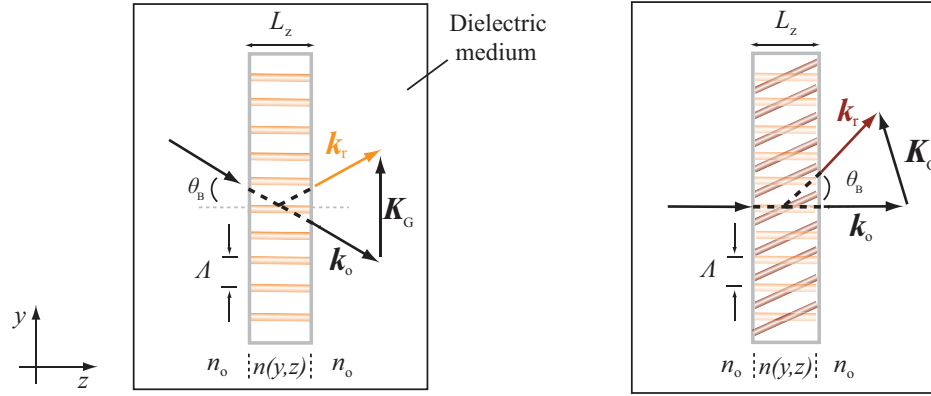
Figure 3.2.: *(a)* Illustration of the illumination of an elementary transmission volume holographic grating at a Bragg angle θ_B. Since the incident light fulfills the Bragg condition, the angles of incidence and diffraction are equal and opposite. *(b)* Illustration of the multiplexing capabilities of volume holograms, whereby only light incident at the Bragg angle with respect to the grating with slanted fringes is scattered efficiently. It is this selective aspect which allows these gratings to be tuned for different orders of diffraction and/or wavelengths by changing the tilting angle α_S with respect to the incident beam of light.

3.3.2. Bragg Selectivity and Multiplexing Properties of Volume Holograms

In practice, all holograms have a limited size, which is determined by the thickness of the medium L_z and their lateral extension (L_x, L_y). Additionally, given the fact that all wave fronts can be decomposed into a sum of plane waves as it was discussed in Sect. 2.3.1., understanding the nature of periodic VPHs is very useful. In this section an overview on this type of holograms is presented.

Let us assume we have a volume holographic grating with a Q-factor $Q > 1$. If such a VPH is illuminated at angles significantly outside of the Bragg condition light may pass through it without being diffracted. However, near the Bragg angle, there is a range of angles for which light will still be efficiently diffracted [90]. To illustrate this effect and how it is related to the size of the VPH, we will consider a holographic grating with a cosinusoidal refractive index modulation - cf. Eqs. (3.17) and (3.21). Suppose that the scattering potential of this hologram can approximately be written in its general form as follows

$$S(\boldsymbol{r}) = [1 + m \cos(\boldsymbol{K}_G \cdot \boldsymbol{r} - \phi)] \operatorname{rect}\left[\frac{x}{L_x}, \frac{y}{L_y}, \frac{z}{L_z}\right]. \tag{3.22}$$

With the help of Eq. (3.15) and by applying the convolution theorem we can easily

compute the grating vector spectrum by means of a 3D Fourier transform to arrive at

$$\tilde{S}(\boldsymbol{K}) = AL_z \left[\delta(\boldsymbol{K}) + \frac{1}{2}\delta(\boldsymbol{K} - \boldsymbol{K}_G) + \frac{1}{2}\delta(\boldsymbol{K} + \boldsymbol{K}_G) \right]$$
$$\otimes \operatorname{sinc}\left[\frac{L_x k_x}{2\pi}, \frac{L_y k_y}{2\pi}, \frac{L_z k_z}{2\pi} \right], \tag{3.23}$$

where $A = L_x \cdot L_y$ is the area of the aperture bounding the hologram. From this it is clear that the multiplicative *rect* function on the scattering potential in (3.22) leads to a convolution of all frequency space components by a *sinc* function. The effect of this convolution is a blurring of the grating vector tip into a continuum of vectors surrounding the ideal position [2, 31].

After further rigorous analysis of HOEs using for instance RCWT (see Sect. B.2.), it can be shown that for a loss-less transmission VPH the diffraction efficiency can be defined as follows

$$\eta = \operatorname{sinc}^2\left(\sqrt{\chi_1^2 + \chi_2^2} \right), \tag{3.24}$$

whereby the parameters

$$\chi_1 = \frac{\pi n_1 L_z}{\lambda \cos(\theta_B)}, \tag{3.25}$$

and

$$\chi_2 = \Delta\theta \frac{\pi L_z}{\Lambda} \tag{3.26}$$

are related to the angular deviation $\Delta\theta$ from the Bragg angle θ_B and the thickness of the hologram. Diffraction efficiency of this VPH is thus maximum at the Bragg incidence and decays as a sinc^2 function as a result of the angular Bragg mismatch [52, 91] as it is shown in Fig. 3.3 *(a)*. The angular Bragg selectivity of a volume hologram can be characterized in terms of the full width at half maximum (FWHM) of this *sinc* envelope. In Fig. 3.3 *(b)* angular Bragg selectivity, as a function of the holograms thickness, is depicted for different holograms. Here, the range of Bragg mismatch $\Delta\theta$(FWHM) is shown for holograms with different grating periods Λ. Further practical implications of this blurring effect and their impact on the Bragg selectivity of CGVHs will be discussed in the following sections.

3.4. Computer Generated Volume Holograms (CGVH)

Computer generated volume holograms are volumetric holographic non-periodic optical elements whose complex transfer functions can be controlled and optimized in the design process [47, 56]. In analogy to their 2D counterparts (cf. Sect. 2.3.2.), CGVHs are generated numerically by means of iterative optimization algorithms. Mathematically, CGVHs are modeled as a randomly scattering inhomogeneous medium, that is characterized by a refractive index distribution. In the following, the problem of
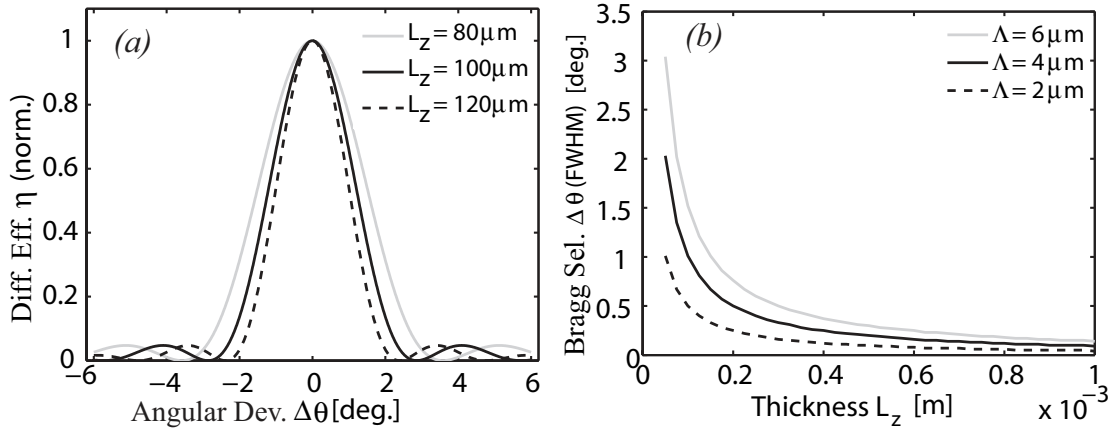
Figure 3.3.: *(a)* Plots of the angular bandwidth envelope for volume phase holograms (VPH) with a thickness of $L_z = 80\ \mu$m, $100\ \mu$m, $120\ \mu$m, in terms of the diffraction efficiency η and the deviation from the Bragg angle $\Delta\theta$. The dependency of the blurring of the spectrum on the size of the VPH can clearly be seen in this plots - see Eq. (3.24). *(b)* Illustration of angular Bragg selectivity in terms of the FWHM as a function of the holograms thickness. Here, the range of Bragg selectivity $\Delta\theta$(FWHM) is depicted for holograms with different grating periods Λ.

computing the scattering potential of such a hologram within the validity of the first order Born approximation is presented. In chapter 5 an extension of this approach in terms of a model based on higher order approximation of Eq. (3.11) will be presented.

3.4.1. Definition of the Inverse Problem: Modeling CGVHs within the validity of the Born Approximation

The problem of designing a CGVH is an inverse problem and can be stated as follows: *the set of wave field distributions that is to be generated in a certain predefined domain is the known effect for which the scattering potential inside the CGVH is the sought cause.* In the sense of Hadamard, there are three important conditions that must be fulfilled for this kind of a problem to be *well-posed* [92]. These are the existence, uniqueness and the continuous dependence of the solution on the target far-field distributions. However, for most practical applications fulfillment of the first two conditions cannot be guaranteed. This is mainly due to the fact that the problem is formulated ideally for an infinitely large CGVH which is represented in terms of a continuous scattering potential. For computational purpose the scattering potential $S(\boldsymbol{r'}, \omega)$ is then discretized, whereby a discretization error appears. Furthermore, only a set of far field projections are specified for limited values $\boldsymbol{q}_s$ and $\boldsymbol{q}_o$. In general, for a fixed value of k, a complete determination of $S(\boldsymbol{r'}, \omega)$ is only possible if U_s is known for various values $\boldsymbol{q}_s$ and $\boldsymbol{q}_o$. Thus, this problem is in essence an ill-posed inverse problem involving the mapping of the 3D field distribution scattered in the volume hologram

onto one or a set of transverse 2D planes [58]. The resolution of this inverse problem requires very good knowledge of the underlying forward problem, i.e. an explicit description of how light is scattered inside the volume of the hologram is needed. In the following, a model that allows for the numerical computation of the CGVH is thus derived from the scalar theory of scattering, which was presented in Sect. 3.2.

To derive this model, we begin by considering the general setup that is depicted in Fig. 3.4. Hereby, a plane wave field (wave vector $\boldsymbol{k}_o$) which is incident on the CGVH is scattered in the bulk of the hologram thereby resulting in a total field $U(\boldsymbol{r}, \omega)$ - see Eq. (3.5). One portion of the total field is in turn transformed into a projection $U_s(\boldsymbol{r}, \omega)$, whereby this transformation can be formulated in terms of forward mapping operator:

$$\mathcal{P}_f : U(\boldsymbol{r}, \omega) \longrightarrow U_s(\boldsymbol{r}, \omega) \quad \forall (\boldsymbol{K}, \omega) \in W. \tag{3.27}$$

From equations (3.15) and (3.16), we can see that $\mathcal{P}_f$ defines a 3D mapping of the total field $U(\boldsymbol{r}, \omega) \in \mathbb{C}^3$ by the potential $S(\boldsymbol{r}, \omega) \in \mathbb{R}^3$ in Eq. (3.4), on to the scattered field $U_s(\boldsymbol{r}, \omega) \in \mathbb{C}^2$. This physical implication becomes apparent when one considers the scattering process within the bulk of the hologram in frequency space as it is defined by Eqs. (3.15) and (3.16). Here, the values of the scattered field are seen to lie on a portion of the Ewald's sphere. We therefore conclude that Eq. (3.16) is a restatement of the Bragg condition for holograms designed using this approach. Thus, Eq. (3.14) presents the *direct problem* of designing CGVHs.
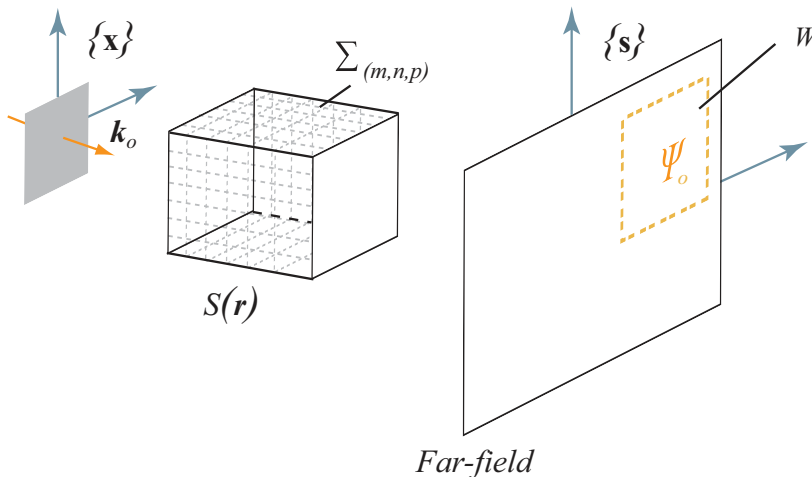
Figure 3.4.: Schematic of the basic principle behind wave field synthesis approach using a discrete CGVH which is defined in terms of its scattering potential $S(\boldsymbol{r})$. Each voxel $\Sigma_{n,m,p}$, represents the local modulation of the refractive index. In the CGVH a single or several angular projections of predefined far-field distributions Ψ_i are encoded. A given plane reference wave that fulfills the Bragg condition will encode the corresponding projection.

Unfortunately, the existence of the corresponding inverse problem cannot be guaranteed as previously discussed. However, given a set of constraints, numerical optimization based methods can be applied to compute an optimal solution. In the current

design approach [56, 57], using Eqs. (3.14) and (3.16) optimization theory is applied to compute an optimal solution iteratively. Thereby, assuming that for every target far-field projection Ψ_i there exists an optimal binary refractive index contrast

$$\tilde{n} = \delta_n n_1(\boldsymbol{r}) \tag{3.28}$$

such that $\hat{n} = \operatorname{argmin}_{\hat{n}}(\boldsymbol{L})$, i.e. it minimizes the objective function

$$\boldsymbol{L}(\tilde{n}_j) = \|U_t - U(\tilde{n}_j)\|^2, \tag{3.29}$$

where $\tilde{n}_j$ is the approximated refractive index contrast at the $j-$th iteration and U_t is the target field. It is however crucial that the refractive index change must be constrained to values on the order of $\delta_n \approx 10^{-3}$, i.e. that lie within the validity of the Born approximation as it will be shown in Sect. 3.5.

3.4.2. Iterative Design Algorithm Based on The Born Approximation

The algorithm described in this section is thus based on Eq. (3.14) and involves optimizing a multivariable system as defined by the functional in Eq. (3.29). It is a bi-directional algorithm which is similar to the iterative Fourier transform based Gerchberg-Saxton algorithm [79]. The design algorithm can be summarized for the case of angular multiplexing in five steps as follows [56, 57]:

1. In the initial step, a discrete scattering potential $S_j(\boldsymbol{r}, \omega)$ for a desired CGVH composed of M x N x P number of voxels is initialized by generating a random refractive index contrast $n(\boldsymbol{r})$ as an initial guess.

2. To attain the resulting scattered fields, the forward mapping $\mathcal{P}_f$ is computed for each far-field projection. Thereby a 3D forward FFT of the scattering potential is computed and the far-field projections are extracted from the corresponding portion of the Ewald's sphere for each illumination direction. From Eqs. (3.14) and (3.16) the scattered field for a given incident field can be expressed in frequency space as

$$\tilde{U}_j(\boldsymbol{K}) = \frac{e^{ikr}}{r} \tilde{S}(\boldsymbol{K}). \tag{3.30}$$

3. Each of these single fields is then modified to better approximate the target intensity $I_t(\boldsymbol{K}, \omega)$ across a given plane in the far-field of the CGVH by imposing the following amplitude constraint:

$$\tilde{U}_j(\boldsymbol{K}, \omega) = \begin{cases} c_k \sqrt{I_t(\boldsymbol{K}, \omega)} \cdot e^{[i\phi_j(\boldsymbol{K}, \omega)]} & \forall (\boldsymbol{K}, \omega) \in W \\ \tilde{U}_j(\boldsymbol{K}, \omega) & \text{otherwise.} \end{cases} \tag{3.31}$$

Here, $\phi_j(\boldsymbol{K}, \omega) = \arg\{\tilde{U}_j(\boldsymbol{K})\}$ is the unmodified phase. We hereby assume that $I_t(\boldsymbol{K}, \omega)$ is only given within the limited signal window W (cf. Fig. 3.4). Furthermore, a linear interpolation is employed to map $I_t(\boldsymbol{K}, \omega)$, which is defined across

a planar detector surface, on to the circular manifold of the Ewald's sphere. The weighting factor c_k is introduced here to ensure the convergence of the algorithm and was determined here heuristically by means of a parameter scan.

4. The modified and unmodified sections of the Ewald's sphere are recombined to obtain $\tilde{S}_j(\boldsymbol{K}, \boldsymbol{\omega})$ and an inverse 3D FFT is used to compute a new scattering potential, i.e. $\acute{S}_j(\boldsymbol{r}, \omega) = \mathcal{F}_{3D}^{-1}\left\{\tilde{S}_j(\boldsymbol{K}, \boldsymbol{\omega})\right\}$.

5. To obtain an approximated binary refractive index contrast $\tilde{n}_j$, a fabrication constraint is imposed on this new scattering potential as follows

$$S_{j+1}(\boldsymbol{r}, \omega) = \begin{cases} \frac{1}{4\pi}k^2\left[n_j^2(\boldsymbol{r}, \omega) - n_o^2\right] & \forall \acute{S}_j(\boldsymbol{r}, \omega) \geq \frac{1}{8\pi}k^2\left[n_j^2(\boldsymbol{r}, \omega) - n_o^2\right] \\ 0 & \text{otherwise.} \end{cases} \tag{3.32}$$

Finally, $S_{j+1}(\boldsymbol{r}, \omega)$ is set as the new scattering potential and steps 2.-5. are repeated until the algorithm converges to an optimum solution $\hat{n}$. To monitor the convergence of the algorithm, both diffraction efficiency and the average value of δ_n are computed at each iteration.

3.5. Limitations in the Current State of the Art

The principle limitation of planar 2D holographic optical elements, in terms of their capability of wave field synthesis, is the fact that they can only modulate an impinging wave across a single transverse plane. This has led to an ever increasing demand of developing 3D optical elements. For instance, stratified DOEs in a cascaded setup have been proposed [49] and it has been shown that by adding more degrees of freedom they expand the system's solution space thus facilitating both angular and frequency multiplexing [50, 51].

Another example is presented by volume phase holograms [52]. As it was discussed in Sect. 3.3, these are optically recorded periodic diffractive optical elements that depict both angular and wavelength selectivity in cases where the Bragg condition is fulfilled, as opposed to their 2D counterparts. Although these two types of volume elements have found numerous applications, their ability to generate arbitrary light distributions within a certain 3D domain is quite limited. This is mainly due to their comparatively low diffraction efficiency, since the efficiency of the device decreases as the square root of the number of holograms recorded in a multiplexed hologram and the thickness of the hologram. This can also be attributed to the fact that for thick holograms, since individual voxels cannot be addressed, the achievable degrees of freedom are limited by the optical recording process [53].

A better solution is presented by the CGVHs that were introduced in Sect. 3.4. In the current design approach several shortcomings in the applied forward model (cf. Sect. 3.2.3.) and its implementation have however been recognized. These shortcomings have the effect of imposing very stringent restrictions on the achievable optical functionality of CGVHs and can be listed as follows:

(i) In the current state of the art the assumption of weak scattering is necessary in order to derive a linear model for the numerical modeling of the scattering process. Hereby the Born approximation is applied [56, 57]. This approximation is derived by considering only linear perturbation of the amplitude of the scattered wave field. In other words, it is obtained by requiring that the first order correction of the scattered field be small as compared to the incident field [93]:

$$|U_B(r\boldsymbol{\theta}_s, \omega)| \ll |U_o(r\boldsymbol{\theta}_o, \omega).| \tag{3.33}$$

Given Eq. (3.14), this results in

$$\left| \frac{\exp(\mathrm{i}k_o r)}{r} \int_V S(\boldsymbol{r'}, \omega) \mathrm{e}^{-\mathrm{i}k_o(\boldsymbol{\theta}_s - \boldsymbol{\theta}_o) \cdot \boldsymbol{r'}} \mathrm{d}^3\boldsymbol{r'} \right| \ll 1. \tag{3.34}$$

Since the scattered field can be expected to increase with increasing distance of propagation, it is clear that the Born approximation can easily break down for large holograms. For holograms with dimensions in the sub-millimeter range, this assumption leads to a constraint that limits the index modulation allowed to very small values within a range on the order of $(\delta_n \approx 10^{-4} \cdots 10^{-3})$, relative to the refractive index of the background material [56, 57]. This in turn limits the optical functionality of the CGVH in terms of angular and frequency selectivity. An approximation that gives a more accurate estimate for larger CGVH sizes without such stringent restrictions has not yet been considered in this context and will be considered in the course of this work.

(ii) The iterative Fourier transform algorithm that has been applied so far tends to stagnate after the first few iterations [56]. This is attributed to the fact that a set of basic constraints in both the frequency and space domains are not fully fulfilled thereby leading to convergence to a local minimum. For instance, in the definition of the coding and quantization operators, which are crucial for the discrete representation and for the fabrication of the CGVH in a dielectric material, various linear interpolation schemes have to be employed - see *step 3* in Sect. 3.4.2. This misrepresentation of values can be shown to lead to deviations from the desired optimal distribution. This in turn implies that diffraction still occurs even for cases where the Bragg condition is not fulfilled. For multiplexed CGVHs, where the fulfillment of the Bragg condition is indispensable, this will result in a poor signal-to-noise ratio (SNR) and to a reduced diffraction efficiency.

(iii) In the current state of the art, only fabrication of CGVHs by means of a linear one photon absorption process has been demonstrated. In such an approach, the photomodification of the substrate, which leads to a localized change in the refractive index can predominantly be attributed to light-induced damage [94]. Thereby, the substrate will undergo a dielectric breakdown upon irradiation by femtosecond laser pulses. This will in turn create a void filled by the gaseous products of the breakdown process. In such a case, the contrast of refractive index is created between the damaged and non-damaged substrate material [95]. An

alternative approach would be to utilize a multiphoton absorption process (MPA) to fabricate CGVHs in a nonlinear optical material such as a photosensitive glass-ceramics [57]. Thereby, a multiphoton absorption process can be used to facilitate a more accurate fabrication of volume holograms, which have smooth internal contours and with even much smaller voxel sizes. This is mainly due to the fact that the absorption profile is narrower than the beam profile. Furthermore, such a nonlinear material allows for the manipulation of the refractive index in a subsequent postbake process [96] and this can be utilized to accurately tune the refractive index change. So far, a laser lithography based fabrication of CGVHs in nonlinear optical materials has not been investigated.

4. Reformulation of the Inverse Scattering Problem and the Hypothesis of this Work

In this thesis a model that allows for a more accurate prediction of the field scattered within the volume of a CGVH is derived. In this model both physical and fabrication constraints that are derived from the wave equation as well as from the consideration of the underlying laser material interaction process are integrated. To accomplish this, the inverse scattering problem has to be reformulated.

4.1. Motivation and Problem Definition

Let us start by considering higher order approximations of the inhomogeneous wave equation. We can do this in the form of the *Rytov approximation*, which consists mainly in expressing the total field in Eq. (3.5) in terms of its complex phase, $\Phi(\boldsymbol{r}, \omega)$, form as follows [74, 97]

$$U(\boldsymbol{r}, \nu) = U_o(\boldsymbol{r}, \omega)\exp\left[\Phi(\boldsymbol{r}, \omega)\right]. \tag{4.1}$$

Now let us consider the power series expansion of the exponential term in Eq. (4.1) so that the total field can be written as

$$U(\boldsymbol{r}, \omega) = U_o(\boldsymbol{r}, \omega)\left[1 + \frac{\Phi(\boldsymbol{r}, \omega)}{1!} + \frac{\Phi(\boldsymbol{r}, \omega)^2}{2!} + \frac{\Phi(\boldsymbol{r}, \omega)^3}{3!} + \cdots\right]. \tag{4.2}$$

In the literature it is customary to consider the first two terms of the series in Eq. (4.2) in order to derive a scattering model based on the Rytov approximation [98–100]. For instance, as it will be shown in Sect. 5.1.2., by considering only the linear term and expressing the complex phase in terms of the Born approximation the total field assumes the additive form of Eq. (3.14)

$$\begin{aligned} U(\boldsymbol{r}, \omega) &= U_o(\boldsymbol{r}, \omega) + U_o(\boldsymbol{r}, \omega)\Phi(\boldsymbol{r}, \omega) \\ &= U_o(\boldsymbol{r}, \omega) + U_B(\boldsymbol{r}, \omega). \end{aligned} \tag{4.3}$$

Therefore, we can conclude that both Born and first order Rytov approximations should produce the same results for a given hologram that fulfills the constraints in Eq. (3.34). However, since the Rytov approximation results from a perturbation expansion of the complex phase of the field rather than of the amplitude, it should have a larger validity in potential scattering than the Born approximation [84]. This fact leads to the following proposition.

4.2. Hypothesis

The current approach for numerically computing the scattering potential of CGVHs considers only the linear perturbation of the amplitude of a scattered wave field, within the validity of the first Born approximation. This leads to a stringent limitation on the hologram in terms of the allowed refractive index modulation. The range of the allowed values are on the order of $\delta_n \approx 10^{-4} \cdots 10^{-3}$. This in turn implies that the design of highly efficient multiplexed CGVHs using this approach is limited and that the size of the holograms is constrained to dimensions on the order of $L \leq 200 \mu m$.

Through a novel approach that is based on the first Rytov approximation, CGVHs with a refractive index modulation within a range of $\delta_n \approx 10^{-4} \cdots 10^{-2}$ can be computed. In this case the size of the feasible holograms depends on the number of terms of the perturbation series that are considered.

In this thesis we posit that such an approach can be applied to design CGVHs, which we define in terms of refractive index modulation of a nonlinear optical dielectric medium. We propose that this approach will facilitate realization of holograms with a higher space-bandwidth product and thus with improved optical functionality. This improvement will be assessed by characterizing their performance in terms of diffraction efficiency, Bragg selectivity and the SNR of the synthesized far-field projections.

5. Advanced Dynamic Wave Field Synthesis Using Electronically Addressed Computer Generated Volume Holograms

In this chapter we will outline an approach which is based on the solution of the inverse scattering problem introduced in chapter 4. The main aim is to come up with a novel approach for optimizing the performance and optical functionality of computer generated volume holograms. Moreover, we will analyze the feasibility of fabricating such holograms in a nonlinear optical material as well as derive the corresponding physical constraints. The motivation behind this goal is to design and optimize a system that facilitates dynamic synthesis of predefined wave fields. Specifically, we focus on a novel hybrid system comprising in a spatial light modulator (SLM) as a dynamic element and a CGVH as a multiplexed static element. Figure 5.1 shows the schematic of the setup that is considered in our design. This configuration makes use of an SLM which allows for the adaptive manipulation of the impinging wave. The SLM is illuminated with a plane reference wave (with wave vector $\boldsymbol{k_o}$); the modulated wave fields (described by the wave vector $\boldsymbol{k_i}$) then propagate through a CGVH thereby decoding individual projections. With this, wave fields with a higher SBWP can for instance be generated through coherent superposition of these projections.

5.1. Advanced Scattering Model

5.1.1. Rytov Approximation

In order to derive an advanced model on the basis of the first Rytov approximation, we start by studying the scattering of the scalar wave of the form of Eq. (4.1). In analogy to Eq. (3.5), we can express the total complex phase as the sum of the incident phase function $\Phi_o(\boldsymbol{r}, \omega)$ and the scattered complex phase $\Phi_s(\boldsymbol{r}, \omega)$

$$\Phi(\boldsymbol{r}, \omega) = \Phi_o(\boldsymbol{r}, \omega) + \Phi_s(\boldsymbol{r}, \omega). \tag{5.1}$$

Furthermore, we consider the total field to be represented as a complex phase as shown in Eq. (5.1). This scalar wave satisfies the wave equation so that after inserting Eqs. (4.1) (with $U_o(\boldsymbol{r}, \omega) = 1$) and (5.1) into the wave equation in Eq. (3.3) we obtain the
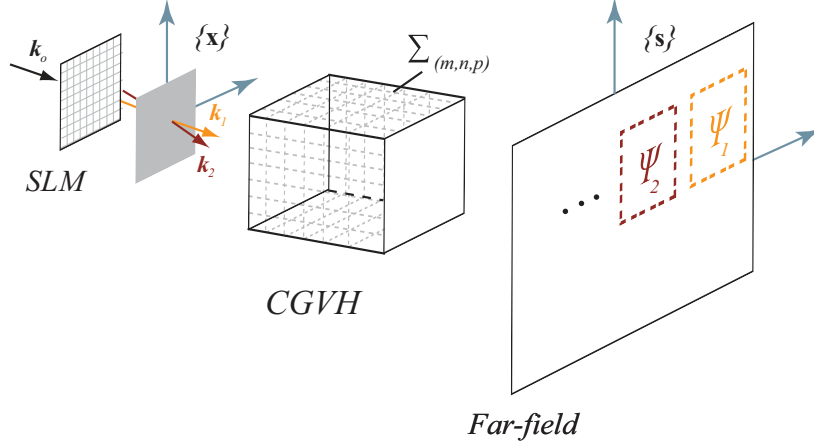
Figure 5.1.: Schematic of the basic principle behind the dynamic wave field synthesis approach, which utilizes the Bragg selectivity property of volume holograms. In the CGVH several angular projections of predefined far-field distributions are encoded. The spatial light modulator (SLM) is used to modulate an impinging plane wave ($\boldsymbol{k}_o$) such that the corresponding reference waves ($\boldsymbol{k}_i$) can be generated across a remote plane $\{\boldsymbol{x}\}$ in the entrance aperture of the CGVH. This allows for a dynamic decoding of individual projections or their superposition.

following equation for $\Phi(\boldsymbol{r}, \omega)$ - cf. Sect. A.3 for the derivation

$$\nabla^2 \Phi(\boldsymbol{r}, \omega) + [\nabla \Phi(\boldsymbol{r}, \omega)]^2 = -4\pi S(\boldsymbol{r}, \omega). \tag{5.2}$$

Hereby, $S(\boldsymbol{r}, \omega)$ is the scattering potential in Eq. (3.4). By expressing the total complex phase Φ as a sum of the incident phase function Φ_o and scattered phase Φ_s as given by Eq. (5.1) and considering that $S(\boldsymbol{r}, \omega)$ is given by Eq. (3.4) into Eq. (5.2) we arrive at the following nonlinear equation for $\Phi_s(\boldsymbol{r}, \omega)$

$$\nabla^2 \Phi_s(\boldsymbol{r}, \omega) + \nabla^2 \Phi_o(\boldsymbol{r}, \omega) + (\Phi_o(\boldsymbol{r}, \omega))^2 + (\Phi_o(\boldsymbol{r}, \omega))^2 + 2\Phi_o(\boldsymbol{r}, \omega) \cdot \Phi_s(\boldsymbol{r}, \omega) = -4\pi S(\boldsymbol{r}, \omega). \tag{5.3}$$

An an approximate solution of Eq. (5.3) can be obtained by means of the Rytov expansion of $\Phi(\boldsymbol{r}, \omega)$ as follows

$$\Phi(\boldsymbol{r}, \omega) = \Phi_o(\boldsymbol{r}, \omega) + \gamma \Phi_1(\boldsymbol{r}, \omega) + \gamma^2 \Phi_2(\boldsymbol{r}, \omega) + \cdots, \tag{5.4}$$

where γ is a perturbation parameter. It is apparent that Φ_1 is linear in $S(\boldsymbol{r}, \omega)$, Φ_2 is quadratic in $S(\boldsymbol{r}, \omega)$ and so on [74]. In this thesis we consider the first order term with the aim of assessing the feasibility of designing multiplexed CGVHs. In this case, the total field can be written as

$$U(\boldsymbol{r}, \omega) = \exp\left[\Phi_o(\boldsymbol{r}, \omega) + \Phi_1(\boldsymbol{r}, \omega)\right]. \tag{5.5}$$

In general however, the Rytov expansion allows for the derivation of a recurrence relation with which any successive terms can be computed once the preceding ones

are known. This recurrence relation for the Rytov series is derived in details in Sect A.4.

5.1.2. First Order Rytov Approximation

In this section we will derive equations which facilitate the design of a CGVH within the validity of the first order Rytov approximation. We begin by noting that within the accuracy of first order perturbation theory we can deduce from Eq. (5.1) that [74]

$$\Phi(\boldsymbol{r},\omega) = \Phi_o(\boldsymbol{r},\omega) + \Phi_1(\boldsymbol{r},\omega), \tag{5.6}$$

where $\Phi_o(\boldsymbol{r},\omega)$ denotes the zero order term of the series expansion. Here, the complex phase of the scattered field $\Phi_1(\boldsymbol{r},\omega)$ can be expressed in terms of the Born approximation as follows as

$$\Phi_1(\boldsymbol{r},\omega) = \frac{U_B(\boldsymbol{r},\omega)}{U_o(\boldsymbol{r},\omega)}. \tag{5.7}$$

Please note, as it was introduced in Sect. 4.1., that by considering only the linear term in Eq. (4.3) and then inserting Eq. (5.7) one arrives at an expression that is similar to the Born approximation. Furthermore, given Eqs. (5.6) and (5.7) we can derive a integral form of the differential equation in Eq. (A.16). As a result, in a similar manner to the case of the Born approximation (cf. Eq. (3.14)), the total field within validity of the Rytov approximation is then given by [17]:

$$\Phi(r\boldsymbol{q}_s,\omega) \cong \Phi_o(\boldsymbol{r},\omega) + \Phi_R(\boldsymbol{r},\omega)$$
$$\cong \Phi_o(\boldsymbol{r},\omega) + \frac{1}{U_o(\boldsymbol{r},\omega)} \frac{\mathrm{e}^{\mathrm{i}kr}}{r} \int_V S(\boldsymbol{r}',\omega)\mathrm{e}^{-\mathrm{i}k(\boldsymbol{q}_s-\boldsymbol{q}_o)\cdot\boldsymbol{r}'}\mathrm{d}^3\boldsymbol{r}', \tag{5.8}$$

where $\Phi_R(\boldsymbol{r},\omega)$ is the scattered complex phase withing the first Rytov approximation. In deriving Eq. (5.8), given Eqs. (A.16) and (5.7), we however have to make an assumption that

$$(\nabla\Phi_1(\boldsymbol{r},\omega))^2 + S(\boldsymbol{r},\omega) \approx S(\boldsymbol{r},\omega). \tag{5.9}$$

This is only fulfilled if

$$(\nabla\Phi_1(\boldsymbol{r},\omega))^2 \ll S(\boldsymbol{r},\omega). \tag{5.10}$$

This shows that within the validity of the first order Rytov approximation the scattering potential is linearly related to the refractive index:

$$S(\boldsymbol{r},\omega) \approx 2k_o^2 n_1^2(\boldsymbol{r},\omega). \tag{5.11}$$

This is only fulfilled when the following conditions are satisfied [101]:

$$\delta_n \ll 1 \tag{5.12}$$
$$|\nabla\Phi_1(\boldsymbol{r},\omega)| \ll k_o. \tag{5.13}$$

In Sect. 5.2.2. the exact physical constraints on the refractive index change in a CGVH that corresponds to the conditions in Eqs. (5.12) and (5.13) will be assessed.

5.2. A Novel Design Algorithm based on the First Order Rytov Approximation

In order to design CGVHs as voxelated volume optical elements using a projection based optimization algorithm similar to the one discussed in Sect. 3.4.2., a clear mathematical formulation of the physical constraints and of the quantization of the refractive index distribution is necessary. In Sect. 5.2.3 the numerical implementation of a volumetric design approach of CGVHs within the validity of the first Rytov approximation, that is based on the formulation that is discussed in Sect. 5.2.2 is presented. In Sect. 5.2.4 the validity of the physical constraints that are presumed in deriving the model presented here is assessed by comparing the results acquired to those predicted by the rigorous coupled wave theory for a given set of elementary CGVHs.

Hereby, a plane wave field (wave vector $\boldsymbol{k}_o$) which is incident on the CGVH is scattered in the bulk of the hologram thereby resulting in a total complex phase $\Phi(\boldsymbol{r}, \omega)$ - see Eq. (5.1). One portion of the total complex phase is in turn transformed into a projection $\Phi_s(\boldsymbol{r}, \omega)$, whereby this transformation can be formulated in terms of forward mapping operator:

$$\mathcal{P}_f : \Phi(\boldsymbol{r}, \omega) \longrightarrow \Phi_s(\boldsymbol{r}, \omega) \quad \forall (\boldsymbol{K}, \omega) \in W. \tag{5.14}$$

From equations (3.15) and (3.16), we can see that $\mathcal{P}_f$ defines a 3D mapping of the total field $\Phi(\boldsymbol{r}, \omega) \in \mathbb{C}^3$ by the potential $S(\boldsymbol{r}, \omega) \in \mathbb{R}^3$ in Eq. (3.4), on to the scattered phase $\Phi_s(\boldsymbol{r}, \omega) \in \mathbb{C}^2$. This physical implication becomes apparent when one considers the scattering process within the bulk of the hologram in frequency space as it is defined by Eqs. (3.15) and (3.16). Here, the values of the scattered field are seen to lie on a portion of the Ewald's sphere. We therefore conclude that Eq. (3.16) is a restatement of the Bragg condition for holograms designed using this approach. Thus, Eq. (5.14) presents the *forward problem* of designing CGVHs within the validity of the Rytov approximation.

5.2.1. Mathematical Background of the Projection Algorithm Adopted in this Work

In order to obtain a far-field distribution from the CGVH, we can infer from Eq. (5.8) that the incident wave field U_o must be modulated such that the scattered complex phase can be expressed in general as follows

$$\Phi_R(\boldsymbol{r}, \omega) = \mathcal{P}_f \left\{ S(\boldsymbol{r}, \omega) U(\boldsymbol{r}, \omega) \right\}. \tag{5.15}$$

Equation (5.15) presents the general form of the *forward problem* in Eq. (5.14) whose *inverse problem* we intend to solve. Thereby, the composite operator can be comprised of N set of projections, i.e. $\mathcal{P}_f = \mathcal{P}_N \cdots \mathcal{P}_1$. It can be described as the problem of finding the *cause* $S(\boldsymbol{r}, \omega)$ for a known *effect* ($\Phi_R(\boldsymbol{r}, \omega)$), under certain given physical constraints. From this we can infer that the problem of designing a CGVH evidently

involves finding the actual composition of the operator $\mathcal{P}$. One common trait of such inverse problems is that although an analytical *solution* usually does not exist, the properties of this solution are known. This *a priori* knowledge can thus be utilized to solve the problem by means of optimization theory. In the following we will outline how projection based optimization methods can be used to solve such a problem. These are numerical methods which can be used to compute an exact or optimal solution, which is an element of a feasible region defined by the intersection of a given number of sets.

To describe such an approach for the problem at hand, let us start by noting that the physical constraints imposed by these properties can be transformed into constraints on the scattering potential of the CGVH, thereby arriving at the sought solution which we will denote here by ψ. From a mathematical point of view, ψ can then be attained by finding the projection of this field onto a set of N constraints $C = C_1 \cdots C_N$. These constraints are thus seen to limit the size of the feasible solution subset C in a given space $\mathbb{H}$. A projection $P_n \{\psi\}$ of $\psi \in \mathbb{H}$ onto C_n is defined through the distance measure $E(\cdot, \cdot)$:

$$P_n \{\psi\} = \arg\min_{\psi \in C_n} E(\psi, \psi_o). \tag{5.16}$$

Commonly $E(\cdot, \cdot)$ is chosen to be the Euclidean norm such that

$$E(\psi, \psi_o) = \|\psi - \psi_o\|. \tag{5.17}$$

The feasible region C is defined as the intersection of all N constraint sets $C_n \subset \mathbb{H} : C \cap_{n=1}^{N} C_n$. The sought solution is consequently any function ψ^* that lies in this intersection [102, 103]:

$$\psi^* \in \bigcap_{n=1}^{N} C_n. \tag{5.18}$$

The approach adopted by projection based methods is one of finding this intersection by iteratively projecting ψ onto a given set. A general formulation of one iteration is hereby given by

$$\psi_{j+1} = \mathcal{P} \{\psi_j\}, \tag{5.19}$$

where j is the number of the iteration. To iterate from an initial point $\psi_o \in \mathbb{H}$ to a point in the feasible set C, the set of N projections defined above can be applied in a serial manner so that the iteration in Eq. (5.19) takes the following general form

$$\psi_{j+1} = \mathcal{P}_N \{\cdots \mathcal{P}_1 \{\psi_j\}\}. \tag{5.20}$$

5.2.2. Description of the Constraints imposed on the Discrete Scattering Potential of Multiplexed Volume Holograms

In analogy to CGHs, computer generated volume holograms can generally be described as holographic elements having a discreet scattering potential $S(\bar{r}, \omega)$ which determines

their optical functionality for a given wavelength. Likewise, this discreet scattering potential represents a sampled version of an unknown continuous function $S(\boldsymbol{r}, \omega)$:

$$S(\bar{\boldsymbol{r}}, \omega) = S(\boldsymbol{r}, \omega) \sum_{i=0}^{M} \sum_{j=0}^{N} \sum_{k=0}^{P} \delta \left(m\Delta x_i - x_i, n\Delta x_j - x_j, p\Delta x_k - x_k \right). \qquad (5.21)$$

Here, x_i, x_j and x_k are the components of $\boldsymbol{r}$ whereas Δx_i, Δx_j and Δx_k are the sampling distances in the i, j and k directions respectively.

The initial step in designing the CGVHs is to define a discreet scattering potential $S(\bar{\boldsymbol{r}}, \omega)$ in terms of a random refractive index distribution $n(\bar{\boldsymbol{r}}, \omega)$. This refractive index distribution is constrained to fit the fundamental physical constraints resulting from the conditions in Eqs. (5.12) and (5.13) as well as fabrication constraints. An overview of the constraints considered in the proposed design are summarized in Table 5.1. Since we applied an optical nonlinear absorption process to fabricate our holograms, one major fabrication constraint was the limitation of the sampling distances Δx_i, Δx_j and Δx_k by the achievable point spread function (PSF) for a given objective lens (cf. Sect. 6.1.3). This means that the actual scattering potential $S(\bar{\boldsymbol{r}}, \omega)$ which describes the modulation of the refractive index for each voxel depends on the dimensions and shape of the focal spot of the focused fs-laser beam. Therefore, $S(\bar{\boldsymbol{r}}, \omega)$ has a compact support only in the volume $\Sigma_{m,n,p}$ of a single voxel and can be written in terms of the ideal scattering potential $\hat{S}(\bar{\boldsymbol{r}}, \omega)$ and the PSF($\boldsymbol{r}$) as follows

$$S(\bar{\boldsymbol{r}}, \omega) = \hat{S}(\bar{\boldsymbol{r}}, \omega) \otimes \mathrm{PSF}(\boldsymbol{r}), \qquad (5.22)$$

where $\otimes$ denotes a 3D convolution.

In order to fabricate the CGVHs in the bulk of photosensitive glass-ceramics, a binary refractive distribution must be computed. This leads to two additional fabrication constraints, namely binary coding and positive refractive index change values. This means we assume that the imaginary part of n is zero or negligibly small, i.e. $\kappa \approx 0$ (see Eq. (2.32)). Therefore the choice of the coding approach, fabrication method (in this case a nonlinear absorption based laser lithography approach) as well as the type of substrate material used places constraints of the feasible optimal refractive index $\tilde{n}$ distribution - see Eq. (3.28). This can be expressed in the form of

$$\tilde{n} \in \mathcal{H} \left\{ n(\bar{\boldsymbol{r}}, \omega) \right\} \subset \mathbb{H}, \qquad (5.23)$$

where $\mathbb{H}$ denotes the set of refractive index distribution that is consistent with the constraints.

The angular multiplexing functionality of the CGVHs is introduced in the design process in form of a parallel projection based algorithm, whereby the scattered fields are extracted from the Ewald's sphere simultaneously for each illumination condition. In this work we follow the approach that was introduced in Sect. 3.4. As it is shown in Fig. 5.2 *(a)*, since the Ewald's sphere is defined in size and orientation by the incident wave vector $\boldsymbol{k}_\theta$ and the aperture of the imaging system is considered, a distinct sphere exists for each illumination condition. For each illumination condition that corresponds

Table 5.1.: A summary of the different constraints imposed on $S(\boldsymbol{K}, \omega)$ that characterize the set $\mathcal{H}\{\cdot\}$, i.e. the set of refractive index distribution $n(\bar{\boldsymbol{r}}, \omega)$ that is consistent with the design and fabrication of CGVHs in a nonlinear material - see Eq. (5.23).

Name	Constraint	Description
C_1	$n_1(\boldsymbol{r}) \in \{0, 1\}$	Binary index coding - Eq. (5.27)
C_2	$n(\boldsymbol{r}) \geq n_o$	Positive refractive index change
C_3	$0 \leq \delta_n \leq 10^{-2}$	Weak scattering - Eqs. (5.12) and (5.13)
C_4	$\Delta x_{i,j,k} \leq \mathrm{PSF}_{MPA}$	Voxel limit MPA (Sect. 6.1.3.)
C_5	$n_{\mathrm{IM}} \approx 0$	Non-absorbing refractive index change
C_6	$A_o = 1$	Unit amplitude reference wave
C_7	$A_t = \sqrt{I_t}$	Known target intensity
C_8	$I(f_x, f_y) \propto I(\Delta\Omega)$	Solid angle constraint

to a given plane reference wave $\boldsymbol{k}_\theta$, which is incident on the hologram at an angle θ, there exists a sphere which lies within the *Ewald's limiting sphere* of radius R_l [74, 81]. For the transmission CGVHs considered in this work, we are interested in the envelope of the spheres whose centers O_i are offset in the frequency domain of the scattering potential by - $\boldsymbol{k}_\theta$ from the center (cf. Fig. 5.2 *(a)*). Please note, each of the coordinates of the surface of each of these spheres can be computed from the other by means of a simple affine transformation. This fact can be used to increase the computational efficiency of the algorithm.

Unlike in the current state of the art, our approach includes an extra intensity mapping step between the values defined across a remote plane in the far-field of the CGVH and the circular surface of the Ewald's sphere. Instead of applying a linear interpolation scheme, we start by noting that since the different far-field projections are to be superposed across a planar surface, e.g. of a CCD sensor, each pixel on this plane then integrates the light scattered within a solid angle $\Delta\Omega(\boldsymbol{k_s})$. A general measure of this scattered intensity $I(\Omega)$ is the differential cross section. Unfortunately, $\Delta\Omega(\boldsymbol{k_s})$ decreases with the increase in spatial frequency as it is shown in Fig. 5.2 *(b)*. This in turn means that projections to the middle part of the Ewald's sphere tend to be larger than those towards the polar regions, which leads to artifacts in the synthesized fields. To remedy this problem a bi-cubic interpolation, whereby $\Delta\Omega(\boldsymbol{k_s})$ (see Fig. 5.2 *(c)*) is considered during this computation, was implemented. This was done using the following spherical polar coordinates

$$f_x = \frac{2\pi}{\lambda}\sin(\vartheta)\cos(\phi)$$
$$f_y = \frac{2\pi}{\lambda}\sin(\vartheta)\sin(\phi) \tag{5.24}$$
$$f_z = \frac{2\pi}{\lambda}(\cos(\vartheta) - 1),$$

where ϑ and ϕ are the spherical polar angles. A block diagram of the design algorithm
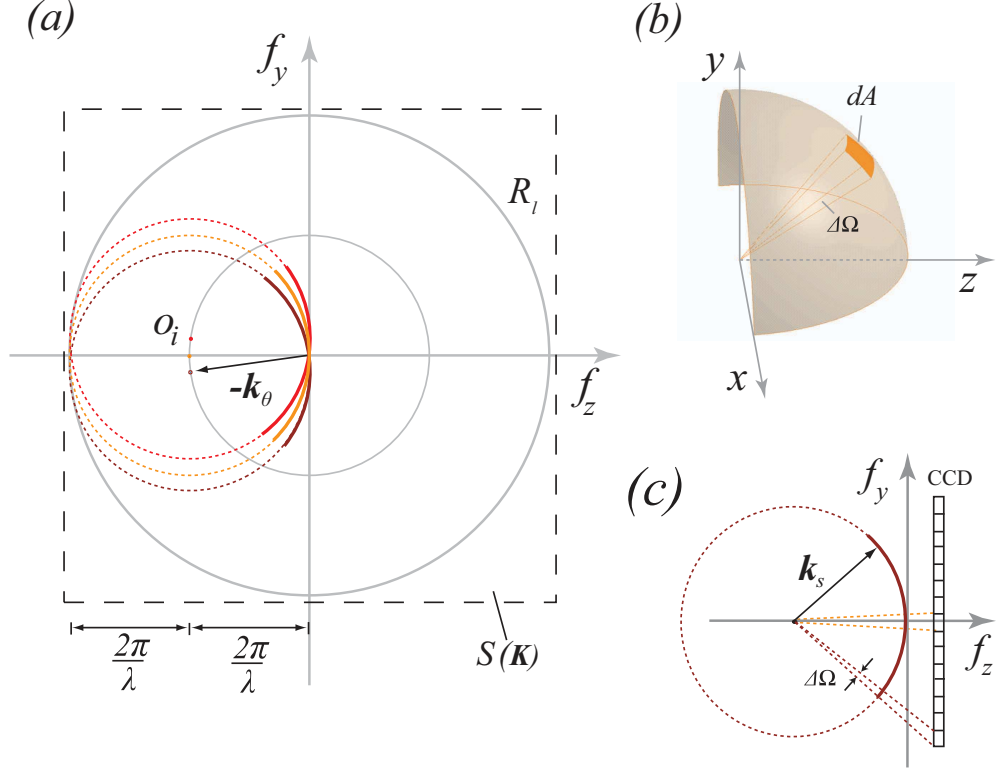
Figure 5.2.: *(a)* Cross section of the frequency space geometric construct, illustrating how the scattered fields can be extracted from the Fourier transformed scattering potential $S(\boldsymbol{K})$. For a transmission CGVH there exists a distinct sphere, whose center O_i is offset by the vector - $\boldsymbol{k}_\theta$, for each reference wave incident on the CGVH at an angle θ. All these spheres lie within an envelope of the limiting Ewald's sphere which has a radius R_l. *(b)* Representation of the scattering problem in terms of the differential cross section, whereby the field scattered within a given solid angle $\Delta\Omega$ is mapped onto a certain area dA on the Ewald's sphere. *(c)* These values are projected onto a planar detector, whereby each pixel on this plane integrates the light scattered within a solid angle $\Delta\Omega$.

developed in this work is depicted in Fig. 5.3 and a detailed description of the single steps is presented in Sect. 5.2.3.

5.2.3. Numerical Implementation

The design algorithm which is based on the first order Rytov approximation can be summarized in five steps as follows:

1. In the initial step, a discrete scattering potential $S_j(\bar{\boldsymbol{r}}, \omega)$ for a desired CGVH composed of $M \times N \times P$ number of voxels is initialized by generating a random refractive index contrast $n(\bar{\boldsymbol{r}}, \omega)$ as an initial guess. Here, we introduce constraint C_4 (see Table 5.1.) for the designed refractive index distribution by considering the fact that the achievable voxel sizes are determined by the absorption profile of the MPA for a given set of fabrication parameters. Furthermore, the spherical coordinates of the indivndual portions of the Ewald's sphere are pre-calculated using the relations in Eq. (5.24).

2. To attain the resulting scattered fields, a forward projection operator is applied on the scattering potential. Hereby, a 3D forward FFT of the scattering Potential is computed and the far-field projections are extracted from the corresponding portion of the Ewald's sphere for each illumination direction. From Eqs. (3.14), (3.16) and (5.8) the scattered field for a given incident field $\boldsymbol{k}_\theta$ can be expressed in frequency space as

$$\tilde{U}_j(\boldsymbol{K}, \omega) = \exp\left[\frac{\mathrm{e}^{\mathrm{i}kr}}{r}\tilde{S}(\boldsymbol{K}, \omega)/U_o(\bar{\boldsymbol{r}}, \omega)\right]. \tag{5.25}$$

3. Each of these single far-field projections is then evaluated, and the amplitude constraint C_6 (see Table 5.1.) is applied, thereby resetting the amplitude throughout the field in order to better approximate the target intensity $I_t(\boldsymbol{K}, \omega)$. However, the phase information is preserved:

$$\tilde{U}_j(\boldsymbol{K}, \boldsymbol{\omega}) = \begin{cases} c_k \sqrt{I_t(\boldsymbol{K}, \boldsymbol{\omega})} \cdot \mathrm{e}^{[\mathrm{i}\phi_j(\boldsymbol{K}, \boldsymbol{\omega})]} & \forall (\boldsymbol{K}, \boldsymbol{\omega}) \in W \\ \tilde{U}_j(\boldsymbol{K}, \boldsymbol{\omega}) & \text{otherwise,} \end{cases} \tag{5.26}$$

where $\phi_j(\boldsymbol{K}, \boldsymbol{\omega}) = \arg\{\tilde{U}_j(\boldsymbol{K})\}$ is the unmodified phase. We hereby assume that $I_t(\boldsymbol{K}, \boldsymbol{\omega})$ is only given within the limited signal window W. A bicubic interpolation is employed to map $I_t(\boldsymbol{K}, \boldsymbol{\omega})$, which is defined across a planar detector surface, onto the circular manifold of the Ewald's sphere. This is done by computing the coordinates on the Ewald's sphere that correspond to a single pixel on the detector. The weighting factor c_k is introduced here to ensure the convergence of the algorithm and was determined here heuristically by means of a parameter scan.

4. The modified and unmodified sections of the Ewald's spheres are recombined to obtain $\tilde{S}_j(\boldsymbol{K}, \boldsymbol{\omega})$ and an inverse projection operator is used to compute a new scattering potential, i.e. $\acute{S}_j(\bar{\boldsymbol{r}}, \omega) = \mathcal{F}_{3D}^{-1}\left\{\tilde{S}_j(\boldsymbol{K}, \boldsymbol{\omega})\right\}$.

5. To obtain an approximated binary refractive index contrast $\tilde{n}_j$, a fabrication constraint is imposed on this new scattering potential as follows

$$S_{j+1}(\bar{\boldsymbol{r}}, \omega) = \begin{cases} \frac{1}{4\pi}k^2 \left[n_j^2(\bar{\boldsymbol{r}}, \omega) - n_o^2\right] & \forall \acute{S}_j(\bar{\boldsymbol{r}}, \omega) \geq \frac{1}{8\pi}k^2 \left[n_j^2(\bar{\boldsymbol{r}}, \omega) - n_o^2\right] \\ 0 & \text{otherwise.} \end{cases} \quad (5.27)$$

The overall refractive index contrast is finally computed, $S_{j+1}(\bar{\boldsymbol{r}}, \omega)$ is set as the new scattering potential and *steps (2-5)* are repeated until the algorithm converges to an optimum solution $\hat{n}$. To monitor the convergence of the algorithm, both the SNR of the signal within the window W (see Fig. 5.4) and the average value of δ_n (see Fig. 5.5) were computed at each iteration.
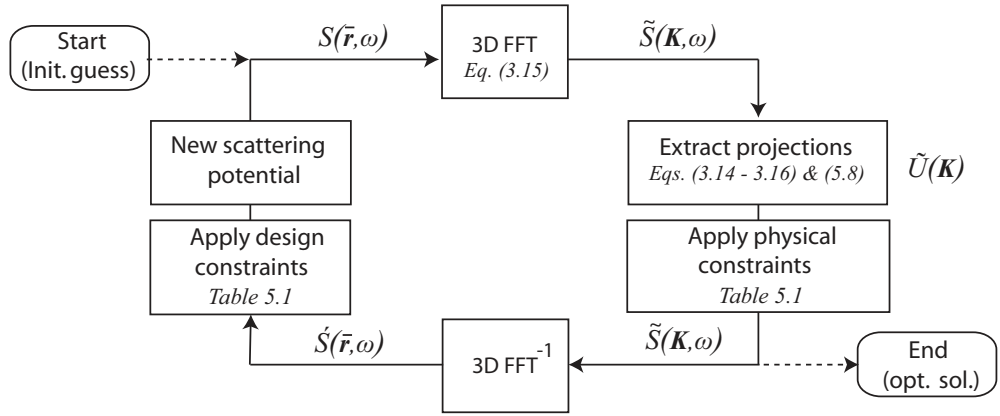

Figure 5.3.: A block diagram of the proposed iterative Fourier transform based bi-directional algorithm for the design of CGVHs within the validity of the first Rytov approximation.

5.2.4. Validation of the Model

In order to verify the hypothesis of this work, a set of CGVHs were designed using both the Born and Rytov approximation based approaches. The designed holograms were characterized in terms of signal-to-noise ratio as well as the computed refractive index distribution. In this section results of these numerical experiments are presented.

Performance of the Proposed Approach

For an initial analysis on the performance of the proposed approach two different CGVHs having the following parameters are discussed: a thickness of $L_z = 192\,\mu$m, a

lateral size of $L_{x,y} = 128\,\mu$m and the wavelength of illumination $\lambda = 532$ nm. In each hologram three projections are encoded, whereby each projection has a Bragg angle θ_B. The Bragg angle of each of these holograms is offset at an angle of 7° from the other. The target intensity I_t is presented by 64 x 64 samples. The holograms were zero-padded during the design process, thus resulting in CGVHs with 128 x 128 x 128 voxels. Additionally, a third hologram with a slightly larger thickness, $L_z = 288\,\mu$m, and the same parameters as the first two is used here to analyze the performance of the proposed approach as the size of the CGVH increases. For all holograms the iterative algorithm was terminated after 25 iterations and the SNR of the signal was computed at each iteration. SNR (measured in dB) is computed here as a practical measure of performance for a given projection Φ_i as follows:

$$SNR = 10\log_{10}\left[\frac{\|A_t(\boldsymbol{K},\omega)\|^2_{\forall(\boldsymbol{K},\boldsymbol{\omega})\in W}}{\|A_t(\boldsymbol{K},\omega) - A_j(\boldsymbol{K},\omega)\|^2_{\forall(\boldsymbol{K},\boldsymbol{\omega})\in W}}\right], \tag{5.28}$$

where $A_t = \sqrt{I_t}$ and $A_j = \left|\tilde{U}_j\right|$ are the amplitudes of the target and designed far-field projections for a given illumination condition respectively. The results in Fig. 5.4 show the performance of these CGVHs. For the case when the size of the CGVH is small (see Eq. (4.3)), both the model based on the first Born approximation and our first Rytov approximation based approach are seen to change the SNR from 0 to 5.9 dB after 25 iterations. These results are thus seen to agree with our theoretical
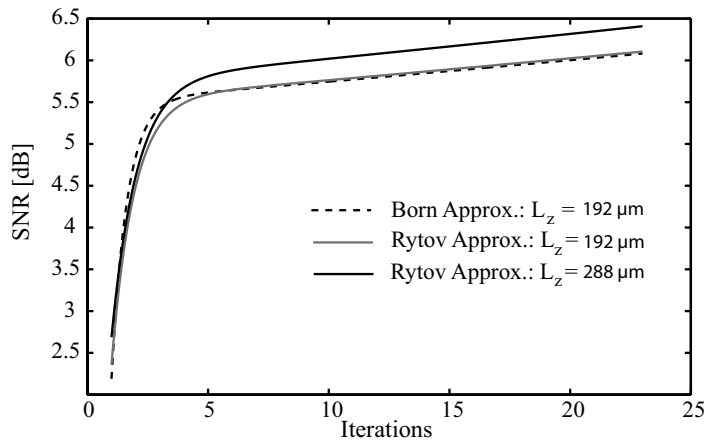

Figure 5.4.: Comparison of the models in terms of the SNR of a single projection. It is clear as stated in Sect. 4.1. that for small values of δ_n and L_z, both models have the same results - see Eq. (4.3). But as the size of the hologram increases, the proposed algorithm computes a result with an even higher SNR as expected, whereas no functional hologram could be computed for this thickness using the first Born approximation.

expectation. However, as the thickness of the hologram increases, our proposed method is seen to produce better SNR values (in this case 6.4 dB) in analogy to the previously

discussed volume phase holograms. On the other hand, no functional hologram, i.e. one that fulfills the constraints of the proposed hybrid system, could be computed for the thickness of $L_z = 288 \, \mu$m using the first Born approximation based approach.

Investigation on the Validity of Various Constraints

In addition to the computation of the performance measure in terms of SNR, the average refractive index change was computed at each iteration for the holograms discussed in the previous section. These results are used here to evaluate the implications of the refractive index constraint - cf. Eq. (5.12).

In Fig. 5.5 results of the convergence behavior of the design algorithm in terms of the average refractive index change, for the two similar CGVHs discussed in the previous subsection, are shown. It can been seen clearly that the design algorithm based on the Rytov model converges towards a δ_n value on the order of 10^{-2}, whereas the Born model converges towards a δ_n value on the order of 10^{-3}. We can thus conclude that
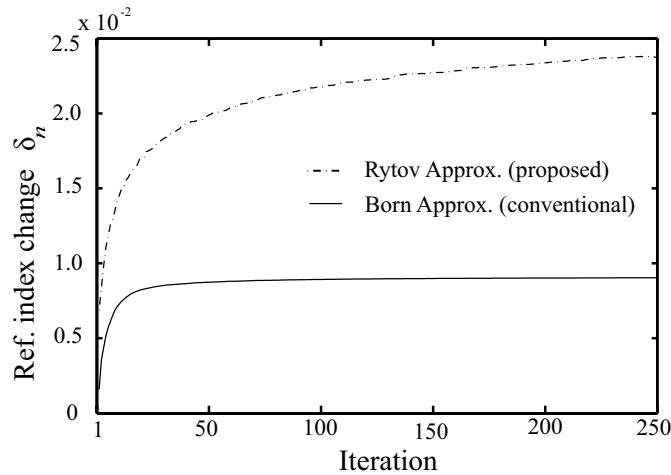

Figure 5.5.: Comparison of the convergence behavior of the design algorithm for both the model based on the Rytov approximation (broken line) and the conventional method which is based on the Born approximation. It is apparent from these results that in the former, the algorithm eventually converges to an average refractive index change δ_n value on the order of 10^{-2}, whereas the latter converges to a δ_n value on the order of 10^{-3} - after Kamau *et. al.* [17].

using the Rytov model functional multiplexed CGVHs with a refractive index contrast within the range of $\delta_n = 10^{-4} \cdots 10^{-2}$ can be designed. This shows the flexibility of this design approach in terms of the feasible range in achievable δ_n values and hologram thickness. As we have shown in our previous work [47], this increase in thickness leads to an increased SBWP. Additionally, the proposed algorithm does not stagnate after a few iterations as in the case of the conventional approach as the size of the CGVH increases. This can be attributed to the introduction of further constraints (see Table

5.1) and a more precise modeling of the scattering process within the bulk of the hologram.

In order to get additional insight on the propagation of different reference waves in the volume of the multiplexed CGVHs, 3D numerical simulations were used. Thereby, the Fourier based beam propagation method (FFT-BPM) was used to study a set of CGVHs. FFT-BPM is a computational technique in optics, which is used to numerically solve the wave equation (see Sect. B.1). It is one of the most widely applied methods for the analysis and simulation of guided wave propagation in inhomogeneous media [104]. The main goal of this analysis was to design a CGVH with an analytically known response using our Rytov approximation based model and then compare this response with the one attained by means of numerical simulations. For instance, let us assume that a given projection Ψ_i is defined as a 2D circularly symmetric Gaussian function across a plane $\{s\}$ in the far-field of the CGVH, i.e.:

$$\Psi_i(\boldsymbol{s}) = A \exp\left[-\pi \frac{(\boldsymbol{s} - \boldsymbol{q}_o)^2}{2\sigma^2}\right],\tag{5.29}$$

where $A = 1/\sigma\sqrt{2\pi}$ is the amplitude and $\boldsymbol{q}_o$ is a known spatial carrier - Sect. 2.3.2. We can expect that a CGVH that projects such an elementary far-field distribution will depict some periodicity in the designed refractive index distribution. This becomes more clear if we consider the limiting case of the distribution in Eq. (5.29) as $\sigma \longrightarrow 0$. In this case the projection becomes a Dirac distribution $\delta(\boldsymbol{s}-\boldsymbol{q}_o)$, which in turn implies the scattered field is a plane wave. Consequently, the CGVH will adopt the form of a periodic volume phase hologram - cf. Sect. 3.3.1.

Figure 5.6 *(a)* shows the binary refractive index distribution for a CGVH that projects a far-field distribution which is given by Eq. (5.29). In Figs. 5.6 *(b)*, *(c)* and *(d)* the FFT-BPM results of simulated propagation of a Gaussian beam through this CGVH are shown. In *(b)*, it can be seen clearly that the incident beam is scattered in the bulk of the hologram and that the resulting complex phases $\Phi_o(\boldsymbol{r}, \omega)$ and $\Phi_s(\boldsymbol{r}, \omega)$ are initially coupled as expected - see Sect. B.2. However, in the far-field of the CGVH the distribution of the scattered field assumes a Gaussian distribution (Fig. 5.6 *(a)*).

Here, we additionally analyzed the case where constraint C_5 is not fulfilled, i.e. the case where the imaginary part of the induced refractive index is not zero. We particularly simulated the case where the refractive index distribution is given by Eq. (2.32). We thereby assumed that the refractive index modulation introduced in the fabrication process is in one case purely real and in the other case it has an equal real and imaginary part. In Figs. 5.6 *(c)* and *(d)* a comparison between these two cases are shown in terms of the diffraction efficiency, which can be expressed as

$$\eta = \frac{\|A_s(\boldsymbol{s})\|^2_{\forall(\boldsymbol{K},\boldsymbol{\omega})\in W}}{\|A_o(\boldsymbol{x})\|^2},\tag{5.30}$$

where $A_s = \|U_j(\boldsymbol{K}, \omega)\|$ is the magnitude of the scattered field across a plane $\{s\}$ and $A_o = \|U_o(\boldsymbol{K}, \omega)\|$ that of the illumination field across the entrance plane $\{x\}$.

Hereby, $U_j(\boldsymbol{K}, \omega)$ is the field given in Eq. (5.25). We can see from these results that the imaginary part leads to absorption losses. However, since both the phase relation between the scattered and the non-scattered fields are influenced only marginally this leads to very a little influence on the angular selectivity of the hologram. Similar results have been observed with other types of holograms [105]. We can thus conclude that as long as the imaginary part of the induced refractive index is negligibly small, the optical functionality of CGVHs remains unchanged.
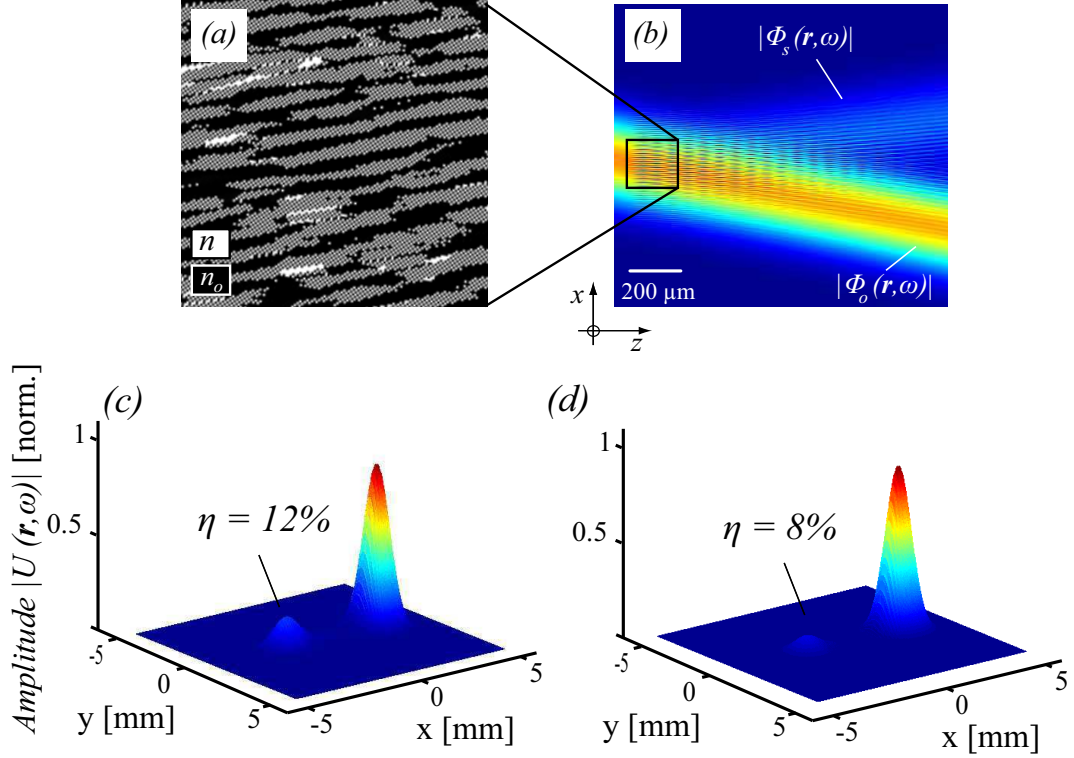

Figure 5.6.: *(a) Axial slice of the optimized binary refractive index CGVH (where n and n_o are given by Eq. (3.6)) that projects an elementary circularly symmetrical Gaussian intensity distribution. (b) Results of an investigation on the transmission of a Gaussian beam through this CGVH using a Fourier transform based beam propagation simulation method, whereby in the near-field the complex phases $\Phi_o(\boldsymbol{r}, \omega)$ and $\Phi_s(\boldsymbol{r}, \omega)$ are initially coupled. In (c) and (d) the normalized amplitudes of the total field $U(\boldsymbol{r}, \omega)$ in the far-field of the CGVH are shown for a purely transmittive and a lossy CGVH respectively.*

5.3. Novel Hybrid System

5.3.1. System Geometry

Figure 5.7 depicts a sketch of an optical setup that was conceived for the dynamic decoupling of single or a set of far-field projections from one CGVH. Such a setup allows for a precise, non-mechanical and robust modulation of single reference waves [106]. Hereby, the objective lenses L_1 and L_2 (focal length f_1 and f_2)) form a $4f$ optical setup within a spatial light modulator is positioned. This setup allows for the dynamic decoupling of individual projections from the CGVH by inscribing the transfer function $H(\boldsymbol{\nu})$ on the SLM, whereby $\boldsymbol{\nu}$ are spatial frequencies.

SLMs can modulate the phase of an optical beam with just a few millisecond response time and a large angle scan range. In general it is possible to utilize various degrees of freedom which are provided by a spatial light modulator. These degrees of freedom could for instance include utilizing various diffraction order terms [107] or linearly shifted plane waves [106], which can be generated by inscribing predefined transfer functions on the SLM. The feasibility of wave field modulation using the latter example for the purpose of dynamically decoupling a set of fields that are encoded in a single CGVH is discussed in Sect. 5.3.2.
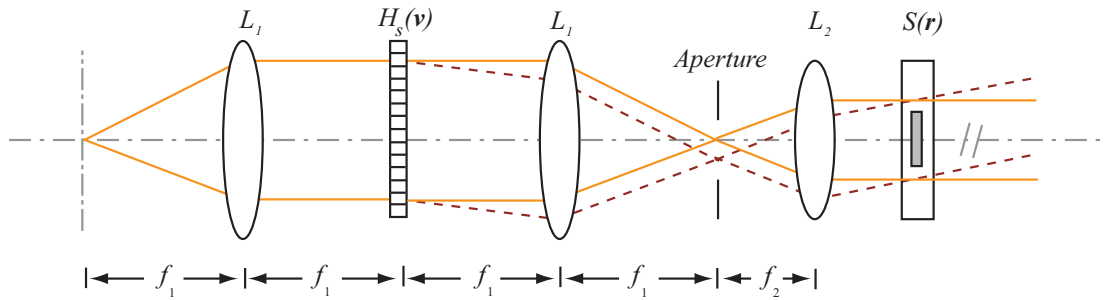

Figure 5.7.: Conceptual layout of the novel hybrid system proposed in this work, whereby an optoelectronic wave field modulation scheme is used to dynamically decouple various far-field projections from a volume holographic element. The objective lenses L_1 and L_2 (focal length f_1 and f_2)) form a $4f$ optical setup within a spatial light modulator is positioned. This setup allows for the dynamic decoupling of individual projections from the CGVH by inscribing the transfer function $H(\boldsymbol{\nu})$ on the SLM.

5.3.2. Optoelectronical Wave Field Modulation Using a Phase-only SLM

The configuration depicted in Fig. 5.7 makes use of an electronically addressed reflective phase-only SLM, which allows for the adaptive manipulation of the impinging wave. The SLM is regarded here as a non-mechanical multiple angle beam splitting

device. For instance, the 2D Fourier shift theorem can be applied to shift a wave field in the frequency space. The spectrum of the shifted field, with a shift s, is in this case the Fourier transform of the original field modulated by the linear transfer function

$$H_s(\boldsymbol{\nu}) = \mathrm{e}^{-\mathrm{i}2\pi\boldsymbol{\nu}s}. \tag{5.31}$$

Such a modulation can be achieved optically with the help of a $4f$-setup. Hereby, the wave field is first Fourier-transformed using a lens with a focal length f. An SLM is then placed in the Fourier plane of this lens. Across this plane there will be a field $U_f(\boldsymbol{r'})$, whose complex valued amplitude at the position defined by $\boldsymbol{r'}$ is proportional to the Fourier transform of the field $U_i(\boldsymbol{r})$ incident at the front focal point of the lens at the position $\boldsymbol{\nu} = \boldsymbol{r'}/\lambda f$, i.e. [2]:

$$U_f(\boldsymbol{r'}) = \frac{1}{\mathrm{i}\lambda f} \cdot \mathcal{F}\left\{U_i(\boldsymbol{r})\right\}\left(\frac{\boldsymbol{r'}}{\lambda f}\right), \tag{5.32}$$

where $\mathcal{F}$ denotes the Fourier transform operator. From Eq. (5.31) if the complex transmittance

$$t_s(\boldsymbol{r'}) = H_s\left(\frac{\boldsymbol{r'}}{\lambda f}\right) = \exp\left[-\mathrm{i}2\pi\frac{\boldsymbol{r'}}{\lambda f}s\right] \tag{5.33}$$

is generated by the SLM and an identical lens is introduced at a distance of $2f$, the shifted wave field exiting the $4f$-setup can be written as

$$\begin{aligned} U_f(\boldsymbol{r''}) &= \mathcal{F}\left\{\mathcal{F}\left\{U_i(\boldsymbol{r})\right\}t_s\right\} \\ &= -U_i(-(\boldsymbol{r''} - s)), \end{aligned} \tag{5.34}$$

which is clearly a copy of the translated field U_i - but one that is rotated by 180°. A set of shifted plane waves k_i, which correspond to individual reference waves impinging on the CGVH at different angles, can then be coupled into the hologram thereby dynamically synthesizing a given set of far-field projections Ψ_i as shown in Fig. 5.1. Moreover, a set of arbitrary orthogonal elementary waves can be coherently superposed in order to attain the complex valued field

$$U(\boldsymbol{r}) = \sum_{i=1}^{I} A_i \mathrm{e}^{\mathrm{i}\phi_i} \cdot \psi_i(\boldsymbol{r}), \tag{5.35}$$

where each $\psi_i(\boldsymbol{r})$ and therefore $U(\boldsymbol{r})$ has a large SBWP. Owing to the birefringence property of the SLM, only light that is polarized along its slow axis is modulated, while light polarized along the fast axis remains unchanged [43]. This property can be used additionally for multiplexing as it will be discussed in the next section.

6. Experimental Results: Fabrication of CGVHs in a Nonlinear Optical Material and Characterization of Their Optical Functionality

To facilitate the assessment of the devices described in the previous chapter a series of experiments, which will be described in this chapter were undertaken. These experiments were performed, *(a)* to ascertain the feasibility of fabricating multifunctional CGVHs using a 3D laser lithography method; *(b)* to assess the suitability of photosensitive glass-ceramics for this fabrication using a nonlinear absorption process approach and *(c)* to deliver a proof of principle for the hypothesis of this work by characterizing the performance of CGVHs designed and fabricated within the validity of the Rytov approximation.

6.1. Fabrication of CGVHs in Nonlinear Optical Materials

Three dimensional laser micro- and nanofabrication has become a fast growing field of science and technology. Particularly in the case of dielectric materials, this opens up a wide range of material processing processes in the micro- and nanometer range. One such process involves 3D structuring within the bulk of the material by means of a laser direct writing process. In the current state of the art [56, 108], fabrication of holograms in glass has been reported. Feasibility of fabricating CGVHs in nonlinear optical materials, which allows for the realization of devices with much smaller voxel dimensions has however not been investigated. In this section, the fabrication of CGVHs in a photostructurable glass-ceramic by means of femtosecond direct laser writing and the corresponding nonlinear absorption process are discussed.

6.1.1. Photostructurable Glass-Ceramics

Glass-ceramics (GC) are manufactured by adding dopant compounds in a base material like glass. This provides the potential to tailor a specific functional property

either on the local or global scale. The photostructurable GC material used in this work was Foturan$^{\text{TM}}$ glass. This is a glass which mainly consists of silica, stabilizing admixtures, a nucleating agent and a photoactive component. Table 6.1 summarizes the typical concentrations of commercially available Foturan substrates [95].

Foturan glass and other GCs, e.g. chalcogenide glasses, are generally manufactured in the amorphous glass state and contain a photoactive component that permits the controlled modification of the refractive index of the material following exposure to a given radiation. A further advantage of this GCs is the fact that they can be transformed to a composite material in a subsequent heat treatment through a controlled nucleation and crystallization of the GC constituents [95, 109].

6.1.2. Optical Nonlinearlity in Photostructurable Glass-Ceramics

As previously discussed in Sect. 2.1.2., an electromagnetic wave incident on a nonlinear medium will polarize it causing it to develop a time dependent electrical polarization. The optical response of the material to an optical electromagnetic field can be described by considering the effect of the field on an atom. The electric field acting on the positive and negative charges of the atom distorts the electron charge distribution in the atom. A primary measure of this distortion is the electric dipole moment induced in the atom by the electric field. The overall macroscopic electric polarization $\boldsymbol{\mathcal{P}}(t)$, cf. Eq. (2.39), can then be obtained by summing up such dipoles over a given sample volume and dividing by the volume. Of particular interest in this work, are the nonlinear reactions resulting from this polarization after tightly focusing a laser beam into the bulk of a photostructurable GC.

In this work we are specifically interested in the nonlinear multiphoton absorption process induced in the bulk of a dielectric material. For this purpose we use a near infra red laser source and a high numerical aperture (N.A.) objective to focus a laser beam into the bulk of a GC material. The main aim is to concentrate high electromagnetic energy densities into a tiny volume ($\approx \mu\text{m}^3$). This process can induce a number of nonlinear reactions e.g., self phase modulation; self focusing; multiple photon absorption and avalanche ionization. However, by appropriately choosing the magnitude of the electric field and spatially controlling these defective regions we can be able to create the desired subsurface structures [95, 110].

If we consider a plane electromagnetic wave propagating into a nonlinear medium, and by taking the Maxwell equation in Eqs. (2.1) - (2.4), the following wave equation can be deduced - cf. Eq. (2.38)

$$\nabla^2 \boldsymbol{\mathcal{E}} - \mu_o \epsilon_o \frac{\partial^2 \boldsymbol{\mathcal{E}}}{\partial t^2} = \mu_o \frac{\partial^2 \boldsymbol{\mathcal{P}}^{NL}}{\partial t^2}. \tag{6.1}$$

Hereby we have only consider the third-order nonlinear polarization

$$\boldsymbol{\mathcal{P}}^{NL} = \chi_{ijkl}^{(3)} \boldsymbol{\mathcal{E}}_j \boldsymbol{\mathcal{E}}_k \boldsymbol{\mathcal{E}}_l \tag{6.2}$$

Table 6.1.: Overview of typical constituents and concentrations (in mass percentage - wt%) found in a commercially available Foturan photostructurable glass-ceramic [95].

Constituents	wt%	Description
Primary substrate:		
SiO_2	75 - 85	Base glass
Admixtures:		
Li_2O	7 - 11	Stabilizer
K_2O and Al_2O_3	3 - 6	Stabilizer
Al_2O_3	1-2	Stabilizer
ZnO	< 2	Stabilizer
Ce_3O_3	0.01 - 0.04	Photoactive component
Ag_2O	0.05 - 0.15	Nucleating agent

since previous investigations on the mechanism of the photoreaction of the photosensitive glass to the infrared fs laser has shown that the third order susceptibility is the largest contributing factor to the electromagnetically induced polarization in the GC used in this work [95, 96]. From Eqs. (2.18), (6.1) and (6.2), an approximated change of irradiance with depth into the sample can be expressed as follows [62, 95, 110]

$$- \frac{\mathrm{d}}{\mathrm{d}z} \acute{I}(z,t) \approx \alpha_3 \acute{I}^3(z,t),$$

(6.3)

where the three-photon absorption coefficient is defined as:

$$\alpha_3 = \frac{5\omega}{2n_o^3 c^3 \epsilon_o^3} \chi^{(5)}$$

(6.4)

6.1.3. Multiphoton Absorption Process

Initially a comprehensive analysis of the feasibility of fabricating CGVHs in the bulk of photosensitive glass was undertaken. One principle task thereby involved the determination of the peak power density needed to induce photomodification within the volume of a single voxel using a setup that is schematically shown in Fig. 6.1. This entailed experimentally investigating the predictions made in Sect. 6.1.2. For this purpose, we employed an fs-laser with the following parameters: wavelength $\lambda = 1550 \, \mathrm{nm}$, repetition rate up to 100 kHz, pulse duration up to $E_p = 50 \, \mu\mathrm{J}$ and pulse energy $\tau < 800 \, \mathrm{fs}$. An appropriate amount of light from the fs-laser had to be focused using a microscope objective (40X; NA = 0.75) in order to achieve conditions where nonlinear absorption is induced in the focal region only. This absorption would lead to the generation of non equilibrium charge carriers in the area localized within the focal spot. In a multiphoton absorption process [111], this focal region is usually elongated

in the beam's propagation direction and the intensity distribution within it depicts an elliptic form [95]. This distribution represents the point spread function in the focal spot of a laser beam focused using an objective of a given numerical aperture. The size of the focal spot thus dictates the achievable resolution in terms of the achievable PSF - cf. Eq. (5.22).

To experimentally approximate the PSF for our system, the dimensions of the focal spot was determined by means of microscopy for different pulse energies and number of pulses. The threshold for photomodification was found to lie approximately above 100 pulses at the target pulse energy of $5\,\mu$J for the set of system parameters presented above. Minimum lateral focal spot sizes on the order of $\delta_x \leq 1\,\mu$m were measured. This values are much smaller than the diameter of the focal spot of the fs-laser used, since the nonlinear absorption process takes place only in a region smaller than the focal spot. An even better resolution could be achieved with this system by using a high NA objective and carefully controlling the energy deposition.

In order to inscribe CGVHs with voxel sizes of $(\Delta x, \Delta y, \Delta z)$, an XPS-controller (Newport XPS-C8) was used to facilitate a point-to-point positioning of the GC. Thereby, the focal spot of the laser is translated inside the material along the desired path with high precision and accuracy. Exact motion trajectories could thus be defined such that a series of focal spots overlap within the volume of a single voxel. Furthermore, the XPS-controller was used to precisely trigger the fs-laser and the translation stages such that a predefined peak power density is delivered for each voxel. As a result, optical elements having dielectric features such as the VPH shown in 6.1 (a) can be realized. This method is commonly reffered to as direct laser writing (DLW) [112, 113].
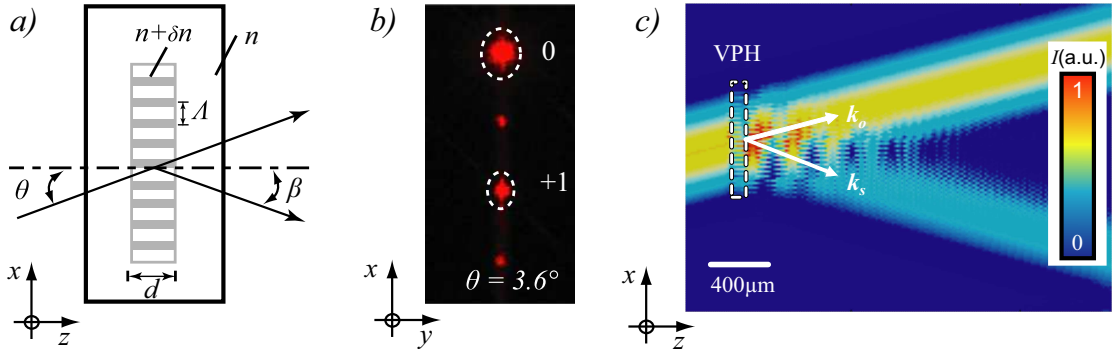

Figure 6.1.: (a) Schematic of the setup used to determine the Bragg angle of volume hologram, from which the induced refractive index could be determined. (b) Diffraction pattern of a CGVH with a thickness of 120 μm, having a sinusoidal refractive index modulation with $\delta_n = 1 \cdot 10^{-3}$ and illuminated with a He-Ne laser beam incident on it at the Bragg angle θ_B. (c) BPM simulation of the transmission of a Gaussian beam through the hologram studied in (b) - after Bülters et. al. [48].

In order to characterize our DLW system and thereby assess the feasibility of fabricating CGVHs in the bulk of Foturan glass, a series of experiments as well as simulations were undertaken. In a first step, experiments were conducted to determine the optimum pulse energy for inducing a refractive index change on the order of $\delta_n \approx 10^{-4} \cdots 10^{-2}$. This was achieved by first inscribing a volume grating in the glass and then measuring the Bragg angle θ_B using the setup shown in Fig. 6.1 (a). The thickness of the grating was $L_z = 120 \,\mu$m and the grating period was $\Lambda = 5 \,\mu$m. Given θ_B, the induced refractive index change could be calculated using Eq. (3.20). Concurrently, FFT-BPM was used to investigate the transmission of a light through a VPH, which is embedded in the bulk of the material. This was modeled as a weak scattering element having a sinusoidal refractive index modulation, whereby the peak refractive index change was taken to be $\delta_n \approx 1 \cdot 10^{-3}$. Figs. 6.1 (b) and (c) show the results of the experiment and the simulation respectively. It is apparent from this results that the volume grating produces a single diffraction order at the Bragg angle. Furthermore, these results show a good agreement between the simulation and the experiment.
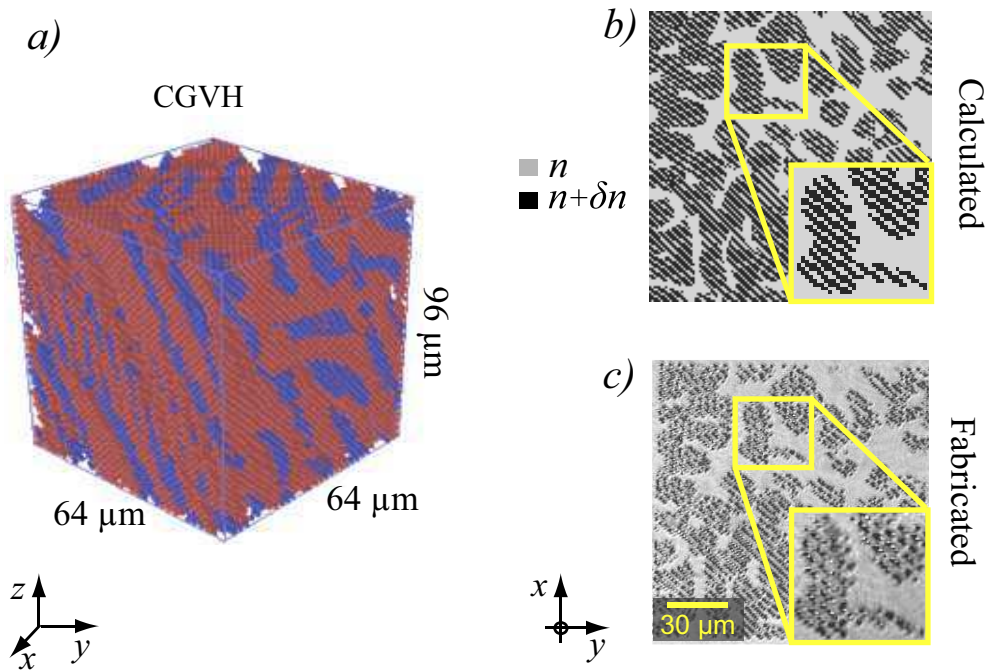

Figure 6.2.: (a) 3D representation of calculated refractive index modulation for a CGVH with a size of 64 x 64 x 96 μm^3, (b) top layer of the CGVH and (b) a phase contrast micrograph after fabrication in a nonlinear optical material - after Kamau *et. al.* [57].

These preliminary studies paved the way to the fabrication of computer generated volume holograms in the bulk of Foturan glass. Fig. 6.2 (a) shows a 3D representation of the refractive index modulation for a CGVH with a size of 64 x 64 x 96 μm^3 that was first fabricated in Foturan glass. In Fig. 6.2 (b) the refractive index distribution $n(\boldsymbol{r})$

of the top layer of this binary CGVH is shown. After the fabrication of this CGVH a differential interference contrast (DIC) microscope measurement of the index contrast in Fig. 6.2 *(b)* was recorded - see Fig. 6.2 *(c)*.

These results clearly demonstrate for the first time that CGVHs with smooth internal contours and smaller voxel dimensions ($\Delta x = \Delta y = 1$ μm) than in the current state of the art ($\Delta x = \Delta y = 2$ μm) can be fabricated in a photosensitive glass by nonlinear laser induced 3D modification of refractive index.

6.2. Experimental Characterization of Fabricated CGVHs

The CGVHs that were fabricated as discussed in the previous section were experimentally investigated in order to characterize their performance in terms of diffraction efficiency and Bragg selectivity. In the following these experiments are described and the acquired results are presented.

6.2.1. Optical Setup

Figure 6.3 shows the setup realized for wave field synthesis through angular multiplexing. Hereby, an SLM with 1920×1080 pixels and a pixel pitch of 8 μm is located in its Fourier plane of the first objective lens ($f = 105$ mm) and is illuminated with a collimated laser beam ($\lambda = 532$ nm) from a diode laser. The modulated reference beam is then Fourier-transformed by a second objective lens as described in Sect. 5.3.2. An aperture is placed in the Fourier plane to block unwanted higher diffraction orders resulting from the SLM. The beam behind the second objective lens is collimated using a lens ($f = 10$ mm) which allows the reference beam to sweep through an angle range of approximately $\pm 10°$. A second aperture is placed behind this lens making the beam as small as possible. The size of this aperture is chosen such that it matches the dimensions of the effective exit pupil of the CGVH in order to reduce the magnitude of the zero order in the far-field. A motorized rotation and two linear stages are used to precisely position the CGVH along the optical axis.

6.2.2. Diffraction Efficiency and Bragg Selectivity of the CGVHs

For the angular multiplexing approach adopted in this work, if the reference waves meant to decouple single far-field projections are appropriately spaced, then the scattered wave U_s contains significant reconstruction from the i-th projection Ψ_i only. The remaining holograms are Bragg mismatched, i.e. they are read out by the incident beam, but their reconstructions, when integrated over the entire volume of the material, cancel out to zero as it has been shown for optically recorded volume holograms [114]. However, unlike in the case of such holograms the CGVHs proposed here
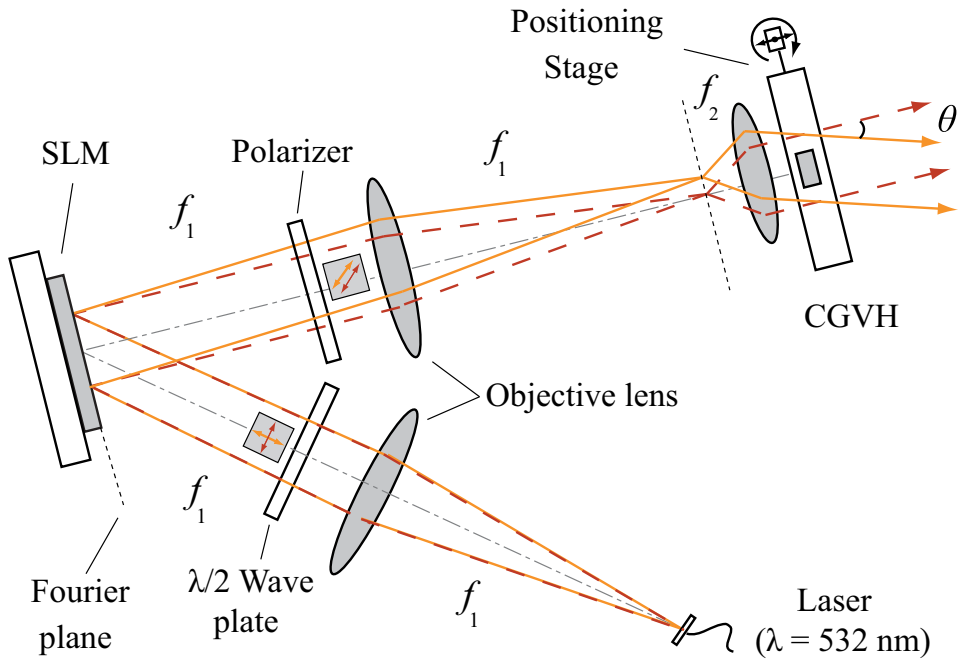
Figure 6.3.: Experimental setup which comprises in a 4f-setup consisting of a fiber coupled diode laser, 2 objective lenses with a focal length of $f_1 = 105$ mm, a $\lambda/2$ wave plate and a polarizer P. This part is used to implement a non-mechanical beam modulation unit with the help of an SLM. The other part, high precision positioning stages are used to position the CGVH and a lens, is used to collimate and couple in a single or a set of reference waves at different angles θ into the CGVH. For instance light that is polarized along the slow axis (*dashed line*) of the SLM can be modulated to generate a given reference wave, while light polarized along the fast axis (*solid line*) represents a second reference wave.

are designed to possess an optimal Bragg selectivity. This is mainly due to the fact that during the nonlinear based fabrication approach, only single voxels are addressed, unlike in the optical case where both the signal and reference beams illuminate the whole volume for each hologram.

The model developed in this thesis was thus first experimentally characterized by investigating the Bragg selectivity properties of the CGVHs shown. Since the CGVHs realized in this work have finite thickness, we expect them to show similar Bragg detuning characteristics as those of the VPHs discussed in Sect. 3.3. We thus expect that the size of the CGVH will effectively impart a multiplicative rect function, which then translates to a convolution of all far-field components with a sinc function:

$$\text{rect}\left(\frac{z}{L}\right) S(\boldsymbol{r}, \omega) \xrightarrow{\mathcal{F}} \frac{L}{\pi} \text{sinc}\left(\frac{L}{2}k_z\right) \otimes \tilde{S}(\boldsymbol{K}, \omega). \tag{6.5}$$

This becomes clear if we consider that we have a finite sized CGVH with a scattering potential which has the general form of

$$S(\boldsymbol{r}) = S(\boldsymbol{r}) \cdot \text{rect}\left[\frac{x}{L_x}, \frac{y}{L_y}, \frac{z}{L_z}\right], \tag{6.6}$$

where (L_x, L_y) determine the lateral extensions and L_z the thickness of the medium. From Eq. (3.15) and by applying the convolution theorem we can compute the scattering amplitude

$$\tilde{S}(\boldsymbol{K}, \omega) = \tilde{S}(\boldsymbol{K}, \omega) \otimes L_x L_y L_z \text{sinc}\left[\frac{L_x k_x}{2\pi}, \frac{L_y k_y}{2\pi}, \frac{L_z k_z}{2\pi}\right]. \tag{6.7}$$

Thus we arrive at a scattering amplitude that is convolved with a *sinc* function whose width is scaled by a positive-valued scale factor $b = L_i/2\pi$ along the $i-$th direction. Note that from Eqs. (5.24) and (6.7), changing the angle of incidence for instance in the y-direction leads to a deviation in the reciprocal space scattering vector which can be written as $k_y = (2\pi/\lambda)\sin(\theta + \Delta\theta)\sin(\alpha)$.

The result of this convolution is a blurring of the far-field projection around the Bragg angle θ_B as it's apparent from Fig. 6.4 *(a)*. Here, the Bragg detuning effect is shown in terms of the relative diffraction efficiency as a function of the sum of Bragg angle and a certain deflection $\Delta\theta$. It is clear that this results in sinc$^2-$shaped diffraction efficiency functions of every far field projection. These results also show a very good agreement between the theoretical case predicted by Eq. (6.7) and the experimentally measured data since the efficiency of reconstruction decreases as the angle of the reference wave deviates from the Bragg angle θ_B. The width of this *sinc* envelope can be interpreted as to represent the full width at half maximum (FWHM) of the system. Therefore, to minimize cross-talk, a certain $\Delta\theta_{fwhm}$ has to be achieved.

Since the angular multiplexing approach investigated in this work utilizes a discrete, angularly distinct set of plane waves as reference beams for decoding the CGVHs, the angular selectivity of the holograms plays a very important role. The Bragg selectivity thus directly limits the number of far field projections, i.e. the number of holograms,
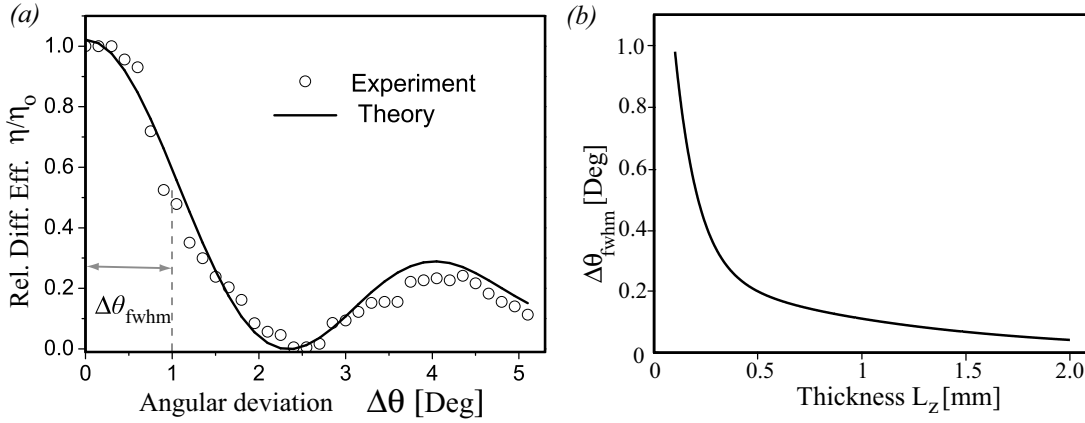
Figure 6.4.: *(a)* Bragg selectivity property of a CGVH, which is shown in terms of the relative diffraction efficiency η/η_o. The width of this sinc^2 envelope can be interpreted as to represent the full width at half maximum (FWHM) of the system - after Kamau *et. al.* [17]. *(b)* Angular Bragg selectivity of a CGVH, which projects an elementary circularly symmetrical Gaussian intensity distribution - c.f Sect 5.2.4., in terms of the $\Delta\theta_{fwhm}$ as a function of the holograms thickness.

that can be encoded in a single CGVH. To evaluate the impact of the thickness on the Bragg selectivity of the CGVHs proposed here, a far field projection of a circularly symmetrical Gaussian intensity distribution (c.f Sect 5.2.4) was investigated numerically for different values of L_z - see Fig. 6.4 *(b)*. For such an elementary far field projection, Bragg selectivity values on the order of $\Delta\theta_{fwhm} = 0.6°$ can be attained from a CGVH with a thickness of $L_z = 0.25$ mm. In the course of this work, a multiplexed CGVH having Bragg selectivity which has values of $\Delta\theta_{fwhm} \leq 1°$ was also investigated experimentally as it is discussed in the next section.

6.3. Dynamic Wave Field Synthesis: Angular Multiplexing and Superposition of Complex Fields

In the next step a CGVH with dimensions of $683 \times 683 \times 200 \ \mu\text{m}^3$, i.e. with a higher SBWP, was designed and fabricated using the parameters discussed above. The optical setup in Sect. 6.2.1 was then used to investigate multiplexing capabilities of this CGVH, which was designed to project far-field target intensities of the initials **bias** (see Fig. 6.5 *(a)-(d)*). Each projection was offset by an angle step of 2° degrees from each other. Figure 6.5 *(e) - (h)* shows results whereby the feasibility of cross-talk free decoding of these four far-field projections ψ_i from a single CGVH have been demonstrated. The far-field intensities of all four projections could clearly be decoded without detectable cross-talk.

In a further proof of principle study, a CGVH for the target intensities in Fig. 6.5 *(a - d)* was used to assess the feasibility of dynamic wave field synthesis. In an initial test, the birefringence property of the SLM was used. In Fig. 6.6 *(b)* the projection ψ_2 corresponding to a single reference wave that was generated using light of a single polarization is shown.
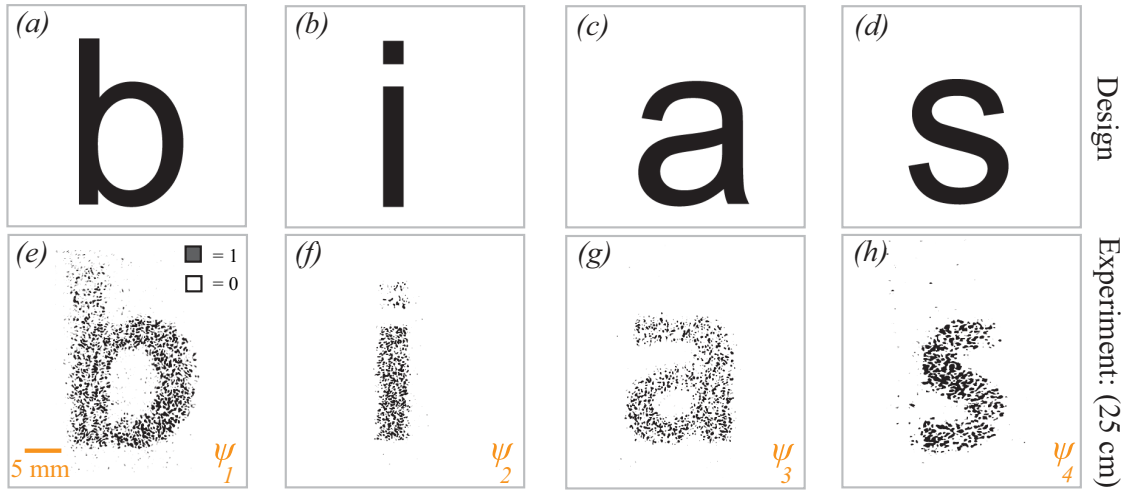
Figure 6.5.: Comparison between target intensities *(a) - (d)* and the four far-field projections *(e) - (h)*, which were were decoded experimentally from a single CGVH for four different angles. Each projection ψ_i was offset by an angle step of 2° from each other - after Kamau *et. al.* [17].

Alternatively, using the concept described in Sect. 5.3.2 above, a deflected reference wave $\boldsymbol{k}_\theta$ can be generated so that the projection ψ_3 is decoded as shown in Fig. 6.6 *(c)*. If however orthogonally polarized light is chosen, then the SLM can be used to generate two reference waves with k-vectors $\boldsymbol{k}_o$ and $\boldsymbol{k}_\theta$ concurrently. Two such reference waves can be coupled simultaneously into the CGVH thereby decoding two different far-field

projections and thus enabling synthesis of wave fields with a higher SBWP within the signal window W as shown in Fig. 6.6 *(d)*. By comparing these two images, this superposition is quite apparent since two projections are decoupled simultaneously and are superposed leading to the synthesis of a new wave field $\psi_2 + \psi_3$.
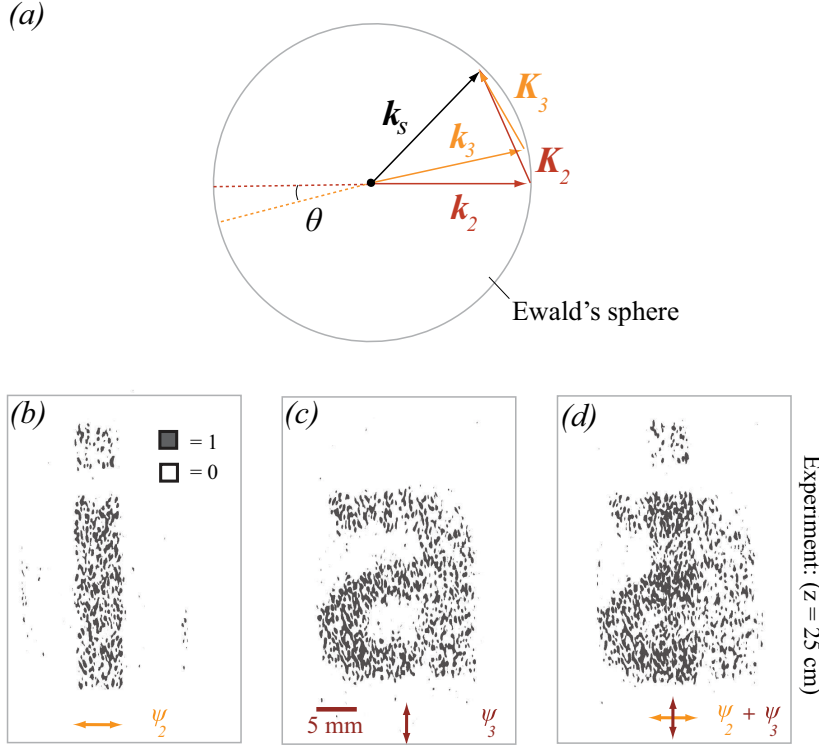

Figure 6.6.: *(a) Vectorial representation of the reconstruction process, whereby the same signal window W for two projections is chosen and hence both reference waves $\boldsymbol{k}_2$ and $\boldsymbol{K}_2$ have the same scattering vector $\boldsymbol{k}_s$. This leads to the superposition of ψ_2 and ψ_3 even though the corresponding reference waves are offset by an angle θ. (b) a single projection ψ_2 corresponding to a single reference wave, which is decoupled by light polarized in the fast axis. In (c) a second projection ψ_3 corresponding to a single reference wave is decoupled by light polarized in the slow axis and modulated using the SLM in order to generate a deflected reference wave $\boldsymbol{k}_\theta$. In(d) projections ψ_2 and ψ_3 are decoupled simultaneously and are superposed leading to the synthesis of a new wave field $\psi_2 + \psi_3$ - after Kamau et. al. [17].*

In a similar manner, by employing the SLM as an electronic diffraction grating several diffraction orders which depend on the shape of the grating can be generated thus facilitating a simultaneous superposition of N far-field projections in a given signal window W. This generation of several projections from a single CGVH was discussed in details in our previous work [47]. Note that if for N-reference waves the same signal window W is chosen (see Fig. 3.1(a)), the resulting CGVH contains N-holograms each having a grating vector $\boldsymbol{K}_n$. Consequently, according to Eq. (3.16)

these holograms have the same scattering vector $\boldsymbol{k}_s$. Such a vectorial representation of the scattering process for the results attained in this work is shown in Fig. 6.6 (a). This representation shows how the superposition of ψ_2 and ψ_3 is achieved even though the corresponding reference waves are offset by an angle θ.

The information capacity of a CGVH having refractive index values that are constrained to C discreet levels can be expressed in terms of the degrees of freedom of the feasible field distribution that it can synthesize. To do this let us start by first considering a wave field scattered within the CGVH to represent a 3D analytic function $U_s(\boldsymbol{r}', \omega)$ with a compact support in a give region. Suppose that this function is sampled in a uniform manner in the (x, y, z)-directions, which is indicated by

$$U_s(x, y, z, \omega) \rightarrow U_s(m\Delta x, n\Delta y, p\Delta z, \omega) \tag{6.8}$$

where the sample intervals are $(\Delta x, \Delta y, \Delta z)$ in the $x-$, $y-$ and $z-$directions respectively and (m, n, p) are integer valued indices of the samples. Now let us assume that this sampling is done in accord with the sampling theory, i.e. with spacings

$$\Delta x \leq 1/2B_x$$
$$\Delta y \leq 1/2B_y$$
$$\Delta z \leq 1/2B_z, \tag{6.9}$$

where B_i is the bandwidth of U_s in the $i-$th direction. The total number of significant samples required to represent U_s can be expressed in terms of the SBWP as follows

$$SBWP = \frac{C}{8} \left[L_x L_y L_z B_x B_y B_z \right]. \tag{6.10}$$

From Eqs. (6.9) and (6.10) it is clear that the results in Fig. 6.5 (b) were obtained from an SLM-CGVH hybrid system with an SBWP = 5.4×10^8 for each projection ψ_i. Hereby, we consider the fact that 5 holograms were encoded in one CGVH, each with discreet levels of quantization of $C = 2$, voxel sizes of ($\Delta x = 2.6\,\mu$m, $\Delta y = 2.6\,\mu$m, $\Delta z = 4\,\mu$m) and a hologram size of ($L_x = 683\,\mu$m, $L_y = 683\,\mu$m, $L_z = 200\,\mu$m). Thus owing to the excellent Bragg selectivity properties of the CGVH, the total SBWP of this system is SBWP = 2.2×10^9. This is 3 orders of magnitude higher than the current state of the art in multiplexed cascaded CGH systems [50], where a system with SBWP = 2.6×10^6 was demonstrated. In this case, 2 holograms were encoded in a system of CGHs, each with discreet levels of quantization $C = 64$, pixel sizes of ($\Delta x = 5\,\mu$m, $\Delta y = 5\,\mu$m, $\Delta z = 0.3\,$mm) and a hologram size of ($L_x = 320\,\mu$m, $L_y = 320\,\mu$m, $L_z = 1.5\,$mm).

Moreover, since our system allows for a simultaneous coupling of a set of reference waves, the achievable signal SBWP is much larger than that of a single CGVH. For instance, a hybrid system having a total in-coupling angle of $20°$ in both the xy-directions and a CGVH with a size of ($L_x = 683\,\mu$m, $L_y = 683\,\mu$m, $L_z = 200\,\mu$m) can have an SBWP on the order of $1.1\times = 10^{10}$. Hereby we have assumed that each of these holograms has an SBWP = 5.4×10^8 and that single projections are offset at an angle of $1°$. Hence we can conclude that our approach facilitates a tremendous increase in the achievable SBWP.

7. Summary and Outlook

7.1. Summary

The capability of an optical system to generate arbitrary optical fields is mainly limited by the number of degrees of freedom of the applied optical element or set of optical elements. One physical quantity that can be utilized to characterize the capability of such systems in capturing, transferring and/or processing optical information is their space-bandwidth product. The SBWP of conventional holographic optical elements, such as computer generated holograms, is for instance known to be quite limited. This can be attributed primarily to a limitation in the number of controllable elements (e.g. pixels), their limited lateral extent and their inherent two dimensional nature. The goal of this thesis was therefore to develop and investigate a novel method of designing volume holographic optical elements that allow for the generation of optical fields with a large signal SBWP. This work is based on the hypothesis that such volume holographic optical elements can in general be applied to generate a set of arbitrary orthogonal elementary waves, which can in turn be coherently superposed in order to attain an optical field with a desirably large signal SBWP.

The motivation behind this goal is to design and optimize a system that facilitates dynamic synthesis of predefined wave fields. Specifically, this work focuses on a novel hybrid system comprising in an SLM as a dynamic element and a CGVH as a multiplexed static element. It begins with an explicit definition of the problem at hand. Thereby, a problem where a scalar field is scattered by a weakly scattering but inhomogeneous dielectric holographic medium that is located in a bounded domain is considered. Hereby, the scattering process within the bulk of the CGVH is modeled with an inhomogeneous wave equation. This problem is formulated as an inverse problem of finding the scattering potential of a desired volume holographic optical element, for a given set of impinging reference waves and physical constraints. It is shown that due to various physical limitations inherent to this problem a closed form solution does not exist.

The proposed solution is based on the Rytov approximation of the scattered field, which is essentially a weak potential approximation. To attain this solution, the integral form of the inverse scattering problem is derived from the inhomogeneous wave equation within the accuracy of first order perturbation theory. The resulting model is then applied to develop a Fourier transform based iterative algorithm for numerically computing the scattered field for a given set of desired far field projections. Thereby, fundamental limits of this approach and the corresponding physical constraints are investigated.

It is shown in this work that most of these constraints arise from the fact that the wave fields that are modeled must fulfill the wave equation as well as a set of sampling conditions. For instance, an optical nonlinear absorption process is applied here to fabricate the proposed holograms. One major fabrication constraint that follows from this is the limitation of the sampling distances which correspond to the point spread function of the femtosecond laser lithographic system. Similarly, the Bragg condition is utilized to facilitate the design of crosstalk free multiplexed CGVHs. To achieve this, the magnitudes of the Fourier transform on the Ewald's sphere are determined for each desired projection. Hereby, the following constraints were enforced: the amplitude of the scattered field for each projection must be non-negative, continuous, and bounded within a compact support. It is shown that in order to enforce continuity of the wave field within the support, a cubic filter has to be applied within the design algorithm.

This thesis thus essentially presents a novel approach that is based on the first order Rytov approximation of the field scattered from a voxelated volume hologram. It is shown in this work that through this approach functional multiplexed CGVHs with a refractive index contrast within the range of $\delta_n \approx 10^{-4} \cdots 10^{-2}$ can be computed. These values are one order of magnitude higher than the ones achievable in the current state of the art. This shows the flexibility of this design approach in terms of the feasible range in achievable δ_n values and hologram thickness. As a result, this approach allows for the determination of the discrete scattering potential of larger holograms as compared to the conventional approach that is based on the first Born approximation. In turn, this increase in thickness leads to an increased space-bandwidth product. The possibilities presented by the proposed approach were investigated by assessing the applicability of such holograms in the field of dynamic wave field synthesis.

In an initial step, in order to explore theoretically the feasibility of the proposed design approach, a set of holograms with a known response are computed - see chapter 5. These CGVHs are analyzed numerically by characterizing their performance in terms of diffraction efficiency, Bragg selectivity and the SNR of the synthesized far-field projections. It is shown here that as the thickness of the hologram increases, our proposed approach is seen to compute holograms with better SNR. For instance, for a hologram with a thickness of $L_z = 288 \ \mu$m the SNR within the signal window is seen to increase from 0 to 6 dB within the first 25 iterations, whereas the conventional approach is seen to fail. Furthermore, it is shown that CGVHs with a diffraction efficiency of $\eta = 12\%$ can be designed using this approach. Additionally, to assess the experimental feasibility of fabricating these holograms and of wave field synthesis using the proposed hybrid system, the characterization of various holograms is discussed in chapter 6. The results of DIC microscopy are for instance presented. These results clearly demonstrate for the first time that CGVHs with smooth internal contours and smaller voxel dimensions ($\Delta x = \Delta y = 1 \ \mu$m) than in the current state of the art ($\Delta x = \Delta y = 2 \ \mu$m) can be fabricated in a photosensitive glass by nonlinear laser induced 3D modification of refractive index.

The optical functionality of the fabricated CGVHs is characterized in terms of their multiplexing properties and the signal SBWP of the synthesized optical fields. It is shown herein that a set of wave fields can be decoupled sequentially or simultaneously

from a CGVH with an SBWP $= 5.4 \times 10^8$ for each far field projection. Furthermore, it is shown that a Bragg selectivity value of $\Delta\theta_{fwhm} = 1°$ is achievable. These results allow for the proposed dynamic wave field synthesis using an electronically addressed spatial light modulator as it is demonstrated here. In conclusion, this thesis clearly demonstrates that a set of arbitrary orthogonal elementary waves can in principle be encoded in a single CGVH. These can then be decoded and coherently superposed in order to generate an optical field having a large signal space-bandwidth product, i.e. SBWP $\geq 1.1 \times 10^{10}$.

7.2. Suggestions for Future Work

One significant next step for the work presented in this thesis would be to investigate a method that facilitates the computation of an even more efficient HOE based hybrid system. In the following, a set of ideas for the future work are outlined:

- For instance, a model based on higher order terms of the Rytov series could be incorporated to the current model. This extension can be used to obtain a very good approximation of the scattered field if more and more terms of the series are included in the calculation. This extension is straightforward since each term is obtained from the preceding one by means of the recurrence relation.

- Another significant next step could be a detailed analysis on the feasibility of encoding fundamental functions in the CGVH. Such signals could then be decoded and superposed thereby generating even more complex field distributions. The capability of such a volumetric spatial light modulator would open up more possibilities in the field of wave field synthesis.

- It is important to note that one of the major bottlenecks of the laser lithography based approach, which was used for the fabrication of CGVHs, is the voxel to voxel serial writing. This leads to a technical limitation on the feasible number of discreet quantization levels to binary levels of $C = 2$ and to the size of holograms that can be inscribed in a given period of time. An approach that allows for a parallel exposure of a set of voxels in a single step is required.

A. Derivations

This appendix provides details of lengthy and important derivations referred to throughout the text for reference purposes.

A.1. Inhomogeneous Wave Equation

In order to derive the *inhomogeneous wave equation* in Eq. (2.33) from the Maxwell's equations in Eqs. (2.1) - (2.4), we start by applying the curl operation $\nabla\times$ to both sides of Eq. (2.4), using Eq. (2.3) and noting that $\epsilon = \epsilon(\boldsymbol{r})$ in order to arrive at

$$-\nabla \times (\nabla \times \boldsymbol{\mathcal{E}}) = \nabla(\nabla \cdot \boldsymbol{\mathcal{E}}) - \nabla^2 \boldsymbol{\mathcal{E}} = -\mu_o \frac{\partial^2 \boldsymbol{\mathcal{B}}}{\partial t^2}. \tag{A.1}$$

Now with the help of Eqs. (2.3) and (2.21) and the identity $\nabla \cdot \epsilon \boldsymbol{\mathcal{E}} = \epsilon \nabla \cdot \boldsymbol{\mathcal{E}} + \nabla \epsilon \cdot \boldsymbol{\mathcal{E}}$, we arrive at the inhomogeneous wave equation [63]

$$\nabla^2 \boldsymbol{\mathcal{E}} + \nabla \left(\frac{1}{\epsilon} \nabla \epsilon \cdot \boldsymbol{\mathcal{E}} \right) - \frac{1}{c^2(\boldsymbol{r})} \frac{\partial^2 \boldsymbol{\mathcal{E}}}{\partial t^2} = 0. \tag{A.2}$$

which, by noting that $c(\boldsymbol{r}) = c_o/n(\boldsymbol{r})$, can be rewritten to arrive at the inhomogeneous wave equation Eq. (2.33).

A.2. Nonlinear Wave Equation

Again from the Maxwell's equations given by Eqs. (2.1) - (2.4) we start by taking the curl of Eq. (2.4) to arrive at

$$\nabla \times (\nabla \times \boldsymbol{\mathcal{E}}) = -\frac{\partial(\nabla \times \boldsymbol{\mathcal{B}})}{\partial t} \tag{A.3}$$

By considering the definition in Eq. (2.24) and with the help of Eq. (2.3), we can rewrite Eq. (A.3) as

$$\nabla \times (\nabla \times \boldsymbol{\mathcal{E}}) = -\mu \frac{\partial^2 \boldsymbol{\mathcal{D}}}{\partial t^2}. \tag{A.4}$$

Here we can use the vector identity in Eq. (2.34) and Eq. (2.1) to arrive at

$$-\nabla^2 \boldsymbol{\mathcal{E}} = -\mu \frac{\partial^2 \boldsymbol{\mathcal{D}}}{\partial t^2}. \tag{A.5}$$

Finally, recalling the definition of the electric flux density in Eq. (2.5) we get

$$-\nabla^2\boldsymbol{\mathcal{E}} = -\mu_o\epsilon_o\frac{\partial^2\boldsymbol{\mathcal{E}}}{\partial t^2} - \mu\frac{\partial^2\boldsymbol{\mathcal{P}}}{\partial t^2}. \tag{A.6}$$

From Eq. (2.39) we can write the polarization $\boldsymbol{\mathcal{P}}$ as a sum of a linear part $\boldsymbol{\mathcal{P}}^{(1)}$ and higher order contributions $\boldsymbol{\mathcal{P}}^{(N)}$. Thus, Eq. (A.6) can be rewritten to arrive at the nonlinear wave equation

$$\nabla^2\boldsymbol{\mathcal{E}} - \mu_o\epsilon_o\frac{\partial^2\boldsymbol{\mathcal{E}}}{\partial t^2} = \mu_o\frac{\partial^2\boldsymbol{\mathcal{P}}^{(N)}}{\partial t^2}, \tag{A.7}$$

which was given in Eq. (2.38). Here, we have changed μ to μ_o since the materials we consider in this work are assumed to be nonmagnetic.

A.3. Inhomogeneous Wave Equation for the Rytov Approximation

The Rytov approximation is derived by considering the total field to be represented as a complex phase of the form of

$$U(\boldsymbol{r},\omega) = \exp\left[\Phi(\boldsymbol{r},\omega)\right]. \tag{A.8}$$

This scalar wave satisfies the wave equation so that after inserting it into the wave equation in Eq. (3.3) we obtain (the arguments $(\boldsymbol{r},\omega)$ are omitted here to simplify notation)

$$\nabla^2\mathrm{e}^\Phi + k_o^2\mathrm{e}^\Phi = -4\pi S\mathrm{e}^\Phi \tag{A.9}$$

$$\nabla\left[\nabla\Phi\mathrm{e}^\Phi\right] + k_o^2\mathrm{e}^\Phi = -4\pi S\mathrm{e}^\Phi \tag{A.10}$$

$$\nabla^2\Phi\mathrm{e}^\Phi + \left(\nabla\Phi\right)^2\mathrm{e}^\Phi + k_o^2\mathrm{e}^\Phi = -4\pi S\mathrm{e}^\Phi, \tag{A.11}$$

and finally

$$\nabla^2\Phi(\boldsymbol{r},\omega) + \left[\nabla\Phi(\boldsymbol{r},\omega)\right]^2 = -4\pi S(\boldsymbol{r},\omega) \tag{A.12}$$

A.4. Perturbation Expansion of the Rytov Approximation

Hereby, $S(\boldsymbol{r},\omega)$ is the scattering potential in Eq. (3.4). By expressing the total complex phase Φ as a sum of the incident phase function Φ_o and scattered phase Φ_s as given by Eq. (5.1) and inserting Eq. (3.4) into Eq. (A.12) we arrive at the following nonlinear equation for $\Phi_s(\boldsymbol{r},\omega)$ [98, 101]

$$\nabla^2\Phi_s(\boldsymbol{r},\omega) + \nabla\Phi_s(\boldsymbol{r},\omega)\cdot\left[2\nabla\Phi_o(\boldsymbol{r},\omega) + \Phi_s(\boldsymbol{r},\omega)\right]^2 +$$
$$2k_o^2\delta_n n_o(\boldsymbol{r},\omega)n_1(\boldsymbol{r},\omega) + k_o^2\delta_n^2 n_1^2(\boldsymbol{r},\omega) = 0 \tag{A.13}$$

Now let us consider a solution to this problem by assuming that the following power series can be used to represent $\Phi_s(\boldsymbol{r}, \omega)$ as an asymptotic expansion in powers of the small perturbation parameter γ:

$$\Phi_s(\boldsymbol{r}, \omega) = \sum_{i=0}^{\infty} \gamma^i \Phi_{s,i}(\boldsymbol{r}, \omega). \tag{A.14}$$

After substituting (A.14) into (A.13) and equating the groups of terms containing equal powers of the perturbation parameter γ, we arrive at the following recurrence relations [74, 101]

$$(\nabla^2 \Phi_o(\boldsymbol{r}, \omega)) + (\nabla \Phi_o(\boldsymbol{r}, \omega))^2 = -2k_o^2 n_o n_1(\boldsymbol{r}, \omega) \tag{A.15}$$

$$\nabla^2 \Phi_1(\boldsymbol{r}, \omega) + 2\nabla \Phi_o(\boldsymbol{r}, \omega) \cdot \nabla \Phi_1(\boldsymbol{r}, \omega) = -2k_o^2 n_1^2(\boldsymbol{r}, \omega) - \nabla \Phi_o(\boldsymbol{r}, \omega) \cdot \nabla \Phi_1(\boldsymbol{r}, \omega) \tag{A.16}$$

$$\cdots$$

$$\nabla^2 \Phi_m(\boldsymbol{r}, \omega) + 2\nabla \Phi_o(\boldsymbol{r}, \omega) \cdot \nabla \Phi_m(\boldsymbol{r}, \omega) = -\sum_{i=1}^{m-1} \nabla \Phi_n(\boldsymbol{r}, \omega) \cdot \nabla \Phi_{m-i}(\boldsymbol{r}, \omega), m \geq 2. \tag{A.17}$$

Note that Eq. (A.15) is independent of the medium and thus gives a solution to Eq. (3.1) (i.e. $(\nabla^2 + k(\boldsymbol{r}, \omega)^2)U_o(\boldsymbol{r}, \omega) = 0$) - for the case where $n_1(\boldsymbol{r}) = 0$ and

$$U_o(\boldsymbol{r}, \omega) = \exp\left[\Phi_o(\boldsymbol{r}, \omega)\right]. \tag{A.18}$$

On the other hand, Eq. (A.16) which has the term $\Phi_1(\boldsymbol{r}, \omega)$ is linear in $S(\boldsymbol{r}, \omega)$ and the term $\Phi_2(\boldsymbol{r}, \omega)$ in Eq. (A.17) is quadratic in $S(\boldsymbol{r}, \omega)$ and so on. In literature these terms, $\Phi_1(\boldsymbol{r}, \omega)$ and $\Phi_2(\boldsymbol{r}, \omega)$ is usually referred to as the first and second order Rytov approximation respectively. Equation (A.17) can therefore be used to obtain a very good approximation of the scattered field if more and more terms of the series are included in the calculation. Hereby, as it was mentioned in Sect. (4.1) each term is obtained from the preceding one by means of the recurrence relation [115, 116]. This means that once a numerical model, which is based on the first order Rytov approximation is derived, extension of this model to include further terms is straightforward.

B. Modeling of Light Propagation in Scattering Inhomogeneous Holographic Media

With the aim of numerically analyzing light propagation in computer generated volume holograms, two methods were applied in this thesis. The first one is the rigorous coupled wave theory which was originally proposed by Kogelnik with the purpose of analyzing volume holographic gratings [52]. The second method is a numerical computational technique, which is widely applied for the general analysis and simulation of guided wave propagation in inhomogeneous media.

B.1. Fourier Based Beam Propagation Method

To predict the performance of the computed CGVHs and also gain additional insight on their functionality prior to their fabrication, routines for a Fourier based beam propagation method (FFT-BPM) were implemented. The BPM method is a computational technique in optics, which is used to numerically solve the wave equation. It is one of the most widely applied methods for the analysis and simulation of guided wave propagation in inhomogeneous media. It was first introduced by Feit and Fleck in the late 1970s [104]. It is an approximation technique for simulating the propagation of light in a medium slowly varying envelope approximation. Since a different approach (slice-by-slice computation) to the propagation of light is taken in this method, as compared to the perturbation theory based design approach described in this thesis, it can be used to validate such models.

Beam propagation method is based on the solution of the Helmholtz equation in the paraxial approximation for monochromatic waves [117]. Thus in the conventional BPM plane wave decomposition is used to represent a propagating wave field propagating in an inhomogeneous medium as a superposition of plane waves. Wave propagation is thereby modeled as an integral of these plane waves in the spectral domain and effects resulting from the inhomogeneity are accounted for as a phase correction in the space domain [118]. From Eqs. (2.29), (3.2) and (3.6) we can write the Helmholtz equation as follows

$$\frac{\partial^2 U}{\partial x^2} + \frac{\partial^2 U}{\partial y^2} + k_o^2 \left[n(x,y,z)^2 - n_o^2 \right] U = -2\mathrm{i}k_o n_o \frac{\partial U}{\partial z^2}. \tag{B.1}$$

From this equation we then derive the operator form of the FFT-BPM method [119–

121] which was implemented in the course of this work:

$$U(x, y; z + \Delta z) = \exp(S\Delta z) \cdot \mathcal{F}^{-1}\left\{D \cdot \mathcal{F}\left\{U(x, y; z)\right\}\right\}. \tag{B.2}$$

Here, $D = \exp\left[\mathrm{i}\left(f_x^2 + f_y^2\right)\Delta z/2k\right]$ and $S = -\mathrm{i}\Delta n(x, y; z)k$ are the diffraction and the nonlinear operators respectively, (x, y, z) are coordinates in the spatial domain, (f_x, f_y) the corresponding spatial frequencies and Δz propagation steps along the z-direction.

Please note that there are some limitations in the applicability of the conventional BPM method since in its the derivation a paraxial approximation is assumed. Furthermore it is assumed that there are no large refractive index discontinuities in the medium [118]. In cases where these assumptions are not valid, the accuracy and flexibility of this method can be improved by using extended methods like finite-difference based BPM schemes (FD-BPM) and finite-element BPM (FE-BPM) [121]. However, for a more accurate analytical solution rigorous coupled wave theory is adopted.

B.2. Rigorous Coupled Wave Theory

Historically, rigorous analysis of volume holograms has always been done by means of coupled wave theory (CWA). In its original formulation, CWA was derived from the Maxwell's equations by assuming that the total field propagating through a holographic volume grating can be expressed in terms of a reference wave $R(\boldsymbol{r})$ and a scattered wave $O(\boldsymbol{r})$ [52]. Later on, it could be shown that a *rigorous* coupled wave theory (RCWA) can be formulated as an exact solution of the Maxwell's equations without approximation [122]. The accuracy of this solution depends solely on the number of retained terms in the space-harmonic expansion of the fields propagating through the medium. In the following we will discuss the derivation of the fundamental equations that can be used to calculate observables such as the diffraction efficiency and angular selectivity of volume holograms.

Let us start by considering the periodic volume phase hologram that is schematically depicted in Fig. 3.2 *(a)*. When such a VPH is illuminated with a reference plane wave

$$U_r = A_r(z)\exp(-\mathrm{i}\boldsymbol{\rho}\cdot\boldsymbol{r}), \tag{B.3}$$

in the direction $\boldsymbol{\rho}$ at the Bragg-matched angle θ_o a plane wave

$$U_s = A_s(z)\exp(-\mathrm{i}\boldsymbol{\sigma}\cdot\boldsymbol{r}) \tag{B.4}$$

is reconstructed in the direction $\boldsymbol{\sigma}$. These two fields are described by the amplitudes $A_r(z)$ and $A_r(z)$, which vary along the $z-$direction. The propagation vectors $\boldsymbol{\rho}$ and $\boldsymbol{\sigma}$, which have a modulus of

$$\beta = \frac{2\pi n}{\lambda}, \tag{B.5}$$

contain information about the propagation constants and the direction of these fields. In analogy to (3.5), we assume hereby that the total field within the hologram is the

superposition of these two wave fields, i.e. $U = U_r + U_s$. Given this information, Kogelnik derived from the Maxwell's equations the following system of coupled differential equations that describe the energy interchange between these two fields [52]:

$$c_r \frac{\mathrm{d}U_r}{\mathrm{d}z} + \mathrm{i}\tilde{\kappa}U_s = 0 \tag{B.6}$$

$$c_s \frac{\mathrm{d}U_s}{\mathrm{d}z} + \mathrm{i}\vartheta U_s + \mathrm{i}\tilde{\kappa}U_r = 0, \tag{B.7}$$

where $\tilde{\kappa} = \pi n_1/\lambda$ is the coupling constant - see also Eq. (3.21), $\vartheta = (\beta^{-2} - n_1^2)/2\beta$ is the Bragg mismatch parameter and c_r and c_s are the cosines of the angles formed by the propagation vectors with respect to the normal of the grating.

For the loss-less transmission holograms presented in this thesis Eqs. (B.6) and (B.7) can be solved subject to the boundary conditions $A_r(0) = 1$ and $A_s(0) = 0$ in order to obtain the diffraction efficiency $\eta = |U_s|$ which can be written as follows [52]

$$\eta = \mathrm{sinc}^2\left(\sqrt{\chi_1^2 + \chi_2^2}\right), \tag{B.8}$$

whereby the parameters

$$\chi_1 = \frac{\pi n_1 L_z}{\lambda \cos(\theta_B)}, \tag{B.9}$$

and

$$\chi_2 = \Delta\theta \frac{\pi L_z}{\Lambda} \tag{B.10}$$

are related to the angular deviation $\Delta\theta$ from the Bragg angle and the thickness of the hologram.

For a volume hologram with a more complex non-periodic refractive index distribution, this approach can be adopted in form of rigorous coupled wave theory. Thereby, by eliminating the z-dependency of the refractive index distribution, it is possible to write the solution inside the hologram as a Fourier expansion, since only a dependency on the coordinate x and y is present [122, 123]. In this work, a numerical implementation of RCWT was achieved by slicing up the CGVH such that inside each slice, the $n(\boldsymbol{r})$ only depends on x and y. At the boundaries between two slices, the tangential components of the electromagnetic fields are continuous. In this way, the unknown reflection and transmission coefficients of the upper and lower half-space can be connected to each other and determined.

C. List of my Publications

C.1. Peer Reviewed Journals

P1. **Kamau**, E. N.; Heine, J.; Falldorf, C. and Bergmann, R. B., Dynamic Wave Field Synthesis: Enabling Generation of Field Distributions with a Large Space-Bandwidth Product. *Opt. Express* **23** 28920 - 28934 (2015).

P2. **Kamau**, E. N., Burns, N. M., Falldorf, C., von Kopylow, C., Watson, J. and Bergmann, R. B. Least-squares based inverse reconstruction of in-line digital holograms. *J. Opt.* **15**, 075716 (2013).

C.2. Peer Reviewed Proceedings

P3. **Kamau**, E. N.; Parsi Sreenivas, V. V.; Bülters, M.; Falldorf, C. and Bergmann, R. B., *Fabrication of Multiplexed Computer Generated Volume Holograms in Photosensitive Glass*, in *Frontiers in Optics, OSA* (2014), FTh4G-1.

P4. **Kamau**, E. N.; Wang, N.; Falldorf, C. and von Kopylow, C., *Point Source Based Model for the Inverse Numerical Reconstruction of Digital Holograms*, in *EOS Annual Meeting, Aberdeen* (2012), ISBN 978-3-9815022-4-4.

C.3. Proceedings

P5. **Kamau**, E. N.; Falldorf, C.; and Bergmann, R. B., *A new approach to dynamic wave field synthesis using computer generated volume holograms*. In: 12-th Workshop on Information Optics - IEEE Xplore, 2013, pp. 1-3.

P6. Bülters, M.; **Kamau**, E. N.; Sanchez-Alvarez, C.; Parsi Sreenivas, V. V.; Falldorf, C. and Bergmann, R. B., *Three dimensional Modification of the Refractive Index in Photosensitive Foturan Glass*. In: 115. Jahrestagung der Deutschen Gesellschaft für angewandte Optik (DGaO 2014) (online)

P7. **Kamau**, E. N.; Falldorf, C.; and Bergmann, R. B., *Robust digital speckle photography based on Radon and Fourier-Mellin transforms*. In International Conference on Optical Instruments and Technology (OIT2011) (pp. 82020A-82020A), SPIE (2011).

C.4. Conference Talks

P8. **Kamau**, E. N.; Parsi Sreenivas, V. V.; Bülters, M.; Falldorf, C. and Bergmann, R. B., *Fabrication of Multiplexed Computer Generated Volume Holograms in Photosensitive Glass*, Frontiers in Optics / Laser Science (Tuscon, AZ - USA 2014).

P9. **Kamau**, E. N.; Bülters, M.; Sanchez-Alvarez, C.; Parsi Sreenivas, V. V.; Falldorf, C. and Bergmann, R. B., *Fabrication of three dimensional DOEs in photosensitive Foturan Glass.* Nano Manufacturing Conference (Bremen - Germany 2014).

P10. Bülters, M.; **Kamau**, E. N.; Sanchez-Alvarez, C.; Parsi Sreenivas, V. V.; Falldorf, C. and Bergmann, R. B., *Three dimensional Modification of the Refractive Index in Photosensitive Foturan Glass.* 115. Jahrestagung der DGaO (Karlsruhe - Germany 2014).

P11. **Kamau**, E. N.; Falldorf, C.; and Bergmann, R. B., *A new approach to dynamic wave field synthesis using computer generated volume holograms.* 12-th Workshop on Information Optics - IEEE Xplore, (Tenerife, Spain 2013).

P12. **Kamau**, E. N.; Wang, N.; Falldorf, C. and von Kopylow, C., *Point Source Based Model for the Inverse Numerical Reconstruction of Digital Holograms*, European Optical Society Annual Meeting (Aberdeen, UK 2012).

P13. **Kamau**, E. N.; Falldorf, C.; and Bergmann, R. B., *Robust digital speckle photography based on Radon and Fourier-Mellin transforms.* In International Conference on Optical Instruments and Technology, SPIE (Beijing, China 2011).

Bibliography

1. Winick, K. & Fienup, J. Optimum holographic elements recorded with non-spherical wave fronts. *J. Opt. Soc. Am. A* **73,** 208–217 (1983).

2. Goodman, J. W. *Introduction to Fourier optics* (Roberts & Company Publishers, 2005).

3. Gabor, D. A new microscopic principle. *Nature* **161,** 777–778 (1948).

4. Langehanenberg, P., von Bally, G. & Kemper, B. Autofocusing in digital holographic microscopy. *3D Research* **2,** 1–11 (2011).

5. Leith, E., Kozma, A, Upatnieks, J, Marks, J & Massey, N. Holographic data storage in three-dimensional media. *Appl. Opt.* **5,** 1303–1311 (1966).

6. Curtis, K., Dhar, L., Hill, A., Wilson, W. & Ayres, M. *Holographic data storage* (Wiley Online Library, 2010).

7. McElhinney, C. P., Hennelly, B. M. & Naughton, T. J. Extended focused imaging for digital holograms of macroscopic three-dimensional objects. *Appl. Opt.* **47,** D71–D79 (2008).

8. Schnars, U., Falldorf, C., Watson, J. & Jüptner, W. *Digital Holography and Wavefront Sensing* (Springer, 2015).

9. Huferath-von Luepke, S, Kamau, E. N., Kreis, T. & von Kopylow, C. *Single-shot multiwavelength shape measurements with restricted aperture* in *Proc. SPIE* (2012), 84930V–84930V.

10. Von Kopylow, C. & Bergmann, R. B. in *Micro Metal Forming* (ed Vollertsen, F.) 392–404 (Springer, Berlin, 2013).

11. Kamau, E. N., Burns, N. M., Falldorf, C., von Kopylow, C., Watson, J. & Bergmann, R. B. Least-squares based inverse reconstruction of in-line digital holograms. *J. Opt.* **15,** 075716 (2013).

12. Osten, W., Faridian, A., Gao, P., Körner, K., Naik, D., Pedrini, G., Singh, A. K., Takeda, M. & Wilke, M. Recent advances in digital holography [Invited]. *App. Opt.* **53,** G44–G63 (2014).

13. Falldorf, C., Agour, M. & Bergmann, R. B. Digital holography and quantitative phase contrast imaging using computational shear interferometry. *Optical Engineering* **54,** 024110–024110 (2015).

14. Waters, J. P. Holographic image synthesis utilizing theoretical methods. *Appl. Phys. Lett.* **9,** 405–407 (1966).

15. Bryngdahl, O. & Wyrowski, F. Digital holography: computer-generated holograms. *Prog. Opt.* **28,** 1–86 (1990).

16. Piestun, R., Spektor, B. & Shamir, J. Wave fields in three dimensions: analysis and synthesis. *J. Opt. Soc. Am.* **13,** 1837–1848 (1996).

17. Kamau, E. N., Heine, J., Falldorf, C. & Bergmann, R. B. Dynamic wave field synthesis: enabling the generation of field distributions with a large space-bandwidth product. *Opt. Express* **23,** 28920–28934 (2015).

18. Schnars, U. & Jüptner, W. P. Digital recording and numerical reconstruction of holograms. *Measurement science and technology* **13,** R85 (2002).

19. Leith, E. N. & Upatnieks, J. Reconstructed wavefronts and communication theory. *J. Opt. Soc. Am.* **52,** 1123–1130 (1962).

20. Goodman, J. W. & Lawrence, R. W. Digital image formation from electronically detected holograms. *Appl. Phys. Lett.* **11,** 77–79 (1967).

21. Lohmann, A. W., Dorsch, R. G., Mendlovic, D., Zalevsky, Z. & Ferreira, C. Space-bandwidth product of optical signals and systems. *J. Opt. Soc. Am.* **13,** 470–473 (1996).

22. Schnars, U. & Jüpner, W. Direct recording of holograms by a CCD target and numerical reconstruction. *Appl. Opt..* **33,** 179–181 (1994).

23. Domínguez-Caballero, J. A. *Optimization of the holographic process for imaging and lithography* PhD thesis (Massachusetts Institute of Technology, Department of Mechanical Engineering, 2010).

24. Lohmann, A. W. & Paris, D. Binary Fraunhofer holograms, generated by computer. *Appl. Opt.* **6,** 1739–1748 (1967).

25. Lee, W.-H. Binary computer-generated holograms. *Appl. Opt.* **18,** 3661–3669 (1979).

26. Moreno, I. S., Gorecki, C., Rubio, J. C. C. & Yzuel, M. J. Comparison of computer-generated holograms produced by laser printers and lithography: application to pattern recognition. *Opt. Eng.* **34,** 3520–3525 (1995).

27. Xie, Y., Lu, Z. & Li, F. Lithographic fabrication of large curved hologram by laser writer. *Opt. Express* **12,** 1810–1814 (2004).

28. Baber, S. C. *Application of high resolution laser writers to computer generated holograms and binary diffractive optics,* in *Proc. SPIE* **1052** (1989), 66–76.

29. Arnold, S. M. Electron beam fabrication of computer-generated holograms. *Opt. Eng.* **24,** 245803–245803 (1985).

30. Peterhänsel, S., Pruss, C. & Osten, W. Phase errors in high line density CGH used for aspheric testing: beyond scalar approximation. *Opt. Express* **21,** 11638–11651 (2013).

31. Curtis, J. E., Koss, B. A. & Grier, D. G. Dynamic holographic optical tweezers. *Opt. Commun.* **207,** 169–175 (2002).

32. Falldorf, C., Dankwart, C., Gläbe, R., Lünemann, B., Kopylow, C. v. & Bergmann, R. B. Holographic projection based on diamond-turned diffractive optical elements. *Appl. Opt.* **48,** 5782–5785 (2009).

33. Dankwart, C., Falldorf, C. & Bergmann, R. B. *Design of diamond turned holograms for multiple wavelength image formation* in *Information Optics (WIO), 2013 12th Workshop on* (2013), 1–3.

34. Grosso, R. P. & Yellin, M. The membrane mirror as an adaptive optical element. *J. Opt. Soc. Am.* **67,** 399–406 (1977).

35. Zhu, L., Sun, P.-C., Bartsch, D.-U., Freeman, W. R. & Fainman, Y. Wavefront generation of Zernike polynomial modes with a micromachined membrane deformable mirror. *App. Opt.* **38,** 6019–6026 (1999).

36. Grinberg, J., Jacobson, A., Bleha, W., Miller, L., Fraas, L., Boswell, D. & Myer, G. A new real-time non-coherent to coherent light image converter the hybrid field effect liquid crystal light valve. *Opt. Eng.* **14,** 143217 (1975).

37. Mukohzaka, N., Yoshida, N., Toyoda, H., Kobayashi, Y. & Hara, T. Diffraction efficiency analysis of a parallel-aligned nematic-liquid-crystal spatial light modulator. *App. Opt.* **33,** 2804–2811 (1994).

38. Sampsell, J. B. Digital micromirror device and its application to projection displays. *J. Vac. Sci. Technol. B* **12,** 3242–3246 (1994).

39. Gruneisen, M. T., DeSandre, L. F., Rotge, J. R., Dymale, R. C. & Lubin, D. L. Programmable diffractive optics for wide-dynamic-range wavefront control using liquid-crystal spatial light modulators. *Opt. Eng.* **43,** 1387–1393 (2004).

40. Liang, M., Stehr, R. L. & Krause, A. W. Confocal pattern period in multiple-aperture confocal imaging systems with coherent illumination. *Opt. Lett.* **22,** 751–753 (1997).

41. Seifert, L, Tiziani, H. & Osten, W. Wavefront reconstruction with the adaptive Shack–Hartmann sensor. *Opt. Comm.* **245,** 255–269 (2005).

42. Falldorf, C., Agour, M., Bergmann, R. B., *et al.* Phase retrieval by means of a spatial light modulator in the Fourier domain of an imaging system. *Appl. Opt.* **49,** 1826–1830 (2010).

43. Falldorf, C., von Kopylow, C. & Bergmann, R. B. Wave field sensing by means of computational shear interferometry. *J. Opt. Soc. Am., A* **30,** 1905–1912 (2013).

44. Huang, P. S., Zhang, C. & Chiang, F.-P. High-speed 3-D shape measurement based on digital fringe projection. *Opt. Eng.* **42,** 163–168 (2003).

45. Zhang, S., Van Der Weide, D. & Oliver, J. Superfast phase-shifting method for 3-D shape measurement. *Opt. Express* **18,** 9684–9689 (2010).

46. Agour, M., Falldorf, C. & Bergmann, R. B. Investigation of composite materials using SLM-based phase retrieval. *Opt. Lett.* **38,** 2203–2205 (2013).

47. Kamau, E. N., Falldorf, C. & Bergmann, R. B. *A new approach to dynamic wave field synthesis using computer generated volume holograms,* in *12th Workshop on information Optics - IEEE* (2013), 1–3.

48. Buelters, M., Kamau, E. N., Sanchez-Alvarez, C., Parsi Sreenivas, V. V., Falldorf, C. & Bergmann, R. B. *Three dimensional Modification of the Refractive Index in Photosensitive Foturan Glass* in *115. Jahrestagung der Deutschen Gesellschaft fuer angewandte Optik (DGaO 2014) (online)* (2014).

49. Borgsmüller, S., Noehte, S., Dietrich, C., Kresse, T. & Männer, R. Computer-generated stratified diffractive optical elements. *Appl. Opt.* **42,** 5274–5283 (2003).

50. Gülses, A. A. & Jenkins, B. K. Cascaded diffractive optical elements for improved multiplane image reconstruction. *Appl. Opt.* **52,** 3608–3616 (2013).

51. Gerke, T. D. & Piestun, R. Aperiodic computer-generated volume holograms improve the performance of amplitude volume gratings. *Opt. Express* **15,** 14954–14960 (2007).

52. Kogelnik, H. Coupled wave theory for thick hologram gratings. *Bell System Technical Journal* **48,** 2909–2947 (1969).

53. Brady, D. & Psaltis, D. Control of volume holograms. *J. Opt. Soc. Am.* **9,** 1167–1182 (1992).

54. Case, S. K. & Dallas, W. Volume holograms constructed from computer-generated masks. *App. Opt.* **17,** 2537–2540 (1978).

55. Cai, W., Reber, T. J. & Piestun, R. Computer-generated volume holograms fabricated by femtosecond laser micromachining. *Opt. Lett.* **31,** 1836–1838 (2006).

56. Gerke, T. D. & Piestun, R. Aperiodic volume optics. *Nature Photonics,* 188–193 (2010).

57. Kamau, E. N., Sreenivas, V. V. P., Bülters, M., Falldorf, C. & Bergmann, R. B. *Fabrication of Multiplexed Computer Generated Volume Holograms in Photosensitive Glass,* in *Frontiers in Optics* (2014), FTh4G–1.

58. Wolf, E. Three-dimensional structure determination of semi-transparent objects from holographic data. *Opt. Commun.* 153–156 (1969).

59. Dallas, W. Computer-Generated Holograms. *The Computer in optical research: methods and applications* **41,** 291 (1980).

60. Cech, J. *Forming of diffractive microoptical elements in amorphous chalcogenide thin films* PhD thesis (2002).

61. Lukin, A. Holographic optical elements. *J. Opt. Tech.* **74,** 65–70 (2007).

62. Murti, Y. & Vijayan, C. *Essentials of Nonlinear Optics* (John Wiley & Sons, 2014).

63. Saleh, B. E. A. & Teich, M. C. *Fundamentals of Photonics (Wiley Series in Pure and Applied Optics)* 1st Ed. (John Wiley & Sons, 1991).

64. Jahns, J. & Helfert, S. *Introduction to micro-and nanooptics* (John Wiley & Sons, 2012).

65. Lipson, A., Lipson, S. G. & Lipson, H. *Optical physics* (Cambridge University Press, 2010).

66. Marom, E., Friesem, A. A. & Wiener-Avner, E. *Applications of holography and optical Data Processing* (Pergamon, 1977).

67. Ewald, P. Introduction to the dynamical theory of X-ray diffraction. *Acta Crystallographica Section A: Crystal Physics, Diffraction, Theoretical and General Crystallography* **25,** 103–108 (1969).

68. Williams, E. G. *Fourier acoustics: sound radiation and nearfield acoustical holography* (academic press, 1999).

69. Wyrowski, F. & Bryngdahl, O. Digital holography as part of diffractive optics. *Prog. Phys.* **54,** 1481 (1991).

70. Sherman, G. C. Integral-transform formulation of diffraction theory. *J. Opt. Soc. Am.* **57,** 1490–1498 (1967).

71. Ersoy, O. K. *Diffraction, fourier optics and imaging* (John Wiley & Sons, 2006).

72. Coupland, J. M. & Lobera, J. Holography, tomography and 3D microscopy as linear filtering operations. *Measurement science and technology* **19,** 074012 (2008).

73. Whyte, G. & Courtial, J. Experimental demonstration of holographic three-dimensional light shaping using a Gerchberg–Saxton algorithm. *New Journal of Physics* **7,** 117 (2005).

74. Born, M. & Wolf, E. *Principles of optics: electromagnetic theory of propagation, interference and diffraction of light* (Cambridge University Press, 1999).

75. Kreis, T. *Handbook of Holographic Interferometry: Optical and Digital Methods* (Wiley-VCH, 2005).

76. Yamaguchi, I. & Zhang, T. Phase-shifting digital holography. *Opt. Lett.* **22,** 1268–1270 (1997).

77. Leith, E. N. & Upatnieks, J. Wavefront Reconstruction with Continuous-Tone Objects. *J. Opt. Soc. Am.* **53,** 1377–1381 (1963).

78. Xu, L., Peng, X., Guo, Z., Miao, J. & Asundi, A. Imaging analysis of digital holography. *Opt. Express* **13,** 2444–2452 (2005).

79. Fienup, J. R. Phase retrieval algorithms: a comparison. *Appl. Opt.* **21,** 2758–2769 (1982).

80. Wyrowski, F. & Bryngdahl, O. Iterative Fourier-transform algorithm applied to computer holography. *J. Opt. Soc. Am.* **5,** 1058–1065 (1988).

81. Gerke, T. D. *Aperiodic Volume Optics* PhD thesis (University of Colorado at Boulder , USA, 2010).

82. Bastiaans, M. J. The Wigner distribution function applied to optical signals and systems. *Opt. Commun.* **25,** 26–30 (1978).

83. Hillery, M., O'connell, R., Scully, M. & Wigner, E. P. *Distribution functions in physics: fundamentals* (Springer, 1997).

84. Kak, A. C. & Slaney, M. *Principles of computerized tomographic imaging* (Society for Industrial and Applied Mathematics, 2001).

85. Slaney, M., Kak, A. C. & Larsen, L. E. Limitations of imaging with first-order diffraction tomography. *Microwave Theory and Techniques, IEEE Transactions on,* 860–874 (1984).

86. Griffiths, D. J. & Harris, E. G. *Introduction to quantum mechanics* (Prentice Hall New Jersey, 1995).

87. Aoki, K., Okamoto, A., Wakayama, Y., Tomita, A. & Honma, S. Selective multimode excitation using volume holographic mode multiplexer. *Opt. Lett.* **38,** 769–771 (2013).

88. Coufal, H. J., Sincerbox, G. T. & Psaltis, D. *Holographic data storage* (Springer-Verlag New York, Inc., 2000).

89. Klein, W. & Cook, B. D. Unified approach to ultrasonic light diffraction. *Sonics and Ultrasonics, IEEE Transactions on* **14,** 123–134 (1967).

90. Barden, S. C., Arns, J. A. & Colburn, W. S. *Volume-phase holographic gratings and their potential for astronomical applications* in *Astronomical Telescopes & Instrumentation* (1998), 866–876.

91. Heifetz, A., Shen, J. T. & Shahriar, M. A simple method for Bragg diffraction in volume holographic gratings. *American Journal of Physics* **77,** 623–628 (2009).

92. Bertero, M. & Boccacci, P. *Introduction to inverse problems in imaging* (CRC press, 1998).

93. Devaney, A. Inversion formula for inverse scattering within the Born approximation. *Opt. Lett.* **7,** 111–112 (1982).

94. Stuart, B., Feit, M., Herman, S, Rubenchik, A., Shore, B. & Perry, M. Nanosecond-to-femtosecond laser-induced breakdown in dielectrics. *Physical Review B* **53,** 1749 (1996).

95. Misawa, H. & Juodkazis, S. *3D laser microfabrication: principles and applications* (John Wiley & Sons, 2006).

96. Hongo, T., Sugioka, K., Niino, H., Cheng, Y., Masuda, M., Miyamoto, I., Takai, H. & Midorikawa, K. Investigation of photoreaction mechanism of photosensitive glass by femtosecond laser. *J. Appl. Phys.* **97,** 063517 (2005).

97. Ishimaru, A. *Wave propagation and scattering in random media* (Academic press New York, 1978).

98. Brown Jr, W. Validity of the Rytov approximation in optical propagation calculations. *J. Opt. Soc. Am.* **56,** 1045–1052 (1966).

99. Kak, A. C. & Slaney, M. *Principles of computerized tomographic imaging* (Siam, 1988).

100. Marks, D. L. A family of approximations spanning the Born and Rytov scattering series. *Opt. Express* **14,** 8837–8848 (2006).

101. Tatarski, V. I., Silverman, R. A. & Chako, N. Wave propagation in a turbulent medium. *Physics Today* **14,** 46–51 (2009).

102. Gubin, L., Polyak, B. & Raik, E. The method of projections for finding the common point of convex sets. *USSR Computational Mathematics and Mathematical Physics* **7,** 1–24 (1967).

103. Youla, D. C. & Webb, H. Image Restoration by the Method of Convex Projections: Part 1Theory. *Medical Imaging, IEEE Transactions on* **1,** 81–94 (1982).

104. Feit, M., Fleck Jr, J., *et al.* Light propagation in graded-index optical fibers. *Appl. Opt.* **17,** 3990–3998 (1978).

105. Belvaux, Y. Influence of emulsion thickness in hologram reconstruction. *Phys. Lett. A* **25,** 70–71 (1967).

106. Falldorf, C., Osten, S., Kopylow, C. v. & Jüptner, W. Shearing interferometer based on the birefringent properties of a spatial light modulator. *Opt. Lett.* **34,** 2727–2729 (2009).

107. Cohn, R. W. *Real-time multispot beam steering with electrically controlled spatial light modulators* in *Optical Science, Engineering and Instrumentation'97* (1997), 145–155.

108. Cai, W., Libertun, A. R. & Piestun, R. Polarization selective computer-generated holograms realized in glass by femtosecond laser induced nanogratings. *Opt. Express* **14,** 3785–3791 (2006).

109. Cheng, Y., Sugioka, K. & Masuda, M. Optical gratings embedded in photosensitive glass by photochemical reaction using a femtosecond laser. *Opt. Express* **11,** 1809–1816 (2003).

110. Sreenivas, V. P., Bülters, M & Bergmann, R. Microsized subsurface modification of mono-crystalline silicon via non-linear absorption. *Journal of the European Optical Society-Rapid publications* **7** (2012).

111. Tan-No, N., Ohkawara, K. & Inaba, H. Coherent Transient Multiphoton Scattering in a Resonant Two-Level System. *Physical Review Letters* **46,** 1282 (1981).

112. Beeson, K., Horn, K., McFarland, M & Yardley, J. Photochemical laser writing of polymeric optical waveguides. *Appl. Phys. Lett.* **58,** 1955–1957 (1991).

113. Marcinkevičius, A., Juodkazis, S., Watanabe, M., Miwa, M., Matsuo, S., Misawa, H. & Nishii, J. Femtosecond laser-assisted three-dimensional microfabrication in silica. *Opt. Lett.* **26,** 277–279 (2001).

114. Barbastathis, G. & Brady, D. J. Multidimensional tomographic imaging using volume holography. *Proceedings of the IEEE* **87,** 2098–2120 (1999).

115. Yura, H. T., Sung, C., Clifford, S. F. & Hill, R. J. Second-order Rytov approximation. *J. Opt. Soc. Am.* **73,** 500–502 (1983).

116. Cairns, B. & Wolf, E. Comparison of the Born and the Rytov approximations for scattering on quasi-homogeneous media. *Opt. Commun.* **74,** 284–289 (1990).

117. Okamoto, K. *Fundamentals of optical waveguides* (Academic press, 2010).

118. Xu, C. & Huang, W. Finite-difference beam propagation method for guide-wave optics. *Progress In Electromagnetics Research, PIER* **11,** 1–49 (1995).

119. Poon, T.-C. & Kim, T. *Engineering optics with MATLAB* (World Scientific, 2006).

120. Agrawal, G. P. *Nonlinear fiber optics* (Academic press, 2007).

121. Wartak, M. S. *Computational photonics: an introduction with MATLAB* (Cambridge University Press, 2013).

122. Moharam, M. & Gaylord, T. Rigorous coupled-wave analysis of planar-grating diffraction. *J. Opt. Soc. Am.* **71,** 811–818 (1981).

123. Van der Aa, N. P. in *Progress in Industrial Mathematics at ECMI 2004* 99–103 (Springer, 2006).